The Dissertation Committee for Xiaoguang Sun Certifies that this is the approved version of the following dissertation:

High Performance 1300 nm Photodetectors Grown By Molecular Beam Epitaxy

Committee:

Archie L. Holmes, Jr., Supervisor

Joe C. Campbell

Russell D. Dupuis

Dean P. Neikirk

John G. Ekerdt

High Performance 1300 nm Photodetectors Grown by Molecular Beam Epitaxy

by

Xiaoguang Sun, B. S., M. S., M. S. E. E

Dissertation

Presented to the Faculty of the Graduate School of

The University of Texas at Austin

in Partial Fulfillment

of the Requirements

for the Degree of

Doctor of Philosophy

The University of Texas at Austin

December 2002

Dedicated

to

my wife

Yuming Gu

and

our parents

Acknowledgements

I am deeply grateful to my supervising professor, Dr. Archie L. Holmes, Jr., for giving me the opportunity to pursue my Ph.D. degree under his supervision. I knew nothing about the molecular beam epitaxy when I first jointed his research group in 1998. Without his constant guidance, encouragement and support during my four and half year study, I would still be a layman of the optoelectronic research area. I am also in debt to Professor Joe C. Campbell. His support and valuable advices make my efforts possible. I have learned a lot from Professor Ben G. Streetman during my first year in MBE group. I would like to thank Dr. Russell D. Dupuis, Dr. Dean P. Neikirk and Dr. John G. Ekerdt for serving on my dissertation committee.

I would like to express my deep appreciation to Terry J. Mattord. His excellent technical knowledge and skills are the guarantee for the running of our MBE laboratory. He is always ready to help me whenever I meet difficulties. I am also grateful to Jean Toll, Amy Pinkston, Joyce Kokes and Steve Moore for helping me with administrative and purchasing issues.

I would like to thank my fellow group members including Rubin Sidhu, Jeffery B. Hurst, Sridhar Govindaraju, Michael M. Oye, Chet Lenox, Chad Hansing, Jason Reifsnider, Oleg Baklenov and David Gotthold. All of them have given me a lot of help and provided me very useful suggestions in my research.

Without the cooperation among the group members, the maintenance and operation of the MBE systems are impossible.

I want to thank Xiaoguang Zheng, Shuling Wang, Xiaowei Li, Feng Ma, Ning Li, Ping Yuan and Jean Hsu in Professor Joe C. Campbell's group. I have learned a lot from them in photodetector theory and design, device fabrication and testing. We have cooperated in several projects and these collaborations have benefited me a lot. I also want to thank my friends and colleagues in the Microelectronics Research Center such as Hao Chen, Oleg Shchekin, Manhong Zhang, Qingwei Mo, Chuanshun Cao, Hua Huang, Zhengmao Ye, Bo Yang, Dingyuan Lu, Xiao Chen, Michael M. Wong and etc.

Finally I wish to express my deep gratitude to my wife Yuming Gu for her love and encouragement during the years and my parents, parents-in-law, sister and brother-in-law for their selfless support in my life.

Xiaoguang Sun

The University of Texas at Austin

December 2002

High Performance 1300 nm Photodetectors Grown by Molecular Beam Epitaxy

Publication No._____

Xiaoguang Sun, Ph.D.

The University of Texas at Austin, 2002

Supervisor: Archie L. Holmes, Jr.

Photodetectors operating at 1.3 μm on GaAs substrates with low noise, low dark current, high quantum efficiency and high bandwidth are very attractive for applications in long haul, fiber optic communication systems. GaAsSb is a promising material for 1.3 μm emission and absorption on GaAs substrates. However, GaAsSb is not lattice-matched on GaAs substrate and As and Sb have different sticking coefficients with Ga, which makes both the growth and device realization difficult. This dissertation discusses the molecular beam epitaxy (MBE) growth of compressively strained GaAsSb layers on GaAs substrates. We found that the optical properties and alloy composition of GaAsSb highly depend on the growth parameters, such as growth temperature, Ga growth rate, Sb and As fluxes. We also reported two resonant-cavity-enhanced (RCE) avalanche photodiode (APD) structures with GaAsSb/GaAs multiple quantum well

absorption regions. The RCE GaAsSb *p-i-n* photodiode exhibited a peak external quantum efficiency of 54% at the wavelength of 1.3 μm with a full-width-at-half-maximum of 8 nm. In the RCE GaAsSb APD with separate absorption, charge and multiplication regions (SACM), the high electric field multiplication region was separated from the intrinsic absorption region. As a result, the RCE GaAsSb SACM APD exhibited very low dark current (~5 nA) at 90% of the breakdown. By utilizing thin undoped $Al_{0.9}Ga_{0.1}As$ layer as the multiplication region, very low multiplication noise with k value ~ 0.1 was obtained in the SACM APD. This is the lowest noise reported to date for APDs operating at 1.3 μm.

Table of Contents

List of Tables

List of Figures

Chapter 1: Introduction

The 21st century is an era for optical communication. The idea of using light as a transmission media for modern communication was first proposed by Alexander Graham Bell back in the late 1870s. But it only remained as a dream until the invention of lasers in 1960s [1.1] and the development of low-loss optical fibers in 1970s [1.2, 1.3]. Since then, fiber optic communication systems have been developed rapidly and become the dominant backbone of the information-carrying infrastructures across the world due to the low transmission loss, high bandwidth, low cost and high security. In 1988, the first transatlantic fiber-optic cable was laid, and the "information superhighway" was on its way to becoming reality.

The fiber-optic communication system includes a transmitter, an optical fiber channel for light transmission and a receiver. Photodetector is the essential part of the receiver because it converts the optical signals into electrical signals at the receiving end. Optical fibers can transmit light over a wide range of wavelengths. For long-haul, high-bit-rate fiber optic communication applications, the operation at 1.3 μm or 1.55 μm is a very useful attribute for both lasers (essential parts of transmitters) and photodetectors because silica-based optical fibers have minimum dispersion and attenuation at these wavelengths [1.4, 1.5].

The operating wavelength of photodetector is determined by the bandgap of the absorption material. Traditionally, InP-based materials such as InGaAs (P) have been employed for photodetectors operating at 1.3 μm or 1.55 μm because

InGaAs (P) can be grown lattice-matched on InP substrates and its composition can be adjusted to produce photodetectors in the required wavelength range [1.6, 1.7, 1.8]. However, there are drawbacks for InP-based devices as compared to those fabricated from GaAs-based materials. For example, it is difficult to make InP-based distributed Bragg reflectors (DBRs) with high reflectance due to the lack of InP-based materials with big refractive index difference. In contrast, GaAs and AlAs have a refractive index difference of more than 14% so that GaAs/AlAs DBRs with near unity reflectivity can be achieved. The superior DBR mirror is very important for vertical-cavity surface-emitting lasers (VCSELs) [1.9] and resonant-cavity-enhanced (RCE) photodetectors [1.10]. The GaAs wafers are much cheaper than InP wafers which can reduce the manufacturing cost. In addition, GaAs-based material systems have better thermal conductivity than InP-based materials which helps to enhance the heat dissipation [1.11]. More important, GaAs-based optoelectronic devices that operate at 1.3 μm or 1.55 μm will benefit from their compatibility with the more mature GaAs-based electronic technologies. However, since there are no naturally available material systems lattice-matched on GaAs substrates with suitable bandgaps for this wavelength range, significant efforts have been devoted to achieve 1.3 μm operation on GaAs substrates by using strained material systems or wafer bonding techniques. GaAs-based 1.5 μm laser with highly strained quantum wells (QWs) has also been reported [1.12]. But it is not the main trend due to the difficulties in material growth and poor device performances.

The candidates for 1.3 μm emission and absorption on GaAs substrates include InGaNAs alloys [1.13, 1.14, 1.15], (Ga) InAs quantum dots (QDs) [1.16, 1.17, 1.18], wafer fusion between InGaAsP-based active regions and GaAs-based DBR mirrors and other parts [1.19, 1.20, 1.21] and GaAsSb [1.22-1.25]. InGaAsN lasers [1.26, 1.27] and photodetectors [1.28] operating at 1.3 μm have been reported. However, it is very difficult to incorporate significant amount of N atoms into GaInAs and the material properties also degrade when adding more N atoms into the lattice [1.29]. Tan *et al* [1.30, 1.31] used wafer fusion technique to bond a *p-i-n* photodiode grown on InP substrate with a GaAs/AlAs DBR mirror grown on GaAs. By depositing a Si/SiO_2 top mirror after etching the InP substrate, quantum efficiency higher than 90% was obtained at 1.3 μm. However, the fabrication requires two growth steps and the wafer fusing and etching processes are relatively complex. Therefore, questions remain as to whether it is a practical technology for manufacture. More recently, 1.31 μm edge-emitting QD lasers have been demonstrated [1.32]. Room temperature operation of QD-based VCSELs has also been achieved [1.33] but the lasing wavelength was only 1.15 μm. InGaAs quantum dot resonant-cavity photodiode operating at wavelength close to 1.3 μm has also been reported [1.34]. However, like wafer fusion, this technology has not yet demonstrated capacity for high-volume manufacturing. Compared to its competitors, the easy incorporation of an arbitrary amount of Sb into GaAs makes GaAsSb a promising material system for this application. Room temperature operation of GaAsSb VCSELs at 1.29 μm has

been reported [1.35]. GaAsSb photodiode operating at 1.3 μm has also been demonstrated [1.36].

For high bandwidth, long-haul fiber optic communication systems, the avalanche photodiode (APD) is usually the detector of choice owing to its internal gain. In order to reduce the number of repeaters and amplifiers, the photodetectors need to have very high sensitivity. The ultimate detection capability of a detector is limited by the noise and dark current. The multiplication region of an APD plays an important role in the determination of gain, multiplication noise and gain-bandwidth-product. The multiplication noise is lower and bandwidth is higher if most of the impact ionization processes are caused by a single type of carrier with higher impact ionization coefficient. As a result, a great deal of researches have been devoted to develop novel, low noise APD structures with $\beta/\alpha \approx 0$ (pure electron ionization) or $\alpha/\beta \approx 0$ (pure hole ionization) where α and β are the electron and hole ionization coefficient, respectively. Low noise and high gain-bandwidth product have been reported on APDs with very thin multiplication regions [1.37-1.40]. History-depend avalanche theory [1.41, 1.42] has to be used to explain the ionization processes in very thin multiplication regions instead of R. J. McIntyre's conventional local-field theory [1.43].

This dissertation reports the researches done in the University of Texas at Austin on GaAs-based GaAsSb/GaAs avalanche photodiodes operating at 1.3 μm with low multiplication noise. We have studied the molecular beam epitaxy (MBE) growth of GaAsSb on GaAs substrates. The optical properties and composition of GaAsSb layer strongly depend on the growth temperature, the Ga

growth rate as well as the As and Sb fluxes. We have also studied the noise of high-Al-ratio $Al_xGa_{1-x}As$ multiplication regions and Impact-Ionization-Engineered multiplication Regions. Very low multiplication noise has been achieved from these approaches. By using GaAsSb as the absorption region and $Al_xGa_{1-x}As$ with high Al concentration as the multiplication region, GaAs-based avalanche photodiode operating at 1.3 μm with low noise has been demonstrated.

Chapter 2 introduces the system setup and growth physics of molecular beam epitaxy. The fundamentals of material characterization techniques used in this study such photoluminescence and X-ray diffraction have also been discussed.

Chapter 3 is focused on the issues related to the MBE growth of GaAsSb on GaAs substrates. The influences of various growth conditions such as growth temperature, group-III and group-V fluxes to the optical properties and composition of GaAsSb layers are discussed. Sb segregation effect at GaAsSb/GaAs interface and the characteristics of Sb valved cracker source are also discussed. Strong photoluminescence at 1.3 μm has been achieved from GaAs/GaAsSb single or multiple quantum well structures.

Chapter 4 reviews the key performance parameters of photodetectors used in long-haul, high speed, fiber optic communication systems. The structures and operation mechanisms of PIN photodiodes and avalanche photodiodes are described. Details about the design of distributed Bragg reflector mirrors and resonant-cavity-enhanced APD structures are discussed. This chapter also talks

about the design and performance of avalanche photodiodes with separate absorption, charge and multiplication regions.

Chapter 5 demonstrates a resonant-cavity-enhance *p-i-n* photodiode with multiple GaAsSb absorption layers operating at 1.3 μm on GaAs substrates. Issues related to the APD structure design, material growth, device fabrication processes as well as optical and electrical testing are discussed. This APD has an operation wavelength of 1.3 μm and good external quantum efficiency but relatively high dark current at high bias.

Chapter 6 describes a resonant-cavity-enhanced GaAsSb avalanche photodiode with separate absorption, charge and multiplication regions. By the separation of multiplication region with high electric field and intrinsic absorption region, the dark current of the device was significantly reduced at high bias. This chapter also talks about the design of low noise multiplication regions. High Al-ratio $Al_xGa_{1-x}As$ ($x \geq 0.8$) and impact ionization engineered structures (I^2E) exhibit very low multiplication noise. By using thin $Al_{0.9}Ga_{0.1}As$ as the multiplication region in the RCE SACM structure, very low excess noise with k value ~0.1 was obtained.

Finally, Chapter 7 concludes this dissertation and proposes a few directions for future research.

Chapter 2: Materials Growth and Characterization Techniques

2.1 MOLECULAR BEAM EPITAXY

Molecular beam epitaxy (MBE) is a highly precise and versatile crystal growth technique developed in early 1970's in AT&T Bell Labs [2.1, 2.2]. Today it becomes one of the most important growth techniques for III-V and II-VI compound semiconductors, metals and insulators. In MBE, ultra-pure elements such as Ga, Al and As are delivered to a heated substrate surface in ultra-high vacuum in the form of thermally evaporated molecular or atomic beams. The atoms or molecules in the beams deposit on the heated substrate to form the growing solid layers. Typically, each element is delivered in a separately controlled beam. The composition of the grown epilayer and its doping level depend on the relative arrival rates of the constituent elements and dopants, which in turn depend on the evaporation rates of the source materials. Each beam can be turned on and off rapidly with a shutter or a valve and this produces abrupt interfaces on atomic scale and good control of thickness, doping and concentration. The beam flux can be adjusted by changing the evaporation temperature of the source material. The growth rate is typically 1 μm/hour (~1 monolayer/second), which is sufficient low that ensures the surface migration of the impinging species on the growing surface.

In the Microelectronics Research Center at the University of Texas at Austin, a customized Varian Gen II solid source MBE system was designed and built for the growth of $Al_xGa_{1-x}As$, $GaAs_{1-x}Sb_x$ and phosphide-based materials

such as InP and $GaAs_{1-x}P_x$. The system consists of three main chambers: the load lock for transferring samples into and out of the vacuum environment, the buffer chamber for outgasing and storage of samples, and the growth chamber.

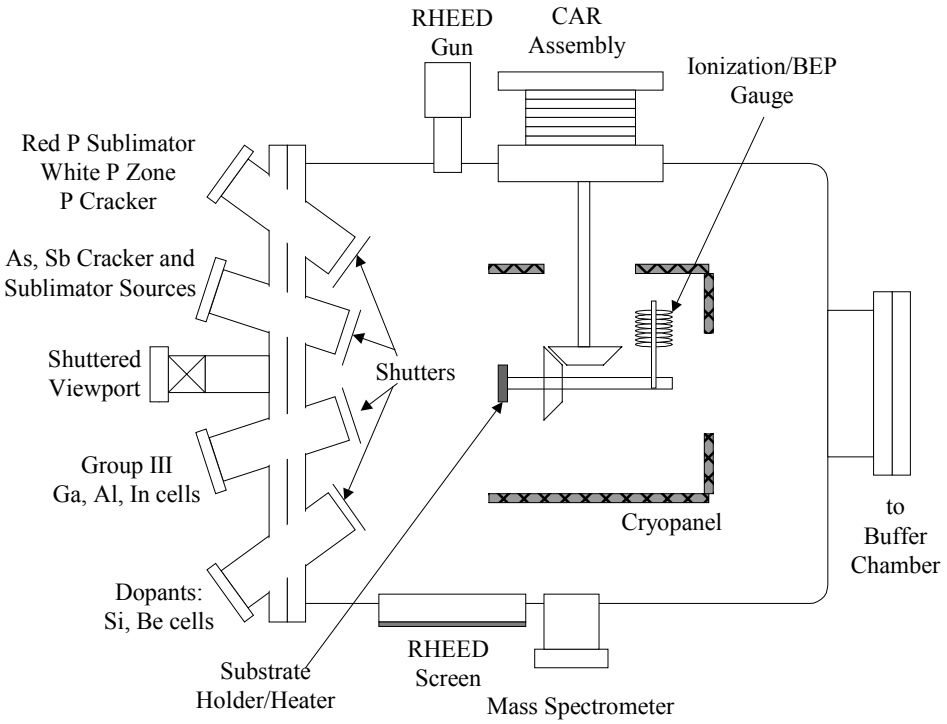

Figure 2.1 Schematic diagram of MBE growth chamber at University of Texas at Austin.

The sample is held on the CAR (Continual Azimuthal Rotation) assembly that can rotate and heat the sample during growth. The ion gauge measures the growth chamber pressure and beam equivalent pressure (BEP) of the sources. A liquid-nitrogen-cooled cryopanel surrounding the CAR is used as an effective pump for many of the residual gases in the chamber such as H_2O, CO_2 and CO.

Two CTI Cryo-Torr 8 cryopumps (not shown in this diagram) maintain the growth chamber at a base pressure of low 10^{-10} Torr. Reflection high-energy electron diffraction (RHEED) is used for calibrating the growth rates, observing removal of the oxides from the surface, monitoring the arrangement of surface atoms, etc. An UTI quadrupole mass spectrometer (QMS) is mounted near the RHEED screen to check for leaks, detect residual gases and analyze source beams.

The source flange on the growth chamber contains a viewport and eight effusion cells. The eight effusion cells include three group-III cells such as Ga, In and Al, three group-V cells such as As, Sb and P, and two dopant cells such as Si and Be. Si and Be are for n-type and p-type doping, respectively. For group-III and dopant cells, ultrahigh-purity elemental source materials are loaded in pyrolytic boron nitride (PBN) crucibles and heated by tantalum heating wires. In order to control the effusion cell temperature to an accuracy of ±0.5°C to provide the precise amount of beam flux, highly stable control loops with Tungsten-Rhenium thermocouples and proportion, integral and derivative (PID) controllers are used. Each effusion cell is surrounded by a coolant-chilled shroud to eliminate the cross talk between neighboring cells. Computer-controlled PBN shutters are positioned in front of each cell to be able to shutter the flux. Because the growth of III-V compound semiconductors requires group-V overpressure and thus consumes more group-V materials than group-III materials, the group-V sources are more massive and it takes several hours for group-V cell temperature to stabilize. For this reason, the group-V As, Sb and P sources are valved crackers.

The fluxes of As, P and Sb can be easily controlled by adjusting the positions of needle valves. The As and Sb cells on this MBE chamber are Applied Epi two-zone valved cracker sources with low-temperature sublimators and high-temperature cracking tubes. Bigger group-V molecules such as As_4 and Sb_2 are generated in the sublimators and dissociated into smaller molecules such as As_2 and Sb_1 when traveling through the high temperature cracking tubes. The use of smaller group-V molecules can significantly improve the incorporation efficiencies of group-V species into the epitaxial layers because the incorporation mechanism is simpler for smaller group-V speices [2.3]. The Sb cell is entirely constructed of PBN in order to protect the source from corrosion due to Sb exposure. Since As and Sb fluxes are frequently changed during the growth of multiple $GaAs_{1-x}Sb_x$/GaAs quantum wells, an Applied Epi automatic valve positioner is used for both As and Sb valves.

One of the advantages of MBE is that it is a ultra high vacuum (UHV) technique and therefore surface analysis techniques may be used to monitor the growth process before, during and after deposition. RHEED is the most useful and important surface analysis instrument in the MBE growth chamber. It can be used to calibrate the growth rates; observe the removal of oxides from the surface; obtain information concerning substrate cleanliness, smoothness, and arrangement of surface atoms; and etc. A collimated electron beam with high energy around 10KeV is emitted by RHEED gun and directed at a shallow angle of 1-2° to the sample surface. The reflected electrons strike on the fluorescent screen opposite to the RHEED gun and form the diffraction pattern. The RHEED pattern varies with

growth temperature as well as the group-III and group-V fluxes. Therefore, the appearance of the RHEED pattern can be used as a reference to determine the substrate temperature and relative group-III/group-V overpressure. At typical growth conditions, the As-stabilized GaAs (100) surface has (2 × 4) reconstruction. Experimental data show that atoms at and near the surface do not exhibit the same arrangement as in the bulk. A surface structure denoted by ($m \times n$) means that it has a surface structure whose unit mesh is $m \times n$ times larger than the underlying bulk structure.

Figure 2.2 shows the schematic drawing of (100) GaAs (2 × 4) RHEED pattern. The "2 ×" is along [011] direction and "4 ×" is along [01$\bar{1}$] direction. The primary lines reflect the spacing between atoms in the bulk. The ½ and ¼ order lines correspond to the spacing between atoms on the surface along [011] and [01$\bar{1}$] directions, respectively. For Ga-stabililzed GaAs (001) surface, the RHEED pattern is (4 × 2) [2.4]. For GaAs growth, the As-stabilized structure is desired because high quality, smooth (100) GaAs layer can be achieved under this condition.

The intensity change of RHEED pattern during the film deposition can be used to calibrate the growth rate. Figure 2.3 shows the RHEED intensity oscillation when depositing GaAs on a smooth GaAs substrate. At the beginning of the growth (Point 1), the surface is smooth and therefore the RHEED pattern is bright. After some Ga and As atoms are deposited on the surface and form islands (Point 2 and 3), the surface becomes rough and the RHEED pattern dims. After the growth of one layer GaAs, the surface becomes smooth again and the RHEED

intensity recovers (Point 4). Therefore, the growth rate can be calculated from the RHEED oscillation frequency.

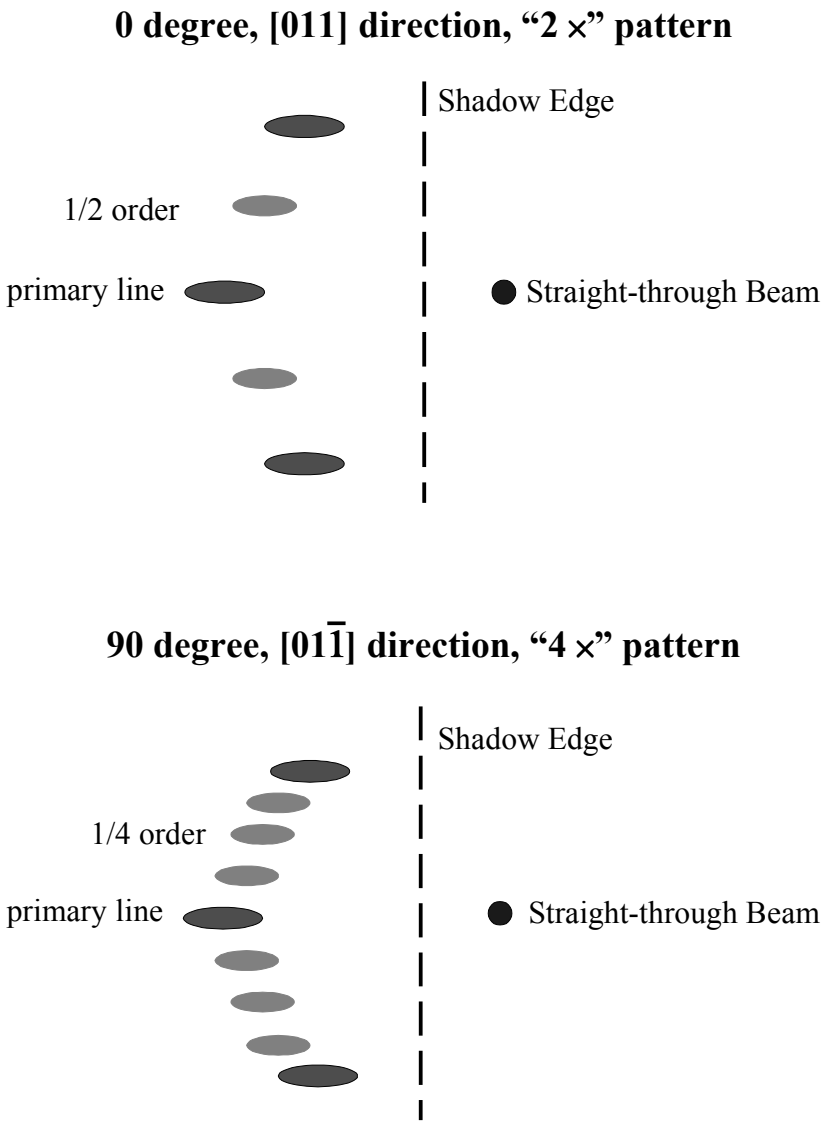

Figure 2.2: Schematic drawing of (001) GaAs (2 × 4) RHEED pattern

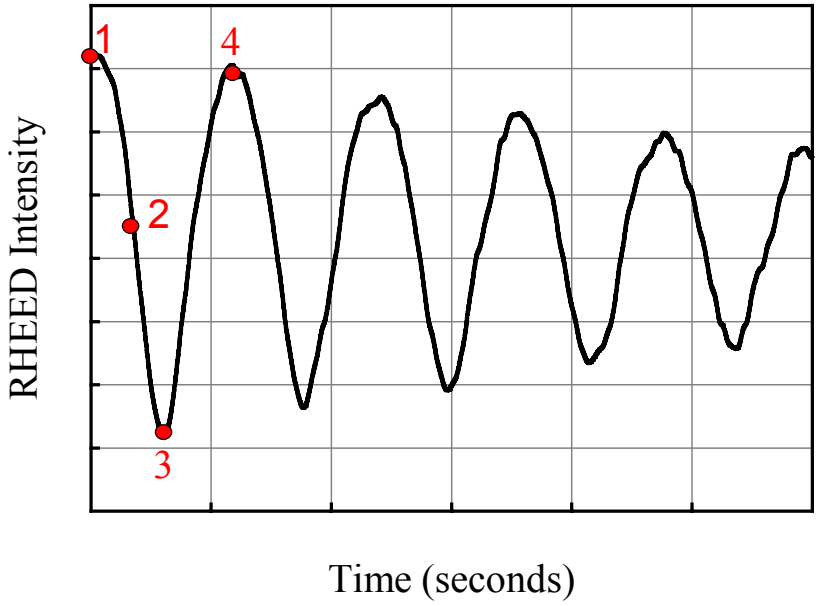

Figure 2.3: RHEED oscillation during the growth of GaAs on GaAs substrate.

In MBE, the growth rate is typically below 1 monolayer/second in order to ensure the surface migration of the impinging species on the growing surface. One monolayer (ML) III-V compound semiconductor contains one layer of group-III atoms and one layer of group-V atoms, which is equal to the thickness of half of the lattice. For example, the lattice constant of GaAs is 5.65Å. Therefore, one monolayer of GaAs is 2.83Å.

At typical growth temperatures, the surface sticking coefficients of group-III atoms are near unity but the sticking coefficients of group-V atoms are smaller than unity. Therefore, group-V overpressure is required and the growth rate is mainly determined by the deposition rate of group-III atoms. For ternary compounds such as $Al_xGa_{1-x}As$ on GaAs substrate, the total growth rate is the

growth rate of Ga plus the growth rate of Al. The composition of the ternary compound is determined by the relative growth rates of Ga and Al. Since GaAs and AlAs are lattice-matched on GaAs substrate, the growth rates of Ga and Al can be calibrated on GaAs substrate directly. $In_{0.53}Ga_{0.47}As$ and $In_{0.52}Al_{0.48}As$ are lattice-matched on InP substrate. However, we can't calibrate In, Ga or Al growth rate directly on InP substrate because InAs, GaAs and AlAs are not lattice-matched on InP. The easiest solution is to calibrate the Ga and Al growth rates on GaAs substrate first. Due to the unequal lattice constant, the growth rate for a give material flux on GaAs substrate can be converted into the equivalent growth rate on InP substrate. The conversion relation is:

$$R_{InP} = R_{GaAs} * \left(\frac{a_{InP}}{a_{GaAs}} \right)^2 = 1.079 * R_{GaAs} \qquad (2.1)$$

In Equation (2.1), R_{InP} is the Al or Ga growth rate on InP substrate, R_{GaAs} is the growth rate on GaAs substrate, a_{InP} is the lattice constant of InP (a_{InP} = 5.87Å), a_{GaAs} is the lattice constant of GaAs (a_{GaAs} = 5.65Å). For example, for $In_{0.53}Ga_{0.47}As$ on InP substrate, if we want the growth rate of $In_{0.53}Ga_{0.47}As$ around 1 ML/s, we need In growth rate of 0.53 ML/s on InP and Ga growth rate of 0.47 ML/s on InP. From Equation (2.1), the required Ga growth rate on GaAs substrate is 0.436 ML/s. The In growth rate can be calibrated by growing InP on InP substrate. But not all the MBE systems are equipped with P sources. We know that an In flux of 3.0×10^{-7} torr is roughly equal to an In growth rate of 0.53 ML/s. From this start point, we can fine-tune the In growth rate to the exact value by calibrating the InGaAs growth rate on InP substrate.

More details about the MBE technology and its development can be found in literatures [2.5-2.10].

2.2 PHOTOLUMINESCENCE

Photoluminescence (PL) is a very useful tool to study the optical properties of compound semiconductors. In photoluminescence process, light from the optical pumping laser is directed onto the sample where it is absorbed and the excess energy is transferred into the material in a process called "photo-excitation". Since the optical pumping laser has energy greater than the material bandgap energy, the photo-excitation causes the electrons in the valence band to jump into the permissible excited states in the conduction band and thus generates electron-hole pairs. When the excited electrons return to their equilibrium states and recombine with holes in valence band, the excess energy is released and may include the emission of light (radiative process) or may not (nonradiative process). The energy of the emitted light, in other words, the emission wavelength of the light, is related to the energy difference between the two electron states involved in the transition. This can be used for the bandgap determination, which is particularly useful in the study of new compound semiconductors. The intensity of the emitted light is related to the relative contributions of the radiative processes. In general, nonradiative process is associated with localized defects. Therefore, the relative intensity of the PL spectra can be used to determine the material quality.

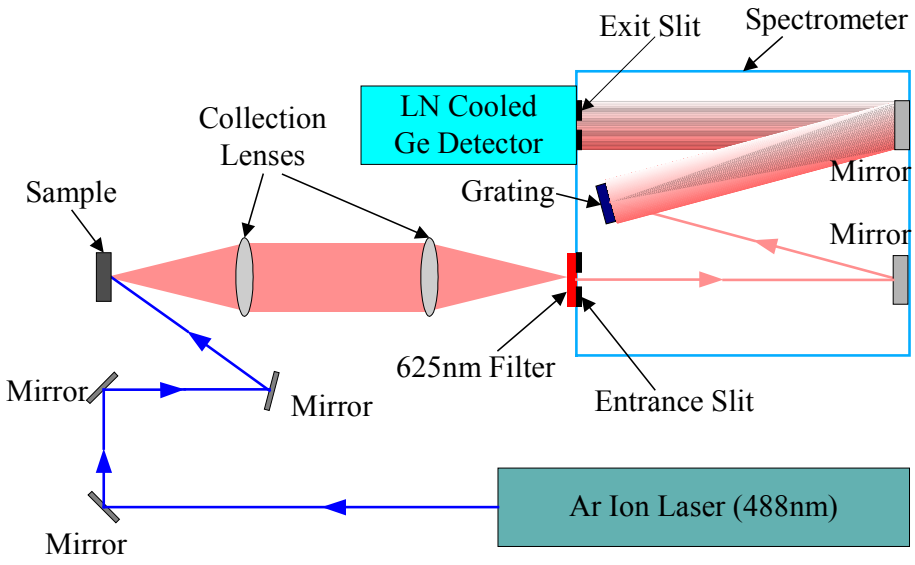

Figure 2.4: Schematic drawing of photoluminescence system.

Figure 2.4 shows the schematic drawing of the photoluminescence system. This setup is for room temperature (300K) PL measurement. Because the emission wavelength that we are interested in is in the range of 0.8-1.5 μm, a 488nm (2.5 eV) Coherent Innova-90 argon ion laser is used as the optical pumping laser. The laser beam is aligned and focused on the sample surface by adjusting the positions and angles of different mirrors. The sample emits light with different wavelengths through photo-excitation and recombination processes. The emitted light is collected by a pair of collection lenses and directed into the spectrometer through a 625 nm cutoff filter and entrance slit. The 625 nm cutoff filter blocks the optical signals with wavelengths shorter than 625 nm and thus reduces the interference with signals from the sample. The photoluminescence

signals with various wavelengths are spread out by a 600 g/mm grating and then enter the liquid-nitrogen-cooled Ge detector through the exit slit.

For low temperature measurement, the sample should be dipped into liquid nitrogen (77K) or liquid helium (4.2K) but the rest of the setup is essentially the same.

2.3 X-RAY DIFFRACTION

X-ray diffraction (XRD) is a versatile, non-destructive analytical technique for crystalline materials. In my dissertation work, XRD was used to study the composition and material quality of $GaAs_{1-x}Sb_x$ epitaxial layers.

Diffraction occurs as waves interact with a regular structure whose repeat distance is about the same as the wavelength. Because X-rays have wavelengths on the order of a few angstroms, the same as typical interatomic distances in crystalline solids, X-rays can be diffracted from crystals with regularly repeating atomic structures. When certain geometric requirements are met, X-rays scattered from a crystalline solid can constructively interfere, producing a diffracted beam. The diffraction condition can be expressed by Bragg's law:

$$2d\sin\theta = n\lambda \qquad (2.2)$$

where d is the interplanar spacing of the diffracting plane, θ is the angle of incidence, λ is the wavelength of incident X-ray beam, n is an integer representing diffraction order. The differential of Equation (2.2), which is in the form of Equation (2.3), can be used to calculate the lattice-mismatch between epitaxial layer and substrate.

$$\frac{\delta d}{d} = -\delta\theta\cot\theta \qquad (2.3)$$

Here $\delta\theta$ is the peak separation between the substrate and epitaxial layer. For symmetric (004) diffraction,

$$\frac{\delta d}{d} = \frac{\delta a}{a} \qquad (2.4)$$

where a is the lattice constant of the substrate. $\delta a/a$ is the lattice-mismatch between the epitaxial layer and substrate. However, for thin epitaxial layer (<0.1μm), Equation (2.3) becomes invalid [2.11, 2.12]. In this case, the mismatch has to be calculated by simulation.

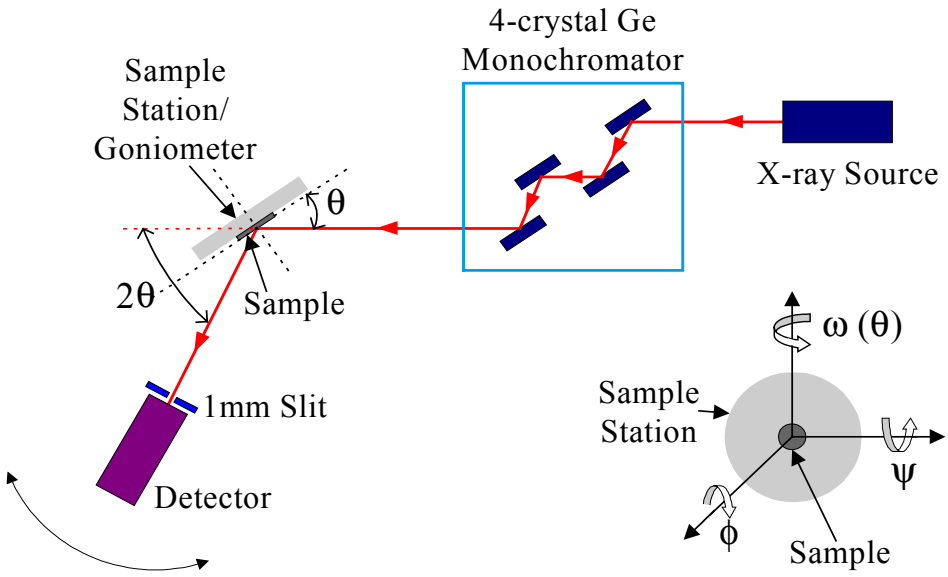

Figure 2.5: Schematic diagram of five-crystal Philips X'pert XRD system.

Figure 2.5 shows the schematic diagram of the five-crystal Philips X'pert XRD system in UT-Austin. The X-ray source uses Cu-K_α X-rays with a wavelength of 1.5406 Å. The X-ray beam goes through a Ge (220) 4-crystal

monochromator before hitting on the sample. Because the wavelengths and angles diffracted by the four crystals should strictly satisfy Bragg's law, the Ge (220) monochromator can control the divergence and wavelength spread of the X-ray beam. The diffracted X-ray beam is detected by the detector. The sample is attached on the sample station by transparent tape. The sample station and the rotation assembly are called goniometer. The goniometer is a four-axis system with 2θ, ω, ϕ and ψ as the variables. ω (often called θ) is the angle between the incident beam and the sample surface. It can be varied independently of 2θ, which is the angle between the incident beam and the diffracted beam. ϕ is the rotation angle about the sample normal and ψ is the tilt angle about a horizontal and centered line in the sample surface. With the detector set at a known Bragg angle, $2\theta_B$, a crystal is rotated through θ_B. The resulting intensity versus θ (or ω) curve is known as a rocking curve. By using the Bede Scientific RADS program, we can fit the experimental rocking curve with the simulated curve and obtain information such as alloy composition, layer thickness and relaxation.

Since the diffraction signal is proportional to the thickness of the semiconductor layer, it is difficult to accurately measure very thin film. For semiconductors that are not lattice-matched on the substrate, for example, $GaAs_{0.85}Sb_{0.15}$ on GaAs substrate, the critical thickness is only several nanometers. For such case, the X-ray sample has to use superlattice structure. Figure 2.6 shows the simulated X-ray rocking curve for a 5nm $GaAs_{0.85}Sb_{0.15}$/10nm GaAs 10-period superlattice structure on GaAs substrate.

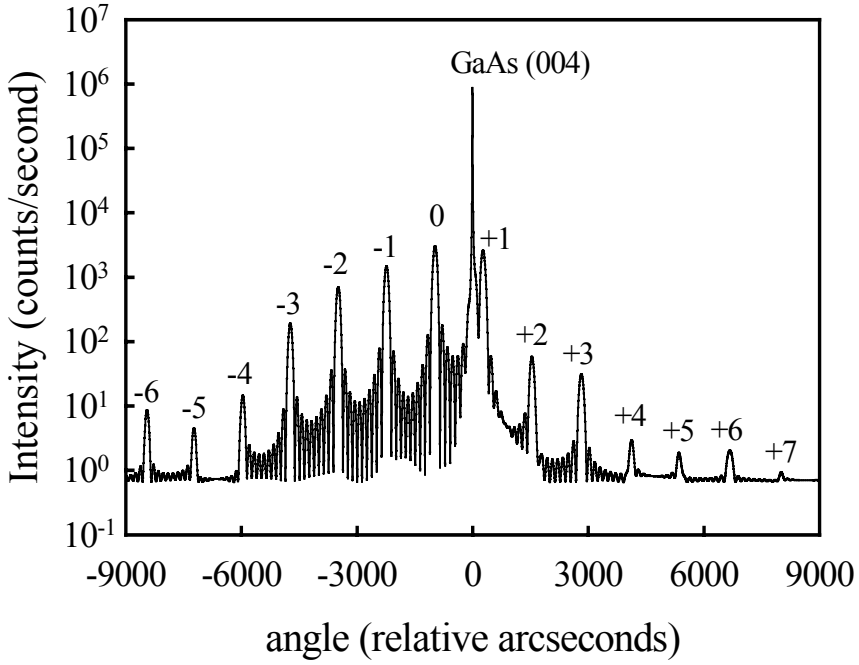

Figure 2.6: Simulated X-ray rocking curve for 5nm $GaAs_{0.85}Sb_{0.15}$/10nm GaAs 10-period superlattice structure on GaAs substrate.

The rocking curve shows the following features:

1. (004) peak from GaAs substrate.
2. Zero-order peak (average mismatch peak) caused by the addition of Bragg reflections from GaAs and $GaAs_{0.85}Sb_{0.15}$ layers. From this peak, the average composition of GaAs and $GaAs_{0.85}Sb_{0.15}$ layers can be obtained by the differential of Bragg's law (Equation 2.3 and 2.4).
3. A set of subsidiary "satellite"peaks symmetrically surrounding the zero-order peak (…-3, -2, -1, +1, +2, +3…). The spacing between subsidiary satellite peaks is determined by the thickness of the repeating layers.

4. The intensities and linewidths of the satellite peaks depend on the intereface sharpness, grading and epitaxial layer quality. For good quality epitaxial layers with abrupt interfaces, the satellite peaks are narrow, sharp and have high intensities.

The conjunct use of X-ray diffraction and photoluminescence provides a very strong tool in analyzing the band structure, alloy composition and layer quality of the compound semiconductor.

Chapter 3: MBE Growth of GaAsSb

3.1 INTRODUCTION

As discussed in Chapter 1, GaAsSb is a promising material for lasers and photodetectors operating at 1.3 μm on GaAs substrates due to the fact that it is easy to incorporate an arbitrary amount o Sb into GaAs lattice. It is not very easy to achieve by near-equilibrium growth techniques such as liquid phase epitaxy (LPE) due to the existence of thermodynamic miscibility gap [3.1]. But it can be grown by nonequilibrium crystal growth techniques such as MBE [3.2, 3.3, 3.4] and organometallic vapor phase epitaxy (OMVPE) [3.5, 3.6]. However, unlike III-V alloys such as $Al_xGa_{1-x}As$ and $In_xGa_{1-x}As$, mixed group-V alloys such as $GaAs_{1-x}Sb_x$ have the drawback that the control of the composition is much more difficult due to the strong competition between the incorporations of anions, which leads to different sticking coefficients of group-V species [3.7]. Figure 3.1 shows the band diagram of III-V semiconductors. We can see that the GaAsSb is not lattice-matched on GaAs substrates. To obtain 1.3 μm emission (~0.95 eV in bandgap), approximately 35% Sb should be incorporated into GaAs which produces ~2.7% compressive strain in the epitaxial layer. GaAsSb and AlAsSb can be grown lattice-matched on InP substrates as the distributed Bragg reflectors (DBRs) for resonant-cavity structures because the refractive index difference between these two materials is large [3.8, 3.9]. In this dissertation we mainly discuss the MBE growth of strained GaAsSb layers on GaAs substrates. The material quality and composition of GaAsSb layers highly depend on the growth

parameters, such as growth temperatures, Ga growth rates and Sb and As fluxes. Therefore, the growth of high quality GaAsSb epitaxial layers is very critical to the application of this material.

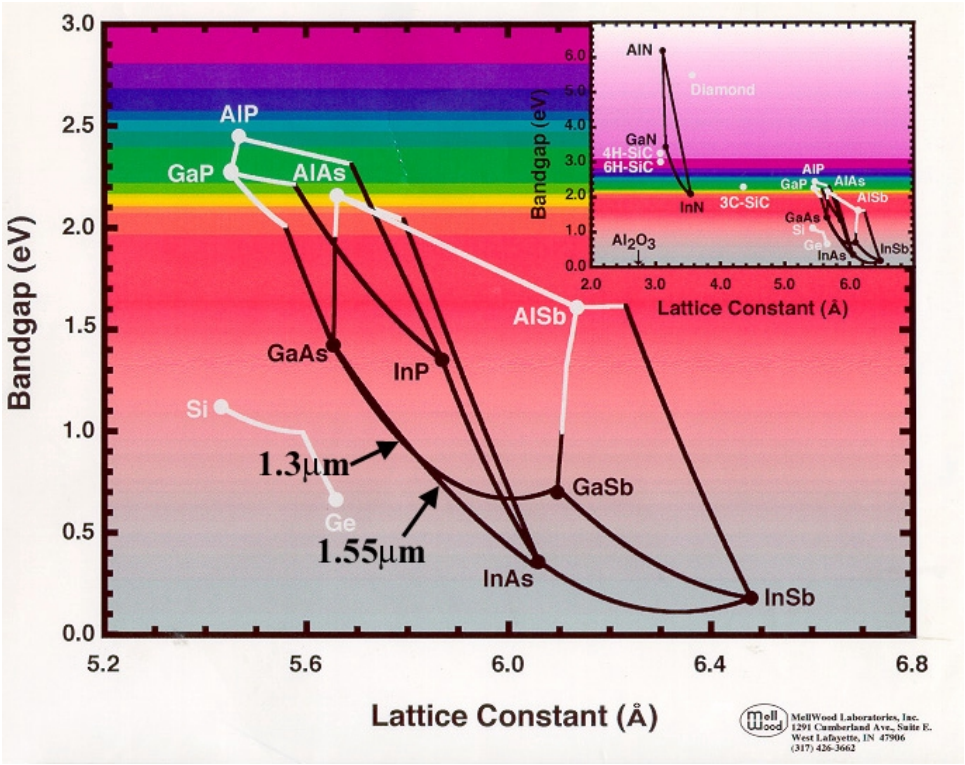

Figure 3.1: Band diagram of III-V semiconductors

3.2 SB VALVED CRACKER SOURCE

The Sb source in our MBE system is a Veeco-Applied Epi corrosive series valved cracker which was purchased and installed in 2000. It is designed to evaporate charge materials (Sb) that are too reactive for standard valved crackers.

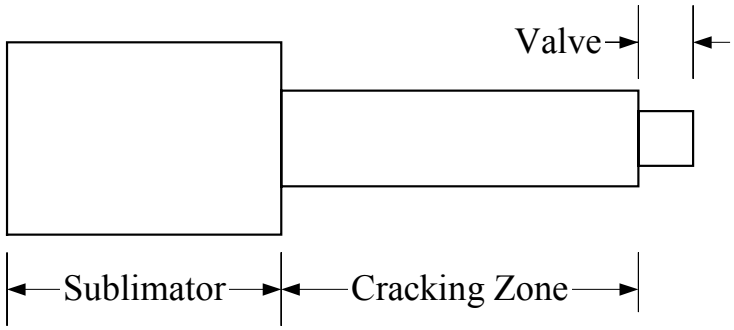

Figure 3.2: Schematic diagram of the cross section of Veeco-Applied Epi valved Sb cracker.

Figure 3.2 shows the schematic diagram of the cross section of this Sb cracker source. The sublimator's crucible, the valve and the cracker's conductance tube are entirely constructed by high-purity pyrolytic boron nitride (PBN) because of the corrosive nature of Sb. The bulk sublimator consists of a 200cm^3 PBN crucible containing the elemental Sb source material with a purity of 99.9999% and the heater assembly of alumina and tantalum that is regulated with W/Re thermocouple. The cracker is heated with a PBN and tantalum assembly and regulated with its own W/Re thermocouple. The cracker acts as a transfer tube for the Sb molecules to pass from the sublimator to the growth chamber. The initial tetramer Sb_4 molecules are dissociated into dimers (Sb_2) or monomers (Sb_1) in the cracking zone. The cracking zone is terminated by a valve fixture which can be used to regulate the Sb flux by opening or closing the valve without changing the sublimator temperature.

In Chapter 2, Section 2.1, we have mentioned that the use of smaller group-V molecules can significantly improve the incorporation efficiencies of group-V species into the epitaxial layers and may result in better crystal quality [3.10]. Thermal dissociation is the simplest way to crack bigger molecules into smaller ones. Ideally, atomic species such as Sb_1, As_1 and P_1 are desired. However, since many group-V species have high dissociation energies (see Table 3.1), extremely high temperatures are required to produce a substantial fraction of atomic N, P or As. At normal cracking temperature of 975°C, most of the As species are As_2. The dissociation energy of diatomic antimony (Sb_2) is much lower (~2.96 eV) than that of As_2. Therefore, it is possible to convert Sb_2 into Sb_1 at a cracking temperature around 950°C.

Table 3.1: Dissociation energies of different group-V species [3.11].

Group-V species	N_2	P_2	As_2	Sb_2
Dissociation energy (eV)	9.76	5.03	3.96	2.96

The relative amount of atomic Sb and different types of Sb molecules in the Sb flux can be measured by mass spectrometer. Figure 3.3 shows a mass spectrometer scan result of the MBE growth chamber when the Sb sublimator is 557°C, Sb cracker is 950°C and the valve is fully open. The maximum Sb flux is ~ 4.1×10^{-6} Torr as measured by ionization gauge. Due to the detecting limitation of our mass spectrometer, we can't measure the molecules with masses larger than 300 atomic mass units (AMUs). Sb has two isotopes with masses of 121 (57% of abundance) and 123 (43% of abundance) and Sb_2 has three different masses of 242, 244 and 246. The peak intensities of Sb_1 (121) and Sb_1 (123) are

much higher than those of Sb_2 (242), Sb_2 (244) and Sb_2 (246), which means that there are more Sb monomers (Sb_1) than Sb dimers (Sb_2) in the Sb flux. The peaks at 75, 150 and 225 are from residual As_1, As_2 and As_3 in the growth chamber. The "196" and "198" peaks are possible AsSb peaks.

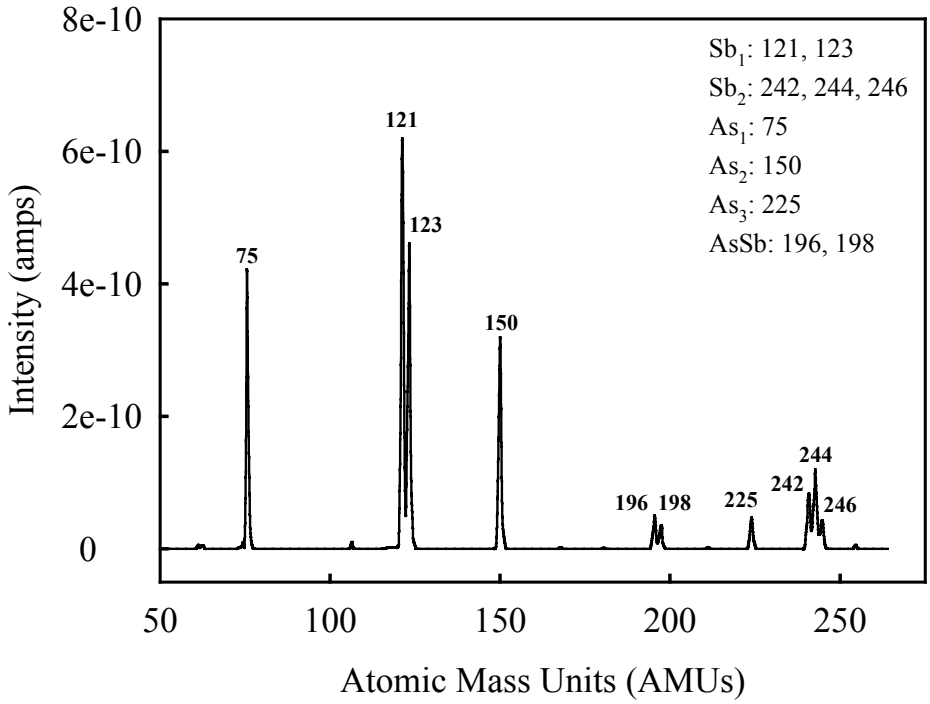

Figure 3.3: Mass spectrometer scan result of the MBE growth chamber. Sb sublimation temperature is 557°C, Sb cracking temperature is 950°C and the valve is fully open. The maximum Sb BEP is 4.1×10^{-6} Torr.

We cannot measure the Sb_3 and Sb_4 molecules directly by the mass spectrometer because their masses are larger than 300AMUs. But since the dissociation energies of Sb_3 and Sb_4 are much smaller than that of Sb_2 [3.12], at the cracking temperature of 950°C, there should have much less Sb_3 and Sb_4

molecules left than Sb_2. The mass spectrometer has already shown that there are more Sb_1 than Sb_2. Therefore, in the Sb flux, most of the Sb species are Sb_1.

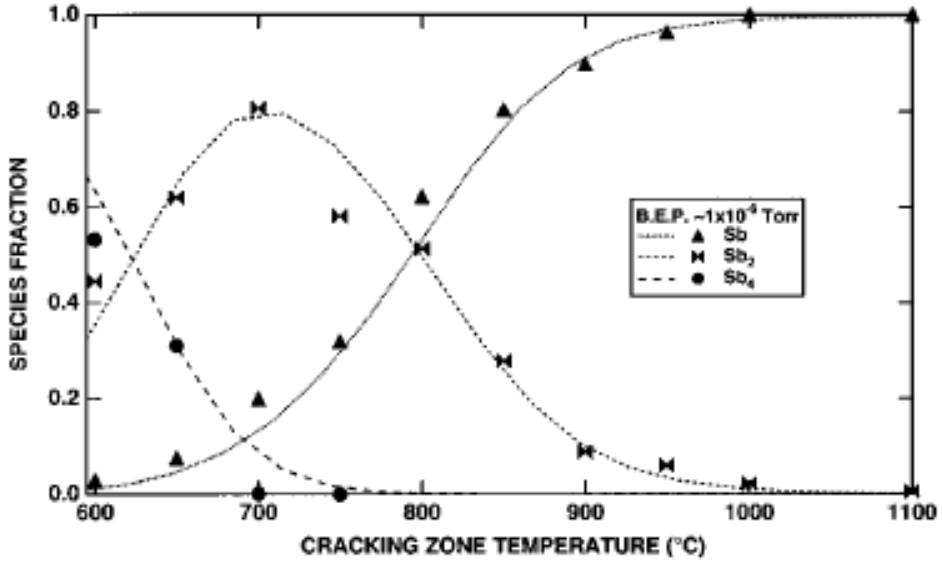

Figure 3.4: The product distribution of Veeco Applied-Epi Sb cracker source as a function of cracking zone temperature at beam equivalent pressure of 1.0×10^{-6} Torr. Experimentally measured values are indicated by solid symbols: Sb (triangles), Sb_2 (bow ties) and Sb_4 (circles). The dashed lines are calculated results [3.11].

Brewer *et al* [3.11] have also studied the product distribution of a Veeco-Applied Epi Sb valved cracker cell that is similar to ours, and the result is shown in Fig. 3.4. They found that tetrameric antimony Sb_4 is the major product produced at cracker temperatures lower than 650°C. At cracker temperatures between 650°C and 800°C, Sb_2 is the major product. Sb_1 becomes the major product at the cracking temperatures higher than 800°C. Our results are consistent with what they found.

In later chapters, I will show that our study requires a large amount of MBE growths of GaAs/$GaAs_{1-x}Sb_x$/GaAs multiple quantum well structures. In such growths the As and Sb fluxes need to be frequently changed because the growths of GaAs and GaAsSb layers require different As and Sb BEPs. To quickly change the As and Sb fluxes back and forth, a Veeco-Applied Epi automatic valve positioner was used for both As and Sb valves. The reproducibility of opening and closing movements of the valves are very important because the compositions of GaAsSb layers highly depend on the As and Sb fluxes. Figure 3.5 shows the As and Sb BEPs as a function of valve position over the entire regime of interest. Both As and Sb valves exhibit some mechanical backlash, which leads to As and Sb flux offsets during the opening and closing operations. However, the As valve behaves pretty good in the BEP range from 2.0×10^{-6} Torr to 6.0×10^{-6} Torr which we are most interested in. The Sb BEP that we are interested in is from 4.0×10^{-7} Torr to 8.0×10^{-7} Torr. Even though the Sb vavle exhibits some offset in this range, it is not a big issue because the growth of GaAs/GaAsSb/GaAs multiple quantum wells doesn't require frequent Sb valve operation. We only need to open the Sb shutter to provide the Sb flux during the growth of GaAsSb layers and close the Sb shutter to turn off the Sb flux during the growth of GaAs layers without valve operations.

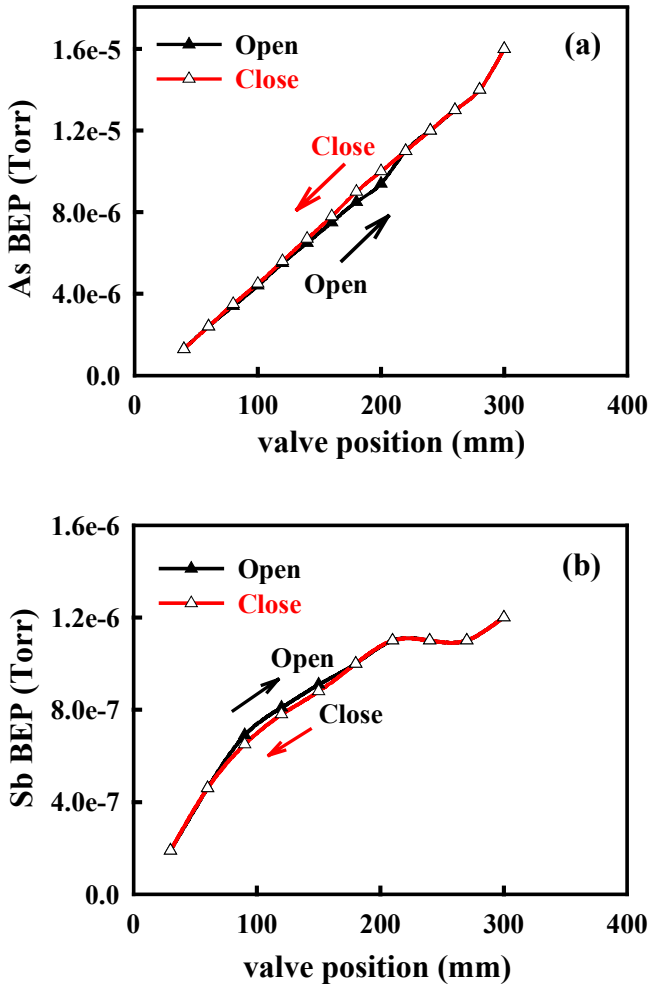

Figure 3.5: As and Sb fluxes as a function of valve position for both opening and closing operations. (a) As valve characteristics, (b) Sb valve characteristics.

3.3 MBE GROWTH OF GAASSB

3.3.1 Composition Control of $GaAs_{1-x}Sb_x$

The growth rates of group-III species such as Ga, Al and In can be calibrated by RHEED oscillations under group-V overpressure. Since the surface

sticking coefficients of group-III species are near unity, the composition of III-III`-V alloys such as $Al_xGa_{1-x}As$ can be determined by the growth rates of Al and Ga. $GaAs_{1-x}Sb_x$ has two group-V elements. The Sb and As growth rates can also be measured by group-V induced RHEED oscillations while maintaining a Ga overpressure during the growth [3.13]. But As and Sb have different sticking coefficients on group-V stabilized surface and the sticking coefficients of Sb and As are not unity. There is strong competition between the incorporations of Sb and As atoms with Ga atoms and the Sb and As mole fractions in the $GaAs_{1-x}Sb_x$ layer are determined by this competition. Therefore the individual growth rates of As and Sb can not tell us the composition of $GaAs_{1-x}Sb_x$ layers. R. Evans *et al* [3.14] described a method to determine the Sb incorporation rates during the MBE growth of GaAsSb via mass-spectrometric measurements of the non-incorporated fraction of the incident Sb flux. But this method is quite complex and time-consuming. In our study, we use Sb and As beam equivalent pressures instead of the growth rates for the composition control. The GaAsSb layer is grown under a mixed As/Sb flux with different As and Sb BEPs. After the growth, photoluminescence is used to determine the emission wavelength and study the optical properties of the grown layers. The GaAsSb composition is measured by x-ray diffraction and simulation. The advantage of this method is that we can directly measure the Sb and As BEPs by ionization gauge and therefore the calibration procedures are significantly simplified. The disadvantage is that the repeatability of the growth highly depends on the accuracy of the ionization gauge.

3.3.2 Sample Preparation

In our study, all the materials were grown on American Xtal Technology (AXT) (100)-oriented semi-insulating (SI) GaAs substrates. These substrates are so-called "epi-ready" wafers that are pre-cleaned and oxidized in a controlled environment. The surface oxide layer provides a protection for the substrate and can be removed thermally inside the growth chamber. The 2" wafers are cleaved into smaller pieces and then mounted on molybdenum sample blocks by using molten indium (In) as bonding adhesive. The molybdenum blocks don't outgas or decompose up to 1400 °C. The molten In should be spread uniformly on the block surface. Otherwise, it may cause temperature non-uniformity across the wafer. This step is very important, especially for the growth of GaAsSb because the thermal gradient on the substrate surface will result in GaAsSb layers with different Sb compositions across the wafer.

The mounted samples are placed in the load lock and heated by a heat lamp at a temperature around 150 °C under vacuum overnight to remove H_2O vapor. The samples are further out-gassed on the heat station inside the buffer chamber at 450 °C. The out-gassed samples are transferred into the growth chamber and placed on the CAR assembly via a magnetically coupled transfer rod. The substrate is heated to 450 °C directly without opening the As shutter and then ramped up at a rate of 10 °C/min with an As overpressure of ~5.5×10^{-6} Torr. Above 550°C, the ramp-up rate is slowed down to 5 °C/min and the temperature holds for 5 minutes for every 5 °C increase until the deoxidation pattern is seen. The substrate temperature is increased 50 °C above the deoxidation temperature

for 3 minutes and then decreased back to the deoxidation temperature to ensure that all traces of the oxides are removed. The temperatures are measured by thermocouple which has some offsets with the real surface temperatures. Because the deoxidation temperature of GaAs wafers is 580 °C, it can be used as a temperature reference for the GaAsSb growth. The same deoxidation procedure is used to obtain reproducible results.

3.3.3 Sb Segregation

The interface between ternary and binary III-V compound semiconductors is often compositionally broadened due to the surface segregation of the more weakly bound species occupying the shared sublattice of the ternary alloy [3.15, 3.16]. Compositional broadening occurs as a result of the gradual buildup or decay of surface accumulation of this species near the interface. Group-III atom segregation (e.g., Ga on AlGaAs, In on InGaAs, In on InGaP, etc.) has been excessively studied.

The success of GaAsSb/GaAs photodetectors or lasers requires abrupt interfaces between As- and Sb-containing layers. However, since Sb is more volatile that As [3.17], the weakly bonded Sb atoms tend to segregate at the GaAs/GaAsSb interfaces. Figure 3.6 shows the schematic drawing of the Sb segregation at GaAsSb/GaAs interface. The Sb segregation causes a “Sb floating layer” on GaAsSb surface which leads to a compositionally broadened interface between GaAs and GaAsSb layers. The Sb segregation effect depends on several factors such as the growth temperature and the growth method. The growth temperature dependence of the Sb segregation will be discussed in next section.

By choosing appropriate growth method, the Sb segregation effect can be reduced.

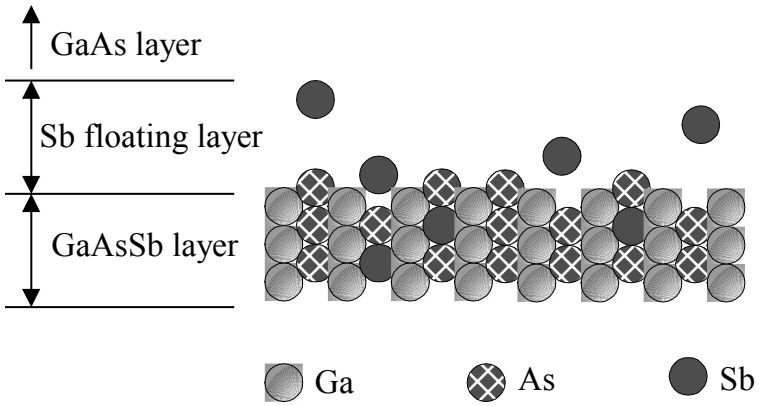

Figure 3.6: Schematic drawing of the Sb segregation at GaAsSb/GaAs interface.

Here we use the growth of photoluminescence structures as an example. Figure 3.7 shows the layer structure of PL samples with GaAsSb/GaAs single or multiple quantum wells. The $Al_xGa_{1-x}As$ layers are for carrier confinement. The GaAsSb quantum wells and GaAs embedded barrier layers are grown at temperatures around 500°C~530°C. The $Al_xGa_{1-x}As$ confinement layers, the GaAs cap layers and the GaAs barriers are grown at the deoxidation temperature of 580°C. The GaAsSb layers are grown under a group-V mixed flux with Sb BEP of ~5.0×10^{-7} Torr and As BEP of ~2.5×10^{-6} Torr. All the GaAs and $Al_xGa_{1-x}As$ layers are grown under a group-V overpressure with As BEP of ~5.5×10^{-6} Torr.

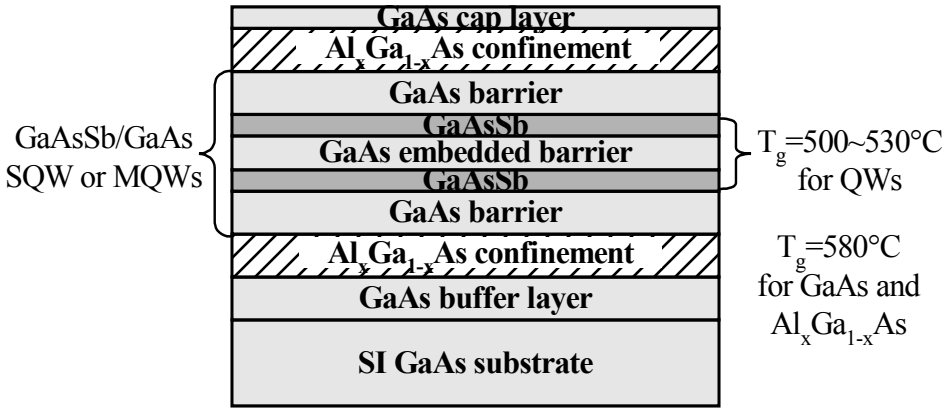

Figure 3.7: Layer structure of the photoluminescence samples with GaAs/GaAsSb single or multiple quantum wells.

Figure 3.8 shows the shutter sequence during the growth of a GaAs/GaAsSb PL structure. When growing the first GaAs layer, the Ga and As shutters are opened and the As BEP is 5.5×10^{-6} Torr. After finishing the first GaAs layer, the Ga shutter is closed, the Sb shutter is opened to provide 5.0×10^{-7} Torr Sb flux and As BEP is lowered down to 2.5×10^{-6} Torr by closing the As valve. The growth is interrupted for 5 seconds to let the As and Sb fluxes stabilize. Then the Ga shutter is opened to grow the GaAsSb layer. After the growth of GaAsSb layer, the Ga and Sb shutters are closed and the As BEP is increased back to 5.5×10^{-6} Torr by opening the As valve. To reduce the Sb segregation at GaAsSb/GaAs interface, the growth is interrupted for 5 seconds before the growth of next GaAs layer to expose the GaAsSb surface to the As flux which purges the Sb floating layer away. Then the next GaAs layer is grown. By using such growth procedure, the Sb segregation effect can be reduced.

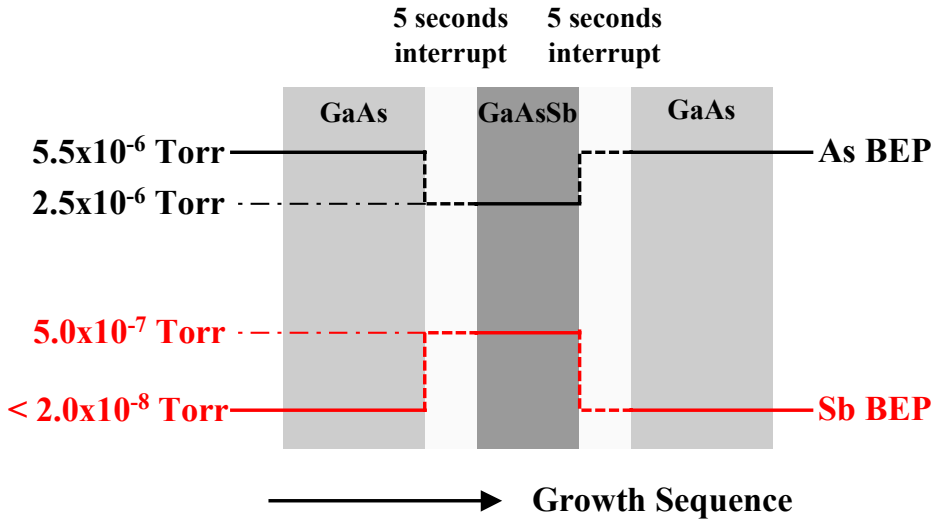

Figure 3.8: Shutter sequence during the growth of GaAs/GaAsSb PL structure.

3.3.4 Influences of Growth Temperature

Growth temperature has been found to be one of the most important factors influencing the alloy composition and optical properties of MBE grown GaAsSb layers [3.18, 3.19]. A series of GaAs/GaAsSb PL samples (structures are shown in Fig. 3.7) with 4.2 nm-thick GaAsSb quantum wells and 10 nm-thick GaAs barriers were grown on SI-GaAs (001) substrates. The GaAsSb layers were grown at different temperatures between 490°C and 545°C under the same As flux of 2.5×10^{-6} Torr and the same Sb flux of 5.0×10^{-7} Torr. The As sublimator was ~380 °C and As cracker was ~975 °C, which produced mainly As_2 species. The Sb sublimator was ~500 °C and Sb cracker was ~950 °C, which produced mainly Sb_1.

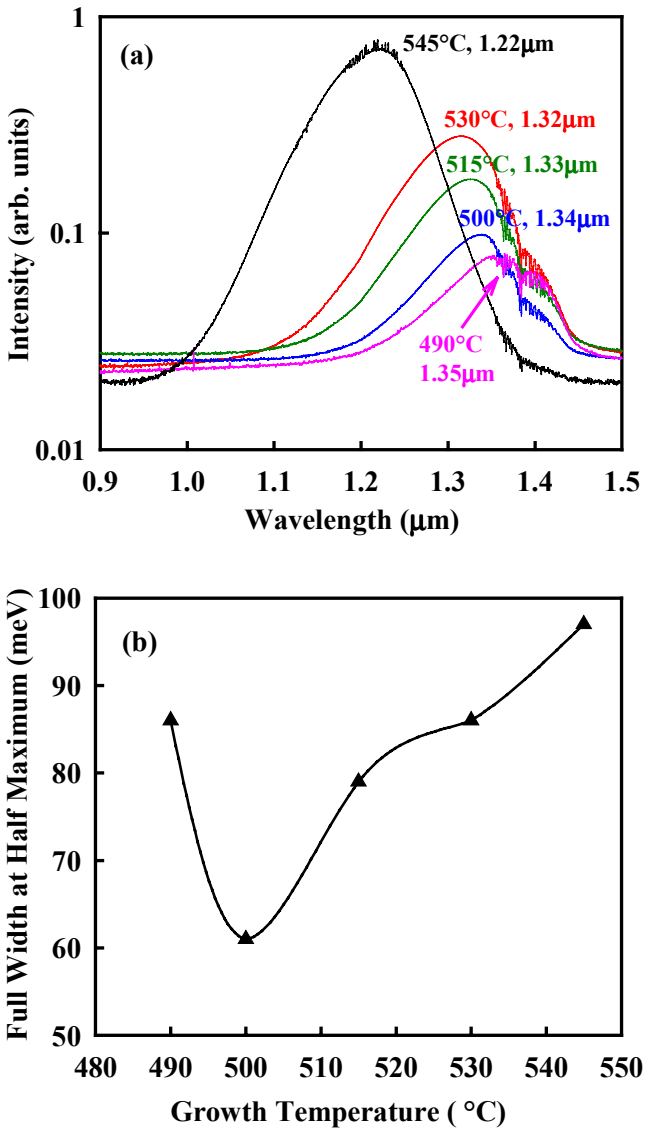

Figure 3.9: (a) 300K PL comparison of GaAs/GaAsSb (4.2nm)/GaAs SQW structures grown at different temperatures. (b) PL linewidths as a function of growth temperatures for the above samples.

The room temperature (300K) photoluminescence results are shown in Fig. 3.9 (a). From the PL results, we can see that, for nominally identical structures, higher growth temperatures produce higher PL intensities and shorter emission wavelengths. When a mixed flux of Ga, Sb and As atoms or molecules impinges on the underlying GaAs lattice, there are two processes related to Sb atoms: Sb incorporation with Ga and As to form GaAsSb and Sb desorption from the surface. The final Sb mole fraction in the GaAsSb film is the net result of the two competitive processes. With an increase in growth temperature, the Sb desorption rate increases and Sb incorporation rate with Ga decreases, which results in smaller Sb mole fraction in the GaAsSb layers. The GaAsSb layers with smaller Sb mole fractions have wider bandgaps and thus shorter emission wavelengths. The increase in PL intensity at higher growth temperatures is associated with the decrease in the density of point defects as well as the decrease of strain-induced defects such as dislocations in the GaAsSb films. At the same growth temperatures, we can shift the PL peaks to longer wavelengths by using higher Sb fluxes but the PL intensities drop dramatically. Therefore, we believe that the amount of compressive-strain-induced defects plays a more important role than the density of point defects in the PL intensity change of GaAsSb films.

Figure 3.9 (b) shows the full width at half maximums (FWHMs) of the PL curves in Fig. 3.9 (a) as a function of growth temperature. The PL linewidths range from 61meV to 97meV. At too high of growth temperature, the PL linewidth increases. We believe this is due to the Sb segregation effect at the GaAs/GaAsSb interface which was mentioned in Section 3.3.3. At too low of

growth temperature, the surface mobility of Ga atoms is too low which results in more growth defects and degradation in crystalline quality. The more growth defects in the GaAsSb layers cause a broadening of the PL linewidth at low growth temperatures. Considering all the factors, an optimized growth temperature window of GaAsSb between 500°C and 530°C was chosen for further experimentation.

X-ray diffraction samples with 5 nm GaAsSb/10 nm GaAs 10-period superlattice structures were grown at the same growth conditions as the PL samples. Figure 3.10 shows the measured and simulated X-ray rocking curves of the sample grown at 500°C with As BEP of 2.5×10^{-6} Torr and Sb BEP of 5.0×10^{-7} Torr. The Sb mole fraction is 36.3% from the simulation.

To prevent the relaxation of the strained GaAsSb layers, the thickness of the GaAsSb quantum wells should be within the critical thickness limitation. The RHEED pattern becomes dim when depositing GaAsSb and then recovers after the growth of GaAs barrier if the GaAsSb layer is thinner than the critical thickness. Beyond the critical thickness, RHEED pattern suddenly switches to spots along [011] direction and chevrons along [$01\bar{1}$] direction which cannot recover even after the growth of a thicker GaAs layer. The change in diffraction pattern results from a faceted surface induced by the compressive strain with higher index planes coexisting with the (001) plane [3.4].

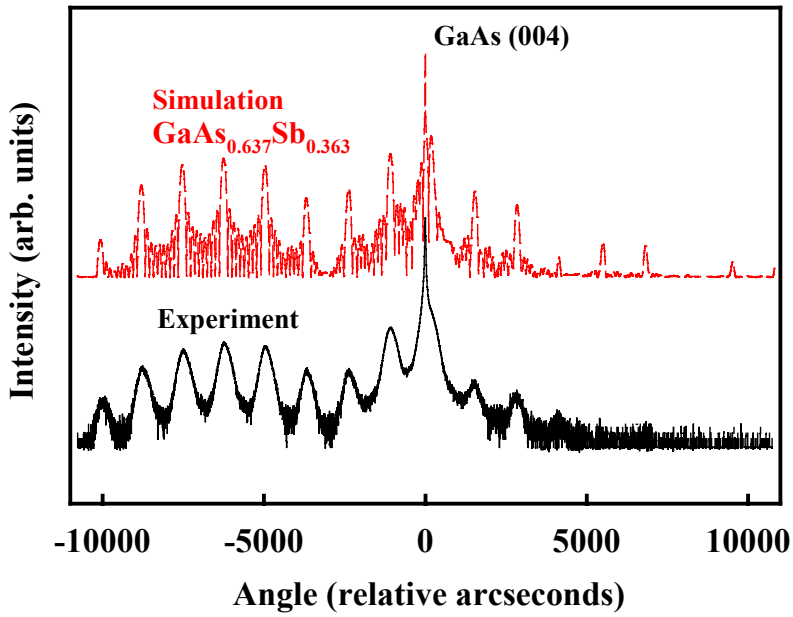

Figure 3.10: Measured and simulated X-ray rocking curves of 5nm GaAsSb/10nm GaAs 10-period superlattice structure grown at 500°C with As BEP of 2.5×10^{-6} Torr and Sb BEP of 5.0×10^{-7} Torr.

3.3.5 Influences of Ga Flux

For given As and Sb fluxes, the group-III Ga flux also affects the Sb incorporation and epitaxial layer quality. Here we use the Ga growth rates (ml/s) on GaAs substrates as an indication of the Ga flux. Figure 3.11 (a) shows the 300K PL comparison of GaAs/GaAsSb (5nm)/GaAs SQW structures grown at different Ga growth rates and Fig. 3.11 (b) plots the emission wavelengths as a function of Ga growth rates.

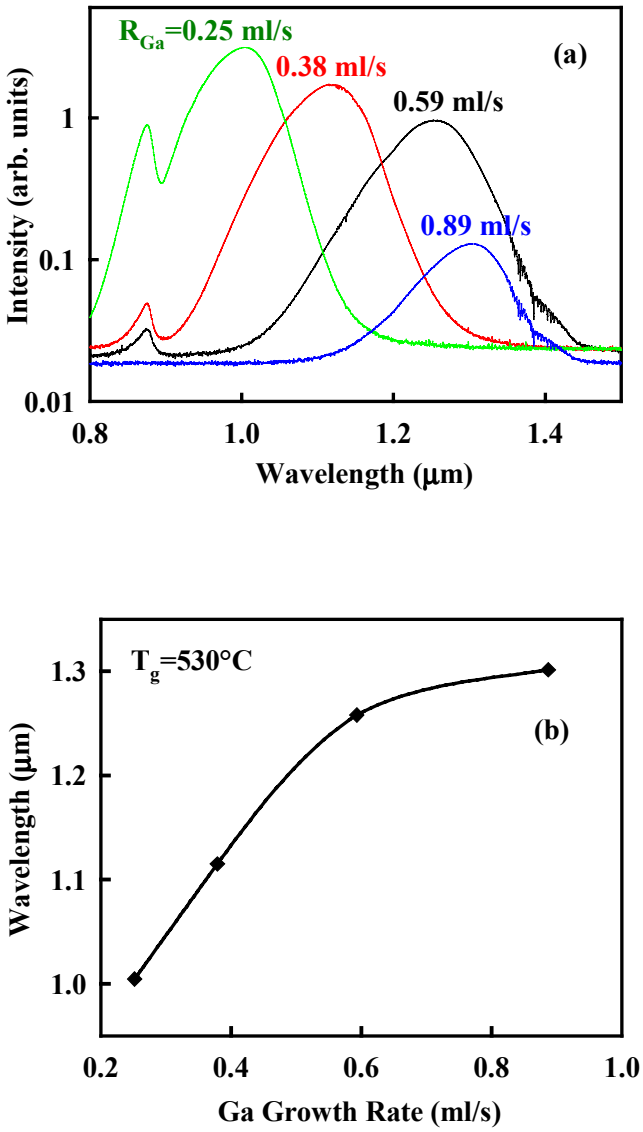

Figure 3.11 (a): 300 K PL comparison of GaAs/GaAsSb (5nm)/GaA SQW structures grown at different Ga growth rates. (b): emission wavelengths vs. Ga growth rates. T_g=530°C, As BEP=2.5×10^{-6} Torr, Sb BEP=5.0×10^{-7} Torr for the QW region.

From Fig. 3.11, we can see that at the same growth temperature (530°C), the same As flux ($2.5x10^{-6}$ Torr) and Sb flux ($5.0x10^{-7}$ Torr), the Ga growth rates of 0.25ml/s, 0.38ml/s, 0.59ml/s and 0.89ml/s result in GaAsSb layers with Sb compositions that can emit light at 1.00μm, 1.12μm, 1.26μm and 1.30μm, respectively. Higher Ga fluxes lead to larger Sb incorporation rates into GaAsSb layers and longer PL wavelengths. One possible reason is that at higher Ga growth rates, there are more Ga atoms available for Sb atoms to bond with, which prevents the Sb desorption from the surface. This result is consistent with the literatures [3.7, 3.20]. From Fig. 3.11 (b), we can clearly see that the emission wavelengths saturate at higher Ga growth rates (>0.8ml/s), which means a saturation of Sb incorporation with Ga atoms. Therefore, in the MBE growth of GaAsSb, it is better to keep the Ga growth rates higher than 0.8 ml/s in order to eliminate the Ga flux influences to the composition of GaAsSb layers.

3.3.6 Influences of As and Sb Fluxes

We have mentioned that due to the strong competition and different sticking coefficients of As and Sb atoms with Ga, the composition of GaAsSb alloy highly depends on the Sb and As fluxes. Figure 3.12 (a) shows the 300K PL comparison of GaAs/GaAsSb (5nm)/GaAs three quantum well (3QW) samples grown at the same temperature (530°C) and the same Ga growth rate (~0.9ml/s). The As and Sb BEPs were different for these samples but the Sb/As ratios were the same (Sb/As=0.2). In other words, 16.7% of the group-V BEP was due to Sb flux. From the PL results, we can see that even the Sb/As ratios were the same, the resulted GaAsSb layers still had different compositions corresponding to

emission wavelengths from 1.11μm to 1.31μm. The higher the As flux in the group-V mixture, the shorter the emission wavelength and the smaller the Sb mole fraction in the GaAsSb film. Figure 3.12 (b) shows the x-ray rocking curves of these 3QW PL samples and the Sb compositions were from simulations. From these results, we know that 16.7% Sb in As/Sb mixture resulted in 24%, 29%, and 36% Sb mole fractions in the GaAsSb films under different group-V fluxes. This means that Sb incorporates with Ga preferentially at these growth conditions. However, with the increase of As flux, the Sb incorporation rate decreases. We can predict that at very high As flux, the As will become the more preferential species to incorporate with Ga atoms.

During the growth of GaAsSb, a group-V overpressure is required to prevent the surface from Ga-rich. However, if the As and Sb pressures are too high, the Ga surface mobility will decrease, which leads to more growth defects. But if the group-V flux is too low, we can't keep the surface group-V-stabilized. This will also cause more growth defects. Our study shows that for better PL results, lower As and Sb mixed flux is desired as long as the surface is group-V stabilized. At the growth temperature of ~530°C and Ga growth rate of ~0.9ml/s, the optimized As and Sb mixed flux is ~3.0×10^{-6} Torr.

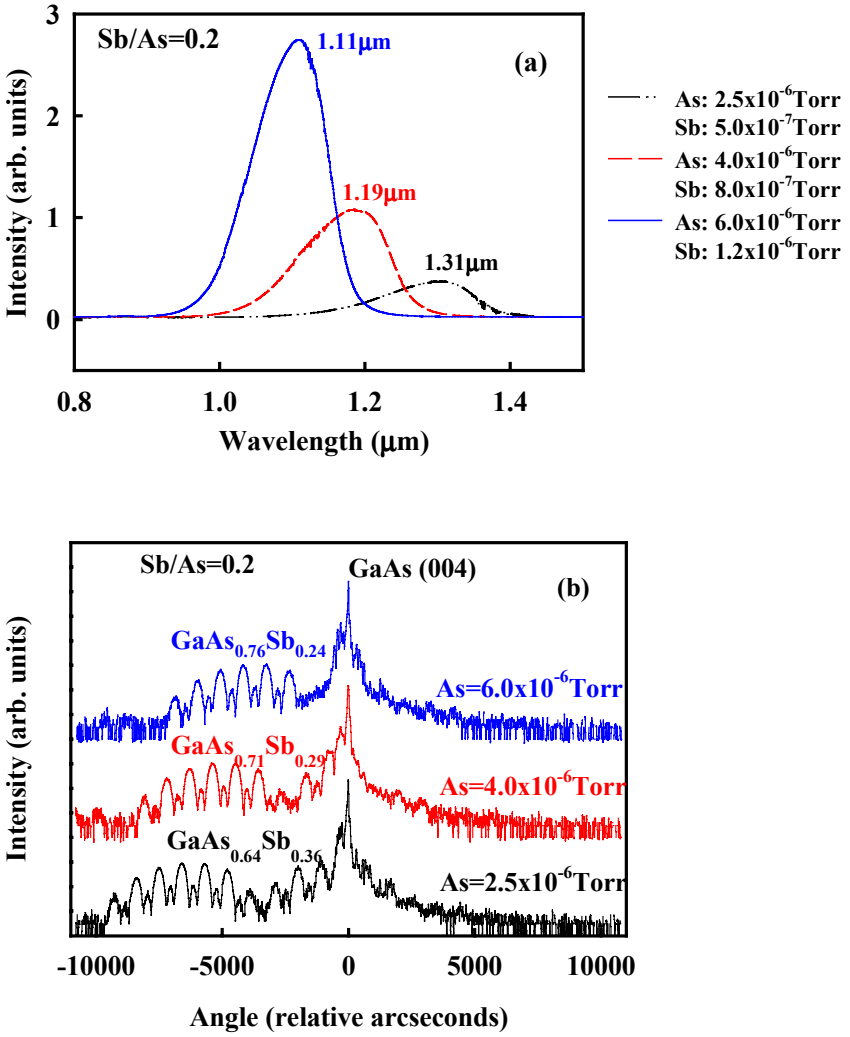

Figure 3.12 (a): 300K PL comparison of GaAs/GaAsSb(5nm)/GaAs three quantum well (3QW) samples. T_g=530°C, R_{Ga}=0.9ml/s. (b): x-ray rocking curves of these 3QW PL samples.

3.4 SUMMARY

We have studied the MBE growth of GaAsSb layers on GaAs substrates. Our experiments show that the optical quality and composition of GaAsSb layers highly depend on the growth temperatures, the Ga growth rates and the As and Sb

fluxes. With the increase of growth temperatures, the Sb desorption from the surface increases and incorporation with Ga decreases, the point defects decrease, and the Sb segregation increases. The optimum growth temperature window of GaAsSb on GaAs substrates is from 500ºC to 530ºC. The Sb incorporation with Ga increases at higher Ga fluxes and saturates at Ga growth rates higher than 0.8 ml/s. The optimum Ga growth rate is 0.8 ml/s to 1.0 ml/s. With the same Sb/As ratio, Sb incorporates with Ga preferentially when As flux is low and As incorporates with Ga preferentially when As flux is high.

Chapter 4: Photodetectors

4.1 INTRODUCTION

Photodetectors are the essential parts of the modern fiber optic communication systems because they covert optical signals into electrical signals at the receiving end. There are generally three steps involved in the photo-detection process:

1. Absorption of optical energy and generation of carriers (electron-hole pairs);
2. Transportation of photo-generated carriers across the absorption and/or transit region with or without gain;
3. Carrier collection and generation of photocurrent which flows through the external circuits.

In this chapter, we will discuss some of the performance parameters of photodetectors such as operating wavelength, responsivity, noise and bandwidth. Different types of photodetectors and resonant cavity structures will also be discussed.

4.2 KEY PERFORMANCE PARAMETERS OF PHOTODETECTORS

4.2.1 Operating Wavelength

The operating wavelengths of photodetectors are determined by the bandgaps of the absorption materials. The optical signals generated by the transmitters travel through optical fibers to the receivers. Optical fibers can

transmit light over a wide range of wavelengths. For short distances, low cost optical communication systems such as local area networks (LAN), the operating wavelength of light is typically less than 1μm in order to take advantage of the well developed and inexpensive $Al_xGa_{1-x}As$ light sources and Si or $Al_xGa_{1-x}As$ photodetectors. For high speed, long-haul communication applications, operating at the wavelengths of 1.3 μm or 1.55 μm are very attractive for both lasers and photodetectors because silica-based optical fibers have minimum dispersion and attenuation at these wavelengths [4.1]. This dissertation is mainly focused on the development of 1.3 μm photodetectors grown on GaAs substrates.

4.2.2 Responsivity

Responsivity is perhaps the most fundamental parameter of photodetector because it is a measure of how well the photodiode converts the incident optical signal into electric current. The responsivity *R* is defined as the current generated by unit incident light power in units of A/W. But usually we use quantum efficiency to describe the conversion efficiency of photodetectors. The internal quantum efficiency (η_i) is the number of electron-hole pairs created divided by the number of photons absorbed and is near unity in pure, defect-free materials. The external quantum efficiency (η_{ext}), which we are most interested in, is defined as the number of carriers collected to produce the photocurrent divided by the number of incident photons. It can be expressed as:

$$\eta_{ext} = \frac{I_{ph}/q}{P_{inc}/h\nu} = \frac{I_{ph}}{P_{inc}} \cdot \frac{h\nu}{q} = \frac{h\nu}{q} \cdot R \qquad (4.1)$$

where I_{ph} is the photocurrent, P_{inc} is the incident optical power, q is the electron charge, hv is the photon energy and R is the responsivity [4.2]. The external quantum efficiency depends on the absorption coefficient of the material and the thickness of the absorbing layer:

$$\eta_{ext} \propto \left(1 - e^{-\alpha d}\right) \tag{4.2}$$

where α is the absorption coefficient of the material and d is the thickness of the absorbing layer. For a given absorption material, we can obtain higher quantum efficiency by using thicker absorption layer. But this will degrade the speed performance. For absorption materials such as $GaAs_{1-x}Sb_x$ and $In_xGa_{1-x}As$ which are not lattice-matched on GaAs substrates, only thin absorbing layers can be grown. In these cases, waveguide or resonant-cavity structure must be utilized to achieve the high responsivity needed.

4.2.3 Noise

The noise of the photodetector is a very crucial factor in designing and determining the performance limits of lightwave systems because it causes fluctuations in the output that cannot be distinguished from the actual signal. High signal-to-noise ratio *S/N* is especially important for photodetectors used in high bit-rate, long-haul fiber optic communication systems in order to reduce the number of repeaters and amplifiers as well as the bit-errors during the transmission. There are many sources of noise in photodetectors such as shot noise, Johnson noise, background radiation noise, dark current noise and *1/f* noise [4.3]. For photodetectors operating at high frequency, Johnson noise and shot noise are the dominant noise sources.

Shot noise is a fundamental noise that exists in all optical detection processes. When optical power is detected, it arrives in discrete photons. Each photon arrives randomly and produces a current of one electron if the external quantum efficiency is unity. This randomness in arrival leads to fluctuations in the signal, which is called shot noise. Noise is usually described as the quadratic mean of noise current $<i^2>$. Shot noise can be expressed as:

$$\left\langle i^2{}_{shot} \right\rangle = 2qIB \qquad (4.3)$$

where q is the electron charge, I is the current and B is the effective bandwidth.

Johnson noise, which is sometimes called circuit noise or thermal noise, arises from the random motion of electrons in resistors. Random thermal motion of the electrons can lead to excess charge accumulating momentarily at one end of a resistor. This leads to small voltage differences and currents. The Johnson noise can be presented as:

$$\left\langle i^2{}_{Johnson} \right\rangle = \frac{4kT}{R} \cdot B \qquad (4.4)$$

where T is the absolute temperature, R is the load resistance and k is the Boltzmann's constant. Low temperature and high load resistance can reduce the Johnson noise of photodetectors. However cryogenic operation is usually impractical for optical communication systems. High R will reduce the speed of the circuit due to RC limitation.

Johnson noise and shot noise are intrinsic noise sources and cannot be eliminated. Because these two noise sources are statistically independent, the total noise can be expressed as:

$$\left\langle i^2{}_{total} \right\rangle = \left\langle i^2{}_{shot} \right\rangle + \left\langle i^2{}_{Johnson} \right\rangle = 2qIB + \frac{4kT}{R} \cdot B \qquad (4.5)$$

4.2.4 Bandwidth

High bandwidth is another important requirement for photodetectors used in high-speed, long-distance fiber optic communication systems because the bandwidth of every component must be sufficient to accommodate the transmission rate. Typically this means that the bandwidth must be slightly larger than half of the bit rate. The bandwidth-limiting mechanisms of photodetectors include *RC* time constant, carrier trapping at the heterojunction interfaces, carrier transit time and carrier diffusion time.

Reduction of the *RC* effect can be accomplished by using substrates with low resistance and scaling the device dimensions to minimize the capacitance. Carrier trapping can be reduced by grading the heterojunction interfaces to remove the large band discontinuities with one or more intermediate-bandgap layers. Carrier transit time is the time that carriers travel through the depleted absorption region and it can be reduced by using thin absorbing layer. But thin absorbing layers lead to low quantum efficiency. Waveguide or resonant-cavity structure can be a solution to the tradeoff between speed and responsivity. In photodetection process, the photogenerated carriers must diffuse to the junction and be swept across to the other side. The carrier diffusion process is time consuming. For modern high-speed photodetectors, the absorption region is generally designed to be located in the high-field intrinsic region to eliminate the carrier diffusion processes.

4.3 PIN PHOTODIODES

There are several types of photodiodes that have been developed for lightwave applications such as photoconductor, metal-semiconductor-metal (MSM), PIN and avalanche photodiodes. PIN and avalanche photodiodes are the two dominant ones used in the front-end circuits of commercially available optical receivers.

The PIN photodiode is a junction diode with an undoped *i*-region (p^- or n^-, depending on the method of junction formation) inserted between P^+ and N^+ regions. Because of the very low density of free carriers in the *i*-region and its high resistivity, any applied bias drops almost entirely across the *i*-layer, which is fully depleted at zero or very low reverse bias. The PIN photodiode operates at low bias without internal gain. It has a controlled depletion layer width, which can be tailored to meet the requirements of photoresponse and bandwidth. For high speed, the depletion layer width should be small and for high quantum efficiency, the width should be large. Therefore, a tradeoff is necessary. Figure 4.1 shows the absorption and carrier generation processes in a PIN photodiode.

There are several physical effects, such as incomplete absorption, recombination, reflection from the semiconductor surface and contact shadowing that tend to reduce the quantum efficiency. Heterojunctions provide a convenient method to reduce two components of recombination. In a well-designed photodetector, most of the incident light is absorbed in the depletion region where the electric field quickly separates the photogenerated electrons and holes before

they recombine. Carriers generated outside the space charge region can recombine before collection thus degrading the responsivity.

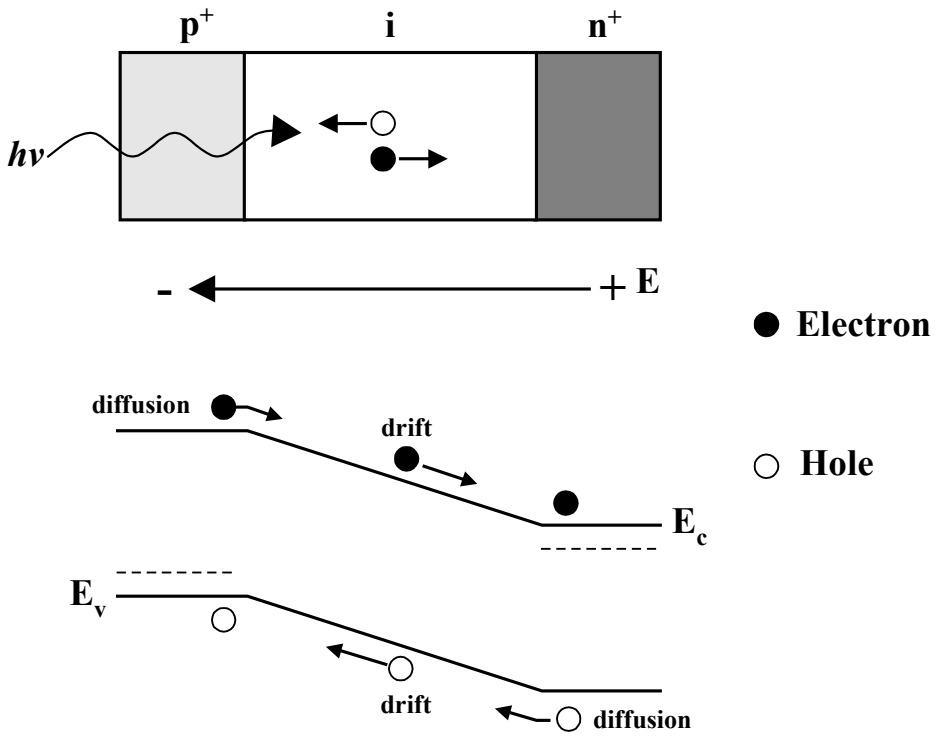

Figure 4.1: The absorption and carrier generation processes in a PIN photodiode.

By utilizing wide-bandgap window layers adjacent to the absorption layer, with sufficient bias to fully deplete the absorption layer, this type of recombination can be eliminated. Surface recombination is a more serious problem. If the electron-hole pairs are generated near a semiconductor/air interface, a large fraction of the carriers will recombine through surface states. Since the surface recombination velocity at the interface between two semiconductors, such as InP/$In_{0.53}Ga_{0.47}As$

interface, is much smaller than that at the semiconductor/air interface, the incorporation of a wide-bandgap window layer can significantly reduce the surface recombination and improve the quantum efficiency. The external quantum efficiency of PIN photodiode is given by:

$$\eta_{ext} = (1-R)(1-e^{-\alpha d}) \cdot \frac{S}{A} \qquad (4.6)$$

where R is the reflectivity at the surface, S is the optically sensitive portion of the photodetector, A is the total photodetector area, α is the absorption coefficient and d is the absorption layer thickness. For most PIN photodiodes, the contact shadowing is negligible, i. e., $S/A \approx 1$. Semiconductors reflect approximately 30% of the incident light (R = 0.3). By using antireflection (AR) coatings, R can be reduced to less than 5%.

The design of PIN photodiode with low noise and high bandwidth follows the rules in section 4.2.3 and 4.2.4.

4.4 AVALANCHE PHOTODIODES

4.4.1 Impact Ionization Process

The PIN photodiode is widely used in optical communication systems due to its low noise, high speed and low dark current. It operates at low bias without internal gain. But for many applications, where very low levels of light are to be detected, photodetectors with high internal gain are desired in order to improve the sensitivity. The high internal gain can be obtained by avalanche photodiodes (APDs). APD is essentially a reverse-biased PIN photodiode that is operated at voltage close to the breakdown. Photogenerated carriers in the depletion region travel at their saturation velocities, and if they acquire enough energy from the

electric field during such transit, ionizing collisions with the lattice can occur. The field necessary to produce ionizing collisions is in the range of 10^4 to 10^5 V/cm. Secondary electron-hole pairs are produced in the process. All or some of the primary and secondary carriers may also gain enough energy and produce new carriers. This process is called impact ionization, which leads to carrier multiplication.

Figure 4.2 shows the schematic drawings of multiplication process for $\alpha \approx \beta$ and $\alpha >> \beta$. α and β are the impact ionization coefficients of electrons and holes, respectively. The impact ionization coefficients are the reciprocal of the average distance traveled by electrons and holes under the electric field before they impact with the lattice to produce secondary electron-hole pairs. α and β can also be defined as the average number of ionizing evens per unit length. In Fig. 4.2 (a), since $\alpha \approx \beta$, the number of secondary electron-hole pairs generated by electrons and holes are roughly equal. In Fig. 4.2 (b), since $\alpha >> \beta$, most of impact ionization processes are caused by electrons. α and β are fundamental material parameters but also depend on the electric field:

$$\alpha(E) = a_e \exp\left[-\left(\frac{b_e}{E}\right)^{m_e}\right] \tag{4.7}$$

$$\beta(E) = a_h \exp\left[-\left(\frac{b_h}{E}\right)^{m_h}\right] \tag{4.8}$$

where E is the local electric field, a_e, b_e, m_e and a_h, b_h, m_h are materials constants. The electric field required for impact ionization depends on the bandgap energy

[4.4]. Semiconductors with wide bandgaps require high electric fields to initiate the impact ionization process.

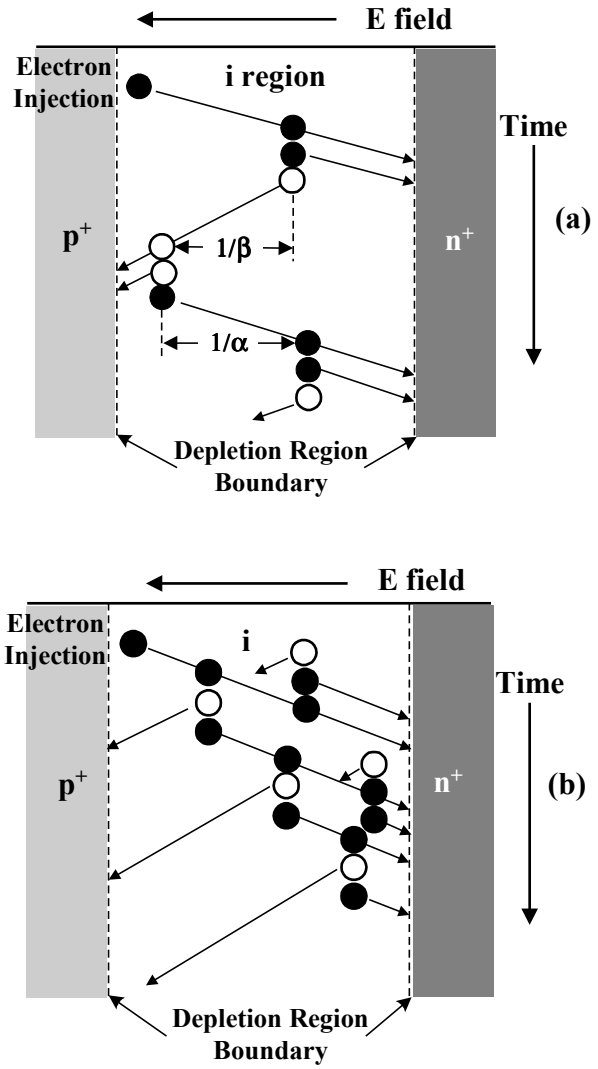

Figure 4.2: Avalanche multiplication process for (a) $\alpha \approx \beta$ and (b) $\alpha >> \beta$.

4.4.2 Noise of APDs

Besides shot noise and Johnson noise mentioned in Section 4.2.3, the avalanche process itself also causes noise in avalanche photodiode. During the avalanche multiplication process, there are random fluctuations in the actual distance between successive ionizing collisions. These fluctuations give rise to variations in the total number of secondary carriers generated by primary carriers injected into the multiplication region. This leads to noise in the total signal current and the magnitude of the noise depends on the mean avalanche gain.

The multiplication noise is lower if most of the impact ionization processes are initiated by a single type of carriers with higher impact ionization coefficient. For example, the multiplication noise in Fig. 4.2 (b) should be lower than that in Fig. 4.2 (a). This is because there is less fluctuation in the ionization process with only one type of participating carriers compared to the case when both electrons and holes are involved. As a result, a great deal of research has been devoted to the development of novel, low noise APD structures with $\beta/\alpha \approx 0$ (pure electron ionization) or $\alpha/\beta \approx 0$ (pure hole ionization). The multiplication noise is the highest if $\alpha \approx \beta$.

For avalanche photodiodes, the shot noise in Equation (4.3) can be modified to include the multiplication noise as follow [4.5]:

$$\left\langle i^2{}_{av} \right\rangle = 2q(I_{ph} + I_B + I_D)BM^2F \qquad (4.9)$$

I_{ph}, I_B and I_D are the photocurrent, background radiation and dark current, respectively. M is the multiplication gain and F is the excess noise factor. The total noise in avalanche photodiodes can be expressed as:

$$\left\langle i^2{}_{APD} \right\rangle = \left\langle i^2{}_{Johnson} \right\rangle + \left\langle i^2{}_{av} \right\rangle = 2q(I_{ph} + I_B + I_D)BM^2F + \frac{4kT}{R} \cdot B \quad (4.10)$$

We can see that the shot noise is amplified M^2F times in the avalanche photodiode. But since the desired optical signal is also amplified, the signal-to-noise ratio is given by:

$$\begin{aligned} \frac{S}{N} &= \frac{\frac{1}{2}\left(\frac{q\eta_{ext}P_{inc}}{h\nu}\right)^2 M^2}{2q(I_{ph} + I_B + I_D)F(M)M^2B + \frac{4kT}{R}B} \\ &= \frac{\frac{1}{2}\left(\frac{q\eta_{ext}P_{inc}}{h\nu}\right)^2}{2q(I_{ph} + I_B + I_D)F(M)B + \frac{4kT}{M^2R}B} \end{aligned} \quad (4.11)$$

The signal-to-noise ratio *S/N* of avalanche photodiode is improved at higher gain *M*. But since excess noise factor *F* also depends on the gain *M*, the gain cannot be very high. There is an optimum value of gain *M* at which the *S/N* is maximized.

Conventional models, which are often called the local-field theory, have been developed to explain the avalanche multiplication process in APDs [4.5, 4.6, 4.7]. This theory assumes that the impact ionization is a continuous, local process. The multiplication only depends on the local electric field and do not depend on the carrier history. Based on this assumption, McIntyre derived the relation between the excess noise factor *F* and multiplication gain *M* for pure electron injection as

$$F(M) = M - M(1-k)\left(\frac{M-1}{M}\right)^2 \quad (4.12)$$

where $k=\beta/\alpha$. For pure hole injection, the relation is:

$$F(M) = M - M\left(1 - \frac{1}{k}\right)\left(\frac{M-1}{M}\right)^2 \qquad (4.13)$$

The excess noise factor F is the figure of merit of noise in APDs. We can see that in order to have low excess noise in APDs, a low k (electron dominant ionization) is desired for pure electron injection and a high k (hole dominant ionization) is desired for pure hole injection. Even though the local-field theory is not valid for unconventional APD structures such as APDs with very thin multiplication regions [4.8-4.14], the Equation (4.12) and (4.13) can still be used to fit the experimental data in order to compare with previously published results.

4.4.3 Gain-Bandwidth-Product

Besides the bandwidth-limiting mechanisms discussed in Section 4.2.4, the avalanche multiplication process also affects the bandwidth of avalanche photodiode. Since the avalanche process takes time to buildup, the bandwidth is reduced with the increase of multiplication gain. For a properly designed APD, the bandwidth-limiting factor is carrier transit time at low gains and avalanche buildup time at high gains. The highest bandwidth of an APD is obtained at unity gain where the transit time is the limiting factor and the APD operates as a PIN photodiode. Due to the tradeoff between gain and bandwidth, gain-bandwidth-product is commonly used as the figure of merit for APDs. The gain-bandwidth-product is constant at high gain.

The avalanche buildup time depends on the width of the multiplication region and the ratio of the electron and hole ionization coefficients. If $\beta/\alpha \approx 1$, both electrons and holes continuously recycle and persist in the multiplication

region which leads to a long response time and low bandwidth. Therefore, electron-dominant ($\beta/\alpha \approx 0$) or hole-dominant ($\beta/\alpha \rightarrow \infty$) ionization process is desired for high-bandwidth APD. Thin multiplication region in APD can also improve the gain-bandwidth-product due to the fact that a narrower multiplication width reduces the effect of carrier feedback for a given gain.

4.5 RESONANT-CAVITY-ENHANCED AVALANCHE PHOTODETECTORS

4.5.1 Resonant-Cavity Structure

Avalanche photodiodes with high speed and high quantum efficiency are very important in high-bit-rate, long-haul fiber optic communication systems. However, there is tradeoff between the bandwidth and sensitivity. High quantum efficiency requires a thick absorption region in APD but this also increases the carrier transit time through the depletion region and thus slows down the frequency response.

The difficulty can be solved by placing the photodiode structure into a Fabry-Perot resonant cavity [4.15, 4.16. 4.17]. Figure 4.3 shows the schematic drawing of a resonant cavity with top mirror R_1 and bottom mirror R_2. The cavity thickness is a multiple of one-half of the desired wavelength to be detected. The light enters the cavity from the top and forms an optical standing wave inside the cavity. The absorption region is placed at the antinode of the optical standing wave to enhance the absorption because the optical field is the strongest at this point. The light is reflected by the top and bottom mirrors inside the cavity and makes multiple passes through the absorption region, which increases the effective absorption length and results in higher quantum efficiency. By

decoupling the optical and electrical paths, the resonant cavity structure can achieve high external quantum efficiency with very thin absorption layer, thus circumventing the tradeoff between quantum efficiency and carrier transit time.

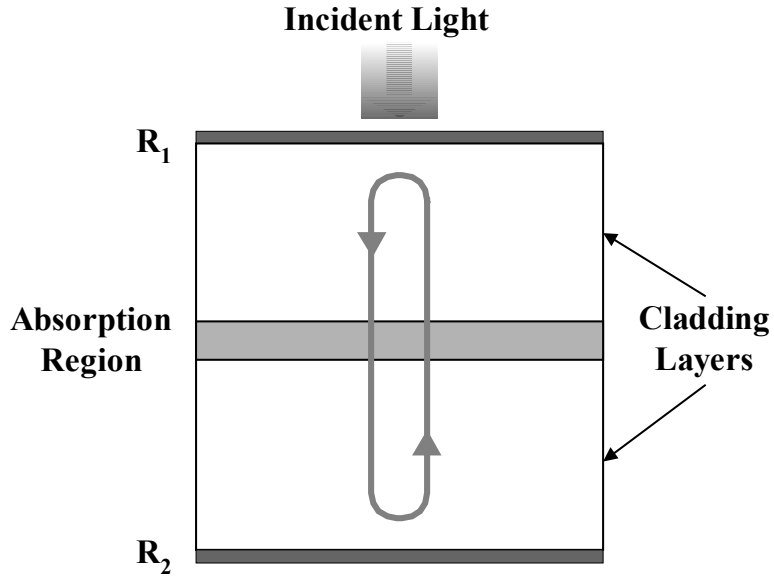

Figure 4.3: Schematic drawing of a resonant-cavity structure.

4.5.2 Distributed Bragg Reflector Mirror

High quantum efficiency can be achieved by high-Q resonant cavity with high mirror reflectivities and low loss. Semiconductor or dielectric distributed Bragg reflectors (DBRs) can be used as the bottom and top mirrors. A DBR mirror consists of alternating layers of low and high refractive index materials. The optical thickness of each layer is often chosen to be a quarter of the wavelength of the light in that medium. The multiple layers are called quarter wave stack (QWS). The reflectivity of quarter wave stack can be calculated by

using transfer matrix approach of Maxwell's equations [4.18]. Assuming normally incident light, for a DBR mirror made of alternating N pairs of quarter-wavelength layers with refractive index n_L and n_H, the reflectivity R at the resonant wavelength is given by:

$$R = \left[\frac{\frac{n_0}{n_s} - \left(\frac{n_L}{n_H} \right)^{2N}}{\frac{n_0}{n_s} + \left(\frac{n_L}{n_H} \right)^{2N}} \right]^2 \tag{4.14}$$

where n_0 and n_s are the refractive indices of air and substrate, respectively. The reflectivity R is determined by the number of mirror pairs as well as the contrast of refractive indices. R increases as the number of mirror pairs increases. For a given N, R is higher if n_L/n_H is smaller. For example, at 1.3 μm, a DBR mirror with 20 pairs of GaAs (n_{GaAs}=3.41) and AlAs (n_{AlAs}=2.91) has a reflectivity of 0.998. For the same reflectivity, only 5 pairs of ZnSe (n_{ZnSe}=2.47) and MgF_2 (n_{MgF2}=1.37) quarter-wave layers are required.

Semiconductor mirrors such as GaAs/AlAs DBRs are commonly used as the bottom mirrors of resonant-cavity-enhanced (RCE) APDs because they can be grown in the MBE chamber with the APD structures. The top mirrors can either utilize the semiconductor mirrors grown by MBE or dielectric mirrors such as MgF_2/ZnSe DBRs deposited by e-beam sputtering outside the MBE growth chamber. The positions of nodes and antinodes of the optical standing wave are determined by the stacking order of high and low refractive index materials in the cavity.

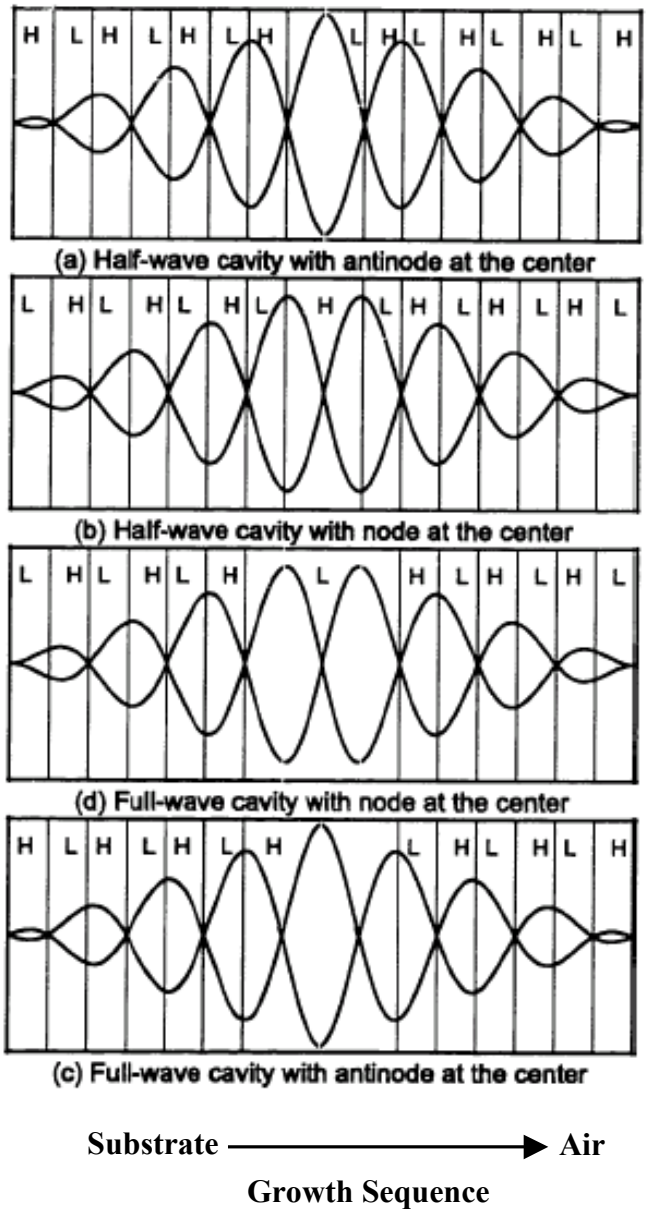

Figure 4.4: Microcavity configurations with different stacking orders [4.19].

Figure 4.4 shows the schematic drawing of microcavities with four different configurations [4.19]. The “H” and “L” refer to the layers with high and

low refractive indices, respectively. For example, to design a full-wave (λ, 2λ, 3λ, …) RCE GaAs (H) homojunction APD with GaAs (H)/AlAs (L) top and bottom DBR mirrors and with antinode at the center of the cavity, the stacking order of the bottom DBR mirror is GaAs (H)-AlAs (L)-GaAs (H)-AlAs (L)… from the substrate and the stacking order of the top DBR mirror is AlAs (L)-GaAs (H)-AlAs (L)-GaAs(H)…from the GaAs (H) cavity layers (Fig. 4.4 (c)). The absorption layers of the APD structure should be placed at the antinodes of the optical standing wave inside the cavity in order to maximize the quantum efficiency.

4.5.3 External Quantum Efficiency of RCE APD

The external quantum efficiency of a RCE APD can be derived based on the following assumptions: (1) normally incident light; (2) absorption only in the absorption layers; (3) uniform refractive indices of the cavity spacer layers; (4) no light penetration into the mirror.

Figure 4.5 shows the electric field inside a resonant cavity. The downward electric field E_{down} near the top mirror inside the cavity is:

$$\begin{aligned} E_{down} &= (1) + (5) + \ldots \\ &= E_{inc}t_t + E_{inc}t_t \cdot e^{-j(2\beta L)} \cdot e^{-\alpha d} \cdot r_t e^{-j\Psi_t} \cdot r_b e^{-j\Psi_b} + \ldots \\ &= \frac{E_{inc}t_t}{1 - e^{-j(2\beta L)} \cdot e^{-\alpha d} \cdot r_t e^{-j\Psi_t} \cdot r_b e^{-j\Psi_b}} \end{aligned} \qquad (4.15)$$

where E_{inc} is the incident electric field, t_t is electric field transmission coefficient through the top mirror, L is the effective cavity length L_1+L_2, β is the propagation coefficient, α is the absorption coefficient of the absorption layer, d is the

absorption layer thickness, r_t and r_b refer to the electric field reflection coefficients of the top and bottom mirrors, and Ψ_t and Ψ_b are the phase shifts at the top and bottom mirrors.

The upward electric field E_{up} near the bottom mirror is:

$$
\begin{aligned}
E_{up} &= (3) + (7) + \ldots \\
&= E_{inc} t_t \cdot e^{-j\beta L} \cdot e^{-\frac{\alpha}{2}d} \cdot r_b e^{-j\Psi_b} + E_{inc} t_t \cdot e^{-j(3\beta L)} \cdot e^{-\frac{3}{2}\alpha d} \cdot r_b^{\,2} e^{-j(2\Psi_b)} \cdot r_t e^{-j\Psi_t} + \ldots \\
&= \frac{E_{inc} t_t \cdot e^{-j\beta L} \cdot e^{-\frac{\alpha}{2}d} \cdot r_b e^{-j\Psi_b}}{1 - e^{-j(2\beta L)} \cdot e^{-\alpha d} \cdot r_b e^{-j\Psi_b} \cdot r_t e^{-j\Psi_t}}
\end{aligned}
\qquad (4.16)
$$

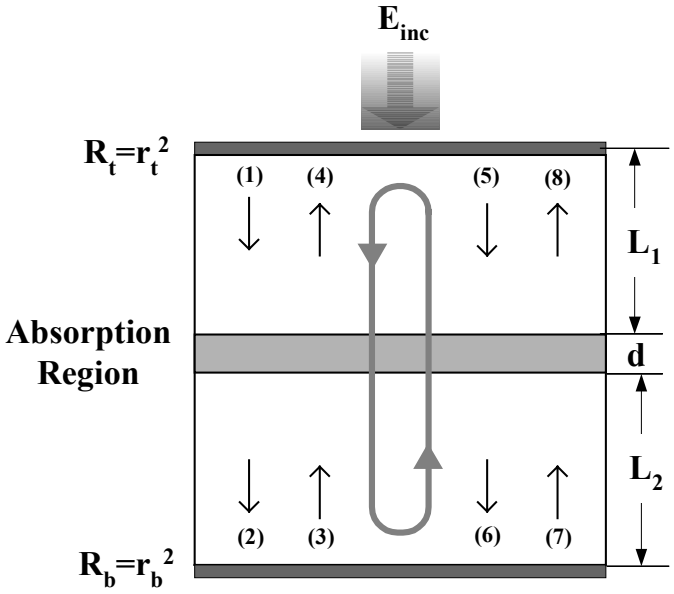

Figure 4.5: Schematic drawing of the electric field inside a resonant cavity.

The power of the electric field E is given by:

$$P = \frac{n}{2\eta_0}|E|^2 \tag{4.17}$$

where n is the refractive index and η_0 is the impedance of the free space. Therefore the external quantum efficiency of the RCE APD is:

$$\begin{aligned}\eta_{ext} &= \frac{P_{up} + P_{down}}{P_{inc}} = \frac{|E_{up}|^2 + |E_{down}|^2}{|E_{inc}|^2} \\ &= \frac{(1-R_t)(1+R_b e^{-\alpha d})(1-e^{-\alpha d})}{1-2\sqrt{R_t R_b}\, e^{-\alpha d}\cos(2\beta L + \Psi_t + \Psi_b) + R_t R_b e^{-2\alpha d}}\end{aligned} \tag{4.18}$$

where P_{inc} is the incident optical power, P_{up} and P_{down} are the optical powers of upward and downward fields in the cavity, and R_t and R_b are the reflectivities of the top and bottom mirrors, respectively. Here $R_t = r_t^2$ and $R_b = r_b^2$. If $\cos(2\beta L + \Psi_1 + \Psi_2) = 1$, the external quantum efficiency goes to maximum. This is where the resonant happens. The peak external quantum efficiency can be expressed as:

$$\eta_{peak} = \frac{(1-R_t)(1+R_b e^{-\alpha d})(1-e^{-\alpha d})}{(1-\sqrt{R_t R_b}\, e^{-\alpha d})^2} \tag{4.19}$$

The external quantum efficiency of resonant-cavity-enhanced APD is determined by the absorption coefficient and absorption layer thickness as well as the top and bottom DBR mirror reflectivities. Figure 4.6 shows the peak external quantum efficiency as a function of absorption αd for a resonant-cavity-enhanced APD calculated from Equation (4.19). The reflectivity of bottom DBR mirror is 0.998 except for the no-cavity case. We can see that for the same αd, in other words, for the same absorption material and absorption layer thickness, the external quantum efficiency depends on the different top mirror reflectivities. If we know the external quantum efficiency, the reflectivities of top and bottom

DBR mirrors, and the absorption layer thickness, the absorption coefficient α can be determined from these plots.

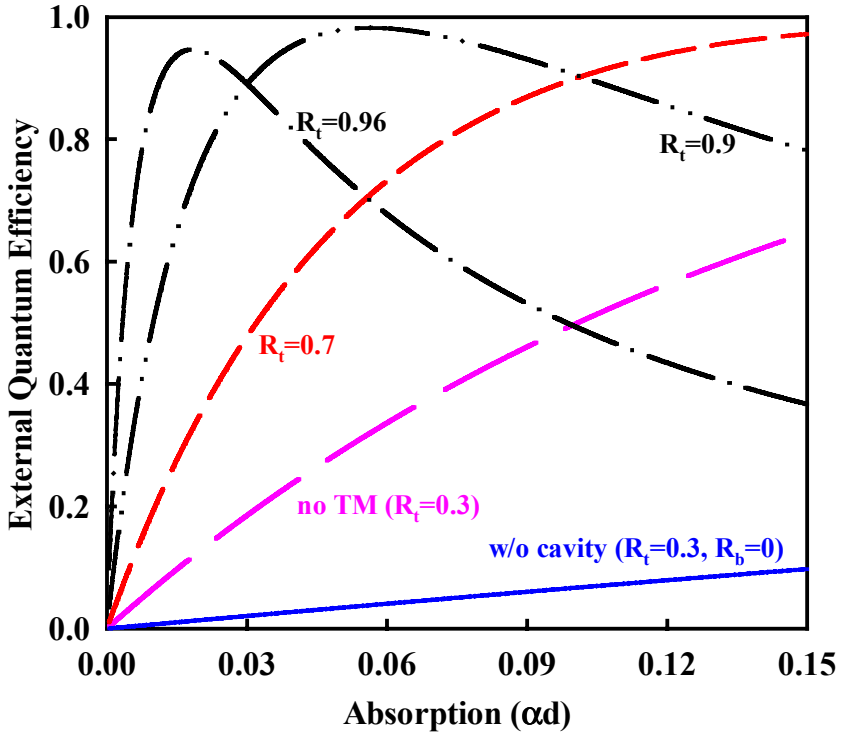

Figure 4.6: Simulated external quantum efficiency as a function of absorption αd for different top mirror reflectivities. The reflectivity of bottom DBR mirror is 0.998.

4.6 APDs With Separate Absorption, Charge and Multiplication Regions

The conventional APD is essentially a PIN photodiode operating at high reverse bias with internal gain. Most of the electric field drops across the undoped *i* region. The high field across the *i* region helps to drive the photogenerated

carriers across the depletion region and thus reduces the carrier transit time. The avalanche photodiode is usually a heterojunction diode with wide-bandgap P^+ or N^+ window layers and narrow-bandgap undoped absorption layer to make sure that the absorption happens in the absorption region and the carrier diffusion from outside the depletion region is eliminated. However, for direct bandgap semiconductors, the tunneling current can be expressed as [4.20]:

$$I_{tunnel} \cong \gamma A \exp\left[-\frac{\Theta m_0^{\frac{1}{2}} E_g^{\frac{3}{2}}}{q\hbar E_m}\right] \qquad (4.20)$$

where m_0 is the free electron mass, q is the electron charge, $\hbar$ is the reduced planck's constant, E_m is the peak electric field, E_g is the bandgap of semiconductor, Θ is a parameter depending on the effective mass of electron and the detailed shape of the tunneling barrier, A is a constant and γ depends on the initial and final states of the tunneling carrier. We can see that high electric field in narrow bandgap semiconductor results in high tunneling current, which is the primary component of dark current at high bias.

In order to avoid the excessive dark current at high bias, it is necessary to separate the multiplication and absorption regions and to tailor the profile of the electric field. This leads to a modified APD structure with separate absorption, charge and multiplication regions which is called SACM APD [4.21, 4.22, 4.23]. Figure 4.7 shows the schematic cross section and electric field profile of a SACM APD. In this structure, most of the electric field drops across the undoped wide-bandgap multiplication region. The thin lightly p-type doped charge layer ensures a low field in the absorption region. Therefore the tunneling in the narrow-

bandgap absorption region is significantly reduced. To eliminate the carrier trapping at the heterointerfaces and improve the bandwidth, grading layers at the interfaces can be used. This kind of structure is called separate absorption, grading, charge and multiplication (SAGCM) APD.

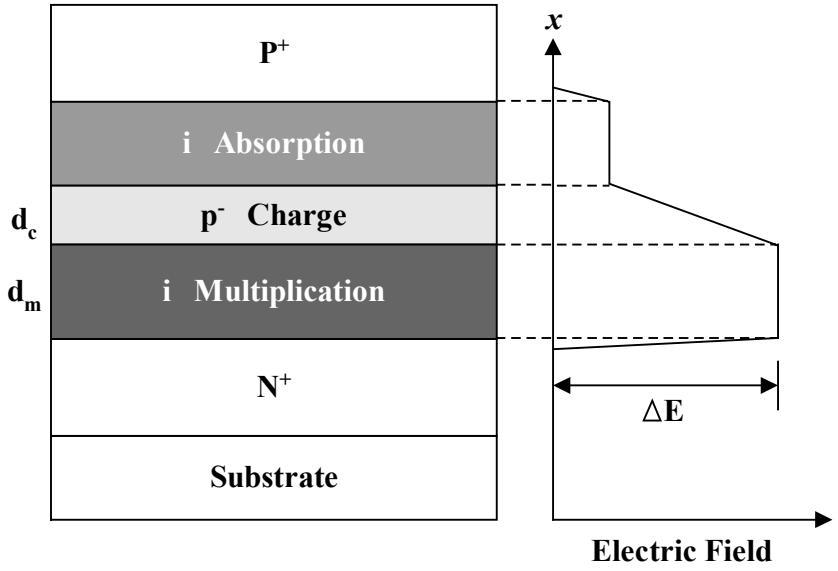

Figure 4.7: Schematic cross-section and electric profile of SACM APD.

The punchthrough voltage of SACM APD is the reverse bias at which the charge layer is fully depleted. It can be calculated from the area between the electric profile and the *x*-axis. Since the electric field across the absorption region is zero at punchthrough, the punchthrough voltage $V_{punchthrough}$ can be shown as:

$$V_{punchthrough} = \frac{1}{2}\Delta E \cdot d_c + \Delta E \cdot d_m \qquad (4.21)$$

where ΔE is the electric field dropped across the multiplication region at punchthough, d_c is the charge layer thickness and d_m is the multiplication layer thickness. From Poisson's equation [4.24], the gradient of electric field in the charge layer is:

$$\frac{d\varepsilon(x)}{dx} = \frac{q}{\varepsilon_0 \varepsilon_r}(-N_a^-)$$
$$\Rightarrow \Delta E = \frac{q}{\varepsilon_0 \varepsilon_r} \cdot N_a^- \cdot d_c \qquad (4.22)$$

where N_a^- is the charge layer doping, q is the electron charge, ε_0 is permittivity of free space and ε_r is the relative dielectric constant of semiconductor.

The punchthrough voltage needs to be carefully tuned. If the punchthrough voltage is too high, the electric field across the absorption region is too low at the revise bias near breakdown. This leads to long carrier transit time and slow frequency response. If the punchthrough voltage is too low, the electric field across the absorption region is too high at the reverse bias near breakdown, which leads to high tunneling current and high dark current in the APD.

The combining of resonant cavity and SACM APD structure could result in APD with high quantum efficiency, high speed, low noise and low dark current.

Chapter 5: Resonant-Cavity-Enhanced GaAsSb *p-i-n* Photodiodes

5.1 INTRODUCTION

In Chapter 3 we discussed the MBE growth of compressively-strained GaAsSb layers on GaAs substrates. After optimizing the growth parameters such as growth temperatures, group-III (Ga) and group-V (As and Sb) fluxes, we successfully achieved GaAsSb single and multiple quantum wells with emission wavelengths around 1.3 μm on GaAs substrates. Photoluminescence (PL) and X-ray diffraction (XRD) results show that the GaAsSb layers have very good optical properties. As discussed in Chapter 1 and Chapter 4, photodiodes operating at 1.3μm on GaAs substrates are very attractive for the applications in long-haul, high-bit-rate fiber optic communication systems. This chapter discusses the design, fabrication and device performance of resonant-cavity-enhanced (RCE) GaAsSb *p-i-n* photodiodes on GaAs substrates operating at 1.3 μm. The "*p-i-n*" refers to photodiode structure instead of the operation mode.

5.2 PHOTODIODE STRUCTURE

The schematic diagram of this photodiode structure including nominal thickness values is shown in Figure 5.1. Since GaAsSb is not lattice-matched to GaAs, the thickness of the coherently strained layers is limited. In order to obtain higher quantum efficiency from the very thin absorption layers, a 2λ resonant cavity with a GaAs/AlAs bottom distributed Bragg reflector (DBR) mirror and a MgF_2/ZnSe dielectric top DBR mirror was utilized. The material was grown on a

(100)-oriented n^+ GaAs substrate in a Varian Gen II solid source MBE system. Beryllium (Be) and silicon (Si) were used as the *p*-type and *n*-type dopants, respectively.

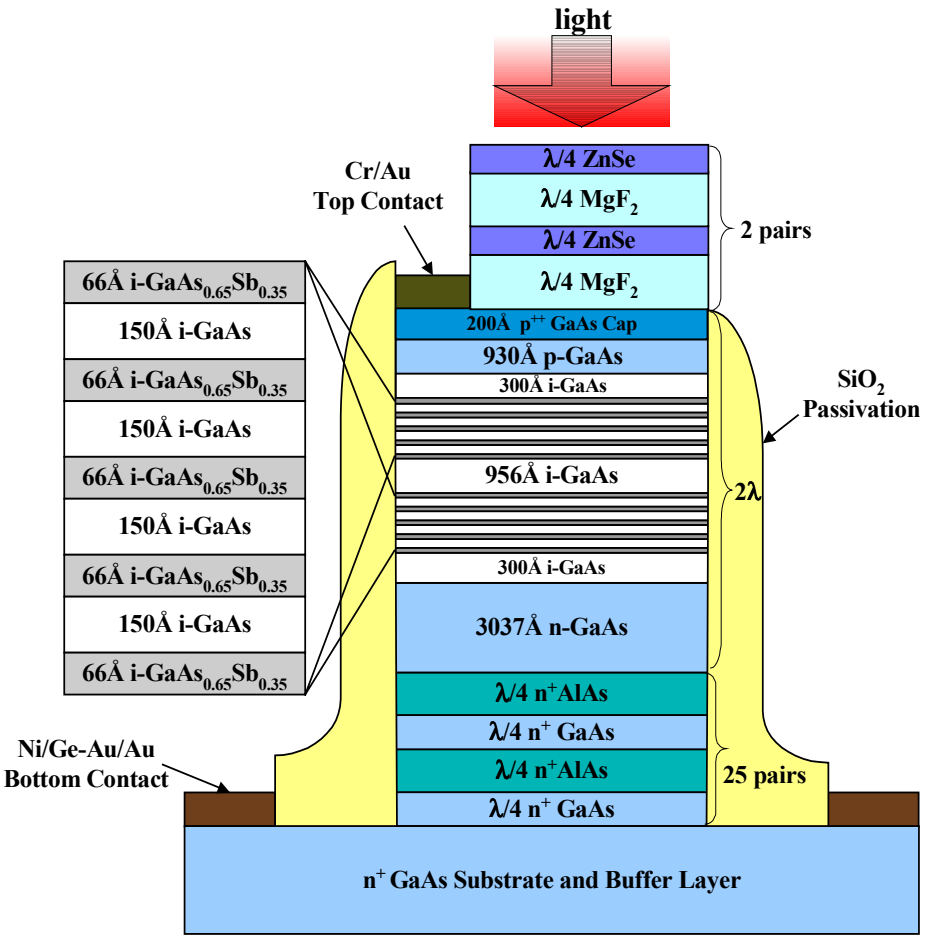

Figure 5.1: Schematic diagram of RCE GaAsSb *p-i-n* photodiode structure.

From the bottom to the top, the layer structure was: a n^+ GaAs buffer layer, a bottom DBR mirror containing 25 pairs of λ/4 GaAs/AlAs layers with *n*-type doping (Si: $5\times10^{18}/cm^3$), a 3037Å-thick *n*-type (Si: $5\times10^{18}/cm^3$) GaAs spacer

layer, an undoped region containing two GaAsSb/GaAs multiple quantum well (MQW) absorption regions and three GaAs spacer layers, a 930Å-thick *p*-type (Be: $5\times10^{18}/cm^3$) GaAs spacer layer, a p^{++} (Be: $2\times10^{19}/cm^3$) GaAs cap layer for ohmic contact formation and 2 pairs of λ/4 MgF_2/ZnSe layers as the dielectric top mirror. The absorption region consisted of four 150Å-thick undoped GaAs layers sandwiched between five 66Å-thick undoped GaAsSb layers. Two such absorption regions were placed at the antinodes of the optical standing wave inside the cavity to further increase the quantum efficiency. Therefore, the total absorption layer thickness was 66nm. The intrinsic region was unintentionally doped with an *n*-type background concentration of approximately $2\times10^{15}/cm^3$. The two 300Å-thick undoped GaAs spacer layers prevented dopant diffusion into the intrinsic region of the device.

Figure 5.2 shows the simulated optical field inside the cavity of the RCE GaAsSb *p-i-n* photodiode. The cavity was composed of GaAs and GaAsSb layers with refractive indices of 3.41 and 3.62, respectively. The relationship between the resonant wavelength and the thickness of each layer is:

$$n_1 \cdot d_1 + n_2 \cdot d_2 + ... + n_L \cdot d_L = 2\lambda \qquad (5.1)$$

where n_1, n_2, …, n_L are the refractive indices at the resonant wavelength of different layers, d_1,d_2, …, d_L are the thickness of the different layers, and λ is the resonant wavelength. By adjusting the thickness of different GaAs spacer layers, we can obtain the resonance at the wavelength of 1.3 μm and place the two GaAsSb absorption regions at the antinodes of the optical standing wave inside the cavity as shown in Fig. 5.2.

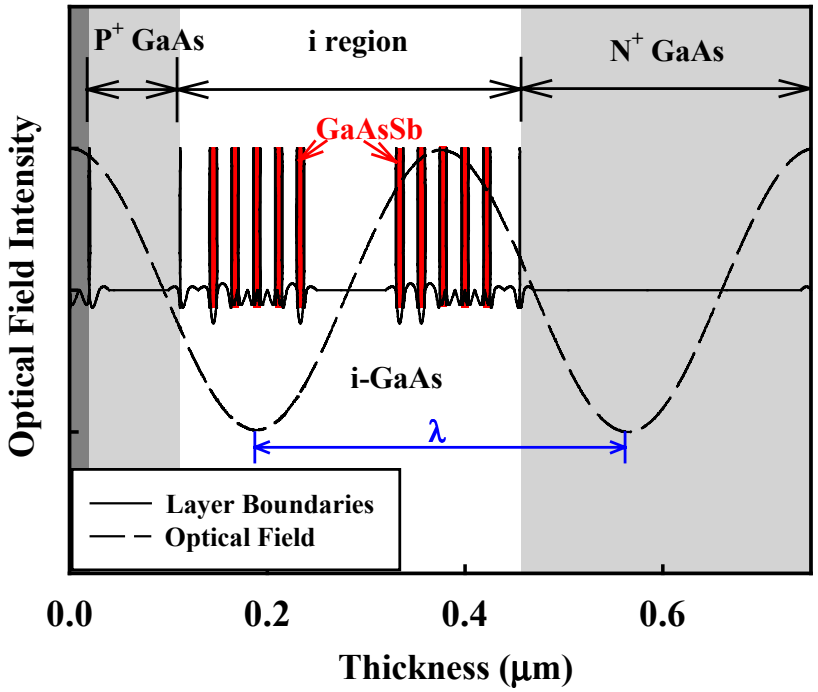

Figure 5.2: Simulated optical field inside the cavity of RCE GaAsSb *p-i-n* photodiode with 2λ cavity length.

For the MBE systems in the University of Texas at Austin, since the pyrolytic boron nitride (PBN) shutters reflect the heat back to the effusion cells, the cells are a little hotter when the shutters are just opened than after a long period of growth. The calibration usually takes about 15-30 seconds but the growth of thick layers takes minutes to hours. Therefore, the calibrated growth rates are approximately 4.5% higher than the actual growth rates. This is a systematic shift which is almost constant. This growth rate shift is very important for mirror and resonant cavity growth and was used to adjust the growth rates used for these devices.

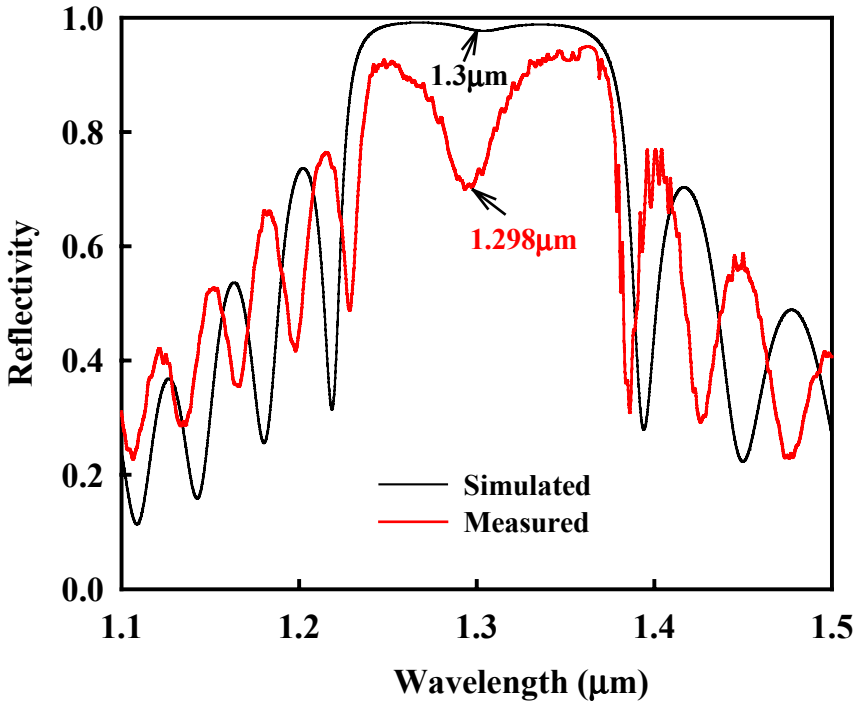

Figure 5.3: Simulated and measured reflectivities of the RCE photodiode with GaAsSb absorption layers.

Figure 5.3 shows the simulated and measured reflectivities of the RCE photodiode structure. The mirror and layers were grown 4.5% thicker than the thickness used in the simulation to compensate the growth rate shift. The reflectivity of the structure was measured by a Perkin Elmer spectrometer after growth but before device fabrication and deposition of dielectric top mirror. The reflectivity plateaus were the GaAs/AlAs mirror reflectivities and the dips around 1.3 μm were due to the absorption in GaAsSb layers. The absorption dip of the

RCE GaAsSb photodiode was at 1.298 μm which was very close to the designed resonant wavelength of 1.3 μm.

5.3 MATERIAL GROWTH

The GaAs layers were grown at the deoxidation temperature of 580˚C and the GaAsSb layers were grown at 530˚C with Ga growth rate of ~0.6 ml/s. The Veeco-Applied Epi valved arsenic and antimony cracker sources were used for As and Sb, producing mainly As_2 and Sb_1 species, respectively. For the GaAs growth, the arsenic beam equivalent pressure (BEP) was approximately 5.3×10^{-6} Torr. The GaAsSb layers were grown under a mixed group-V flux with As BEP of 2.5×10^{-6} Torr and Sb BEP of 5.0×10^{-7} Torr. Measured and simulated X-ray diffraction spectra showed that the Sb mole fraction was approximately 0.35 in these GaAsSb layers. To make sure that after the growth of ten highly strained GaAsSb layers the material quality is still good, photoluminescence samples with 7nm-GaAsSb/15nm-GaAs single quantum well (QW), three QWs and ten QWs were grown under the same growth condition. The sample with ten QWs had a structure similar to the *p-i-n* photodiode with two 5QW-regions separated by a thick GaAs spacer. Figure 5.4 shows the 300K photoluminescence comparison of these samples. We can see that by adding more GaAsSb QWs, both the PL intensity and the PL linewidth increase. The broadening in PL linewidth may due to the composition variation in the ten GaAsSb layers. The X-ray diffraction measurement of the 10QW sample showed no relax in the GaAsSb layers.

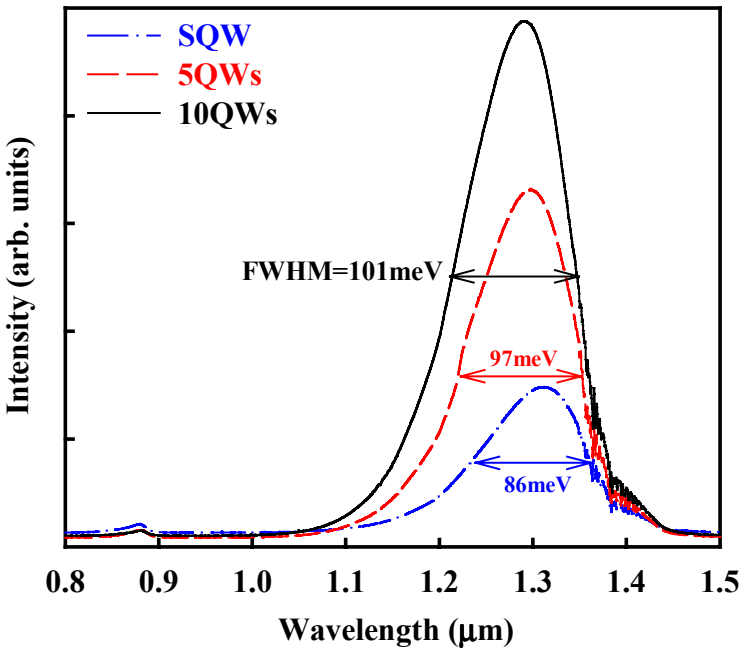

Figure 5.4: 300K photoluminescence comparison of samples with 7nm-GaAsSb/15nm-GaAs single QW, 3QWs and 10QWs. For GaAsSb layers, the growth temperature was 530°C, Ga growth rate was ~0.60ml/s, As BEP was 2.5×10^{-6} Torr and Sb BEP was 6.0×10^{-7} Torr.

5.4 DEVICE FABRICATION

Photodiodes with 150 μm diameters were fabricated after the material growth. The basic process flow is as follow:

Step 1: Wafer Cleaning

During the MBE growth, molten Indium was used to bond the wafer on the molybdenum sample block. The Indium on the backside of the wafer should be removed prior to the fabrication processes because the non-uniform Indium layer may cause the wafer to break into small pieces during the subsequent

photolithography processes on the contact aligner. The wafer was placed on a heated glass slide with a temperature of 200°C ~300°C. By pushing the wafer back and forth on the hot glass slide, the molten Indium on the backside of the wafer attached onto the heated glass slide and left a uniform Indium film on the wafer. After Indium removal, the wafer was rinsed by acetone, isopropyl alcohol or methanol and de-ionized (DI) water in turn and then dried in nitrogen flow.

Step 2: Mesa Etch

Device mesas with ~150 μm diameters were defined by wet chemical etching using a 1:1:8 etch solution of phosphoric acid (H_3PO_4), hydrogen peroxide (H_2O_2) and water (H_2O). This solution is capable of etching AlGaAs, GaAs, GaAsSb, InGaAs and InAlAs. Since there was no etch-stop layer in the structure, an Alpha step profiler was used during the mesa etch to measure the etch depth. Photoresist was used as the etch mask and post-bake at 120°C for at least 30 minutes was required after photolithography process in order to limit the undercut during the etch. The photoresist was removed by rinsing the wafer in acetone, isopropyl alcohol or methanol and DI water after etch.

Figure 5.5 (a) shows the schematic cross section of the device after mesa definition.

Step 3: Passivation

A silicon dioxide (SiO_2) passivation layer was deposited by plasma enhanced chemical vapor deposition (PECVD) on the sample right after the mesa etch in order to reduce the edge leakage current and prevent the oxidation of $Al_xGa_{1-x}As$ and $GaAs_{1-x}Sb_x$ layers. A 1000Å-thick SiO_2 layer was deposited using

silane (SiH_4) and nitrous oxide (N_2O) as the precursors at 285 °C in the Plasma-therm 790 Series PECVD chamber.

The schematic cross section of the device after passivation is shown in Fig. 5.5 (b).

Step 4: P-contact Formation

The P-contact (top contact) was patterned by a photo mask with holes on it. After the photoresist development and post-bake at 120°C, top contact windows were opened on the SiO_2 passivation layer by buffered oxide etch (BOE). Then the sample was transferred into the chamber of CHA Industries E-beam evaporator and P contact with 250Å-thick Cr and 800 Å-thick Au layers was deposited. The Cr and Au provide good ohmic contact on heavily p-type doped GaAs cap layer. After the E-beam evaporation, the metal on the photoresist was "lift-off" in acetone with an ultrasonic bath. The wafer was then cleaned by solvents and DI water.

Figure 5.5 (c) shows the schematic cross section of the device after the P-contact formation.

Step 5: N-contact Formation

Similar to the P-contact, the N-contact (bottom contact) was also E-beam evaporated. A photo mask with dots on it was used instead of a hole mask. The bottom contact was made of Ni (100Å), Ge-Au (200Å) and Au (800Å). The same "lift-off" and wafer cleaning processes were performed after the N-contact formation.

Figure 5.5(d) shows the schematic cross section of the device after N-contact formation.

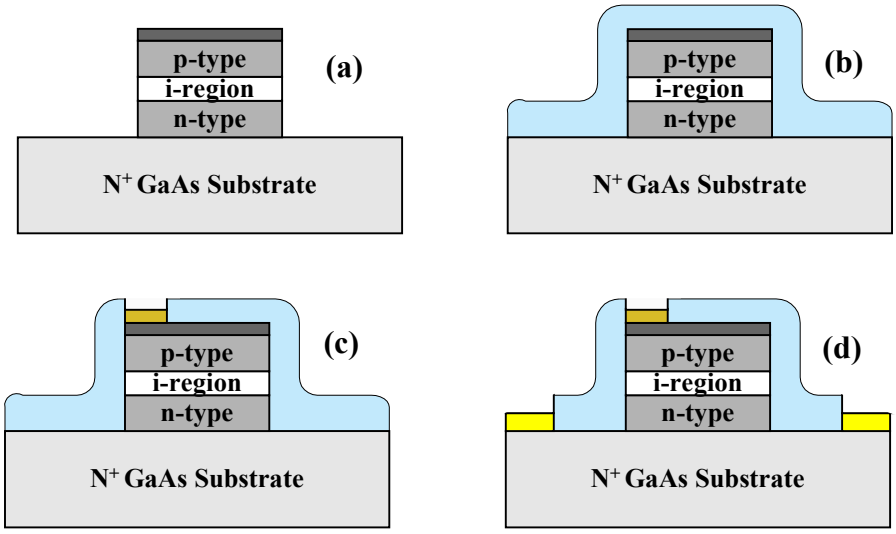

Figure 5.5: Schematic cross section of the device after (a) mesa etch; (b) SiO_2 passivation; (c) top contact deposition; (d) bottom contact deposition.

Step 6: Dielectric Mirror Deposition

Quarter wave stack (QWS) MgF_2 and ZnSe dielectric top mirror was deposited by E-beam evaporation in a Leybold A. G. system. Before deposition, the SiO_2 layer on top of the mesa was removed by BOE. The thickness of the MgF_2 and ZnSe layers is determined by the resonant wavelength of the cavity and the refractive indices of the two materials. Figure 5.3 shows that the resonant wavelength of the grown structure was 1.3 μm. At 1.3 μm the refractive indices of MgF_2 and ZnSe are 1.37 and 2.47, respectively. Therefore, the thickness of the $\lambda/4$ MgF_2 and ZnSe layers should be 2372Å and 1316Å, respectively. The crystal

in the Leybold chamber measures the thickness of the deposited layers but there is a systematic shift in the measured result. Therefore, test mirrors should be grown on waste GaAs wafers or glass slides prior to the deposition on the final devices. The deposited dielectric mirror covered the mesa as well as the top and bottom contacts. During the device measurements, the mirrors on top of the contacts were scratched away by the probe. The final schematic cross section of the photodiode is shown in Fig. 5.1.

5.5 DEVICE MEASUREMENTS

5.5.1 I-V Curve

The DC current-voltage characteristics (I-V curves) were measured using a low-noise probe station and a HP 4145B semiconductor parameter analyzer under white light illumination. Since the dark current is negligible at low bias as compared to the photocurrent, the avalanche multiplication gain can be determined as

$$M(V) = \frac{I_{ph} - I_{dark}}{I_{unity}} \tag{5.2}$$

where M is the calculated multiplication gain, I_{ph} is the photocurrent, I_{dark} is the dark current and I_{unity} is the photocurrent at unity gain. At low bias the photocurrent does not increase with the reverse bias voltage which means there is no internal gain in the photodiode. This constant photocurrent is chosen to be I_{unity}.

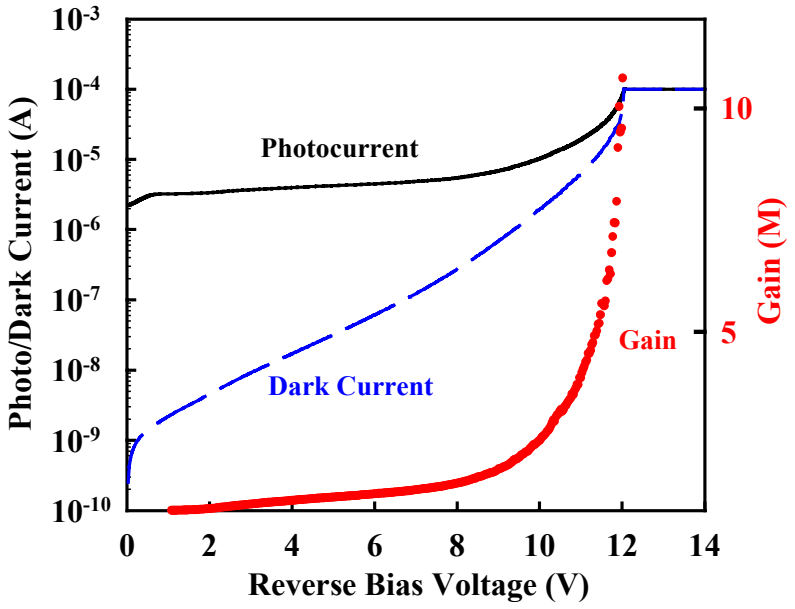

Figure 5.6: Photocurrent, dark current and avalanche multiplication gain as a function of reverse bias voltage for the RCE GaAsSb *p-i-n* photodiode.

Figure 5.6 shows the photocurrent, dark current and avalanche gain as a function of reverse bias voltage of the RCE GaAsSb *p-i-n* photodiode. The breakdown occurred at ~12V and a DC gain up to 10 was obtained near breakdown. At 90% of the breakdown, the dark current was approximately 5 μA. The dip on the photocurrent curve at very low bias (<1 volt) was due to the carrier trapping at the GaAsSb/GaAs heterojunction interfaces. This device exhibited higher than desired dark current at high bias. In this device, most of the electric field dropped across the undoped GaAs and GaAsSb layers. The narrow bandgap GaAsSb layers acted as both the absorption region and part of the multiplication region. The multiplication and band-to-band tunneling in these GaAsSb layers

were the primary components of the dark current at higher bias levels [5.1, 5.2]. The avalanche photodiode structure with separate absorption, charge and multiplication region (SACM) discussed in Chapter 4 can decrease the electric field in the absorption region and reduce the tunneling component of the dark current at high bias.

5.5.2 External Quantum Efficiency

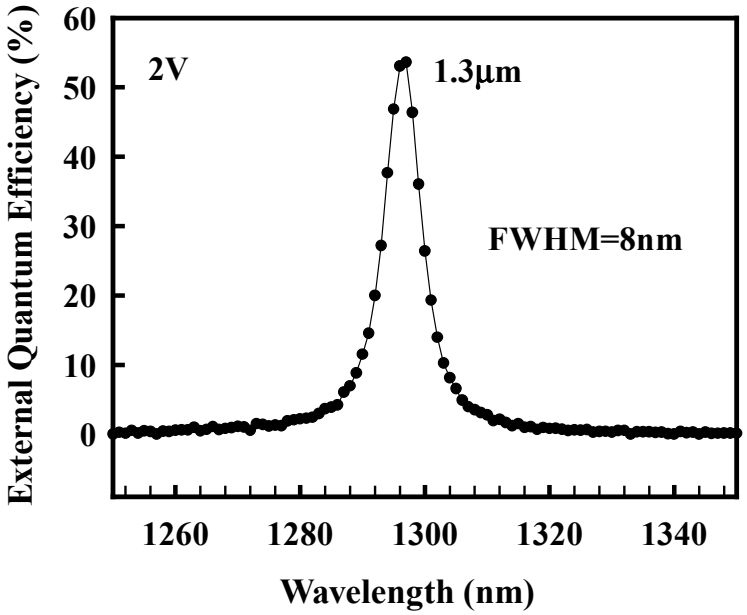

Figure 5.7: External quantum efficiency of the GaAsSb RCE *p-i-n* photodiode with 2 pairs of MgF_2/ZnSe layers as the top mirror.

The external quantum efficiency was measured at unity gain using a tunable monochromatic tungsten-halogen light source, a spectrometer and a lock-in amplifier. As shown in Fig. 4.6, the external quantum efficiency of RCE

photodiode is determined by the absorption coefficient, the absorption layer thickness, the bottom and top mirror reflectivities. Top mirrors with 1 pair, 2 pairs and 3 pairs of λ/4 MgF_2/ZnSe layers were deposited on different devices and the quantum efficiencies of different devices were measured to find out the optimum top mirror reflectivity. Figure 5.7 shows the external quantum efficiency of the photodiode with 2 pairs of λ/4 MgF_2/ZnSe layers as the dielectric top mirror. The peak external quantum efficiency was 54% at the wavelength of 1.3 μm and the full width at half maximum (FWHM) was 8 nm. Adding a third pair of λ/4 MgF_2/ZnSe layers reduced the peak external quantum efficiency to 31%.

The absorption coefficient (α) of $GaAs_{0.65}Sb_{0.35}$ can be estimated from the following equation:

$$\eta_{peak} = \frac{(1+R_b e^{-\alpha d})(1-R_t)(1-e^{-\alpha d})}{(1-\sqrt{R_t R_b}\, e^{-\alpha d})^2} \qquad (5.3)$$

where η_{peak} is the peak external quantum efficiency, R_b is the reflectivity of the bottom DBR mirror, R_t is reflectivity of dielectric top mirror, d is the total thickness of the absorption layers and α is the absorption coefficient of the absorber. Based on a reference DBR sample, the bottom mirror reflectivity was estimated to be 93% at 1.3 μm. For the top dielectric mirror, two and three pairs of λ/4 MgF_2/ZnSe layers have reflectivities of 90% and 97%, respectively. The external quantum efficiency as a function of the normalized absorption (αd) can be calculated from Equation 5.3 (plots shown in Fig. 5.8). The measured external quantum efficiencies are also shown in Fig. 5.8. The simulated and measured results match quite well. From Fig. 5.8, we can see the normalized absorption αd was approximately 0.048. Since the total thickness of the GaAsSb absorption

layers was 66nm, we estimated that the absorption coefficient of $GaAs_{0.65}Sb_{0.35}$ is ~ 7.3×10^3/cm at the wavelength of 1.3 μm.

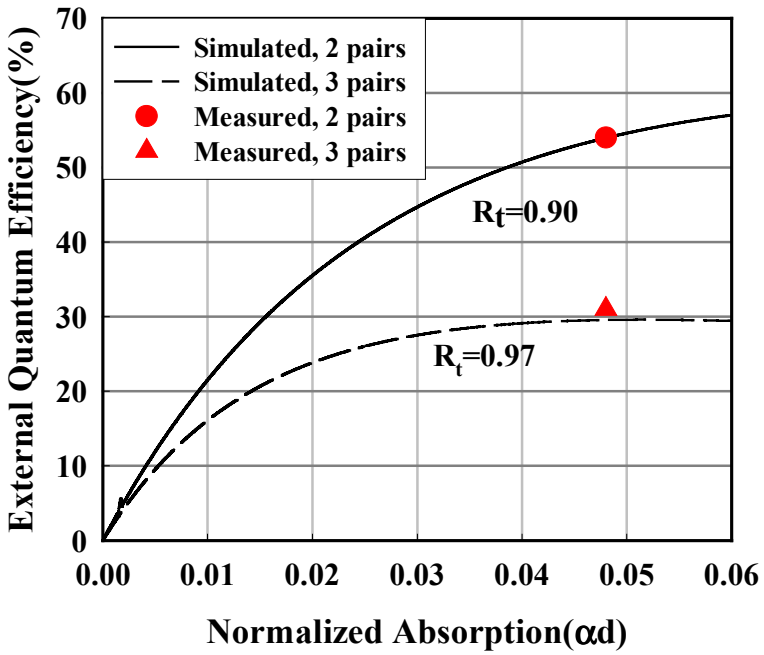

Figure 5.8: Simulated and measured external quantum efficiencies as a function of normalized absorption αd for photodiodes with 2 and 3 pairs of MgF_2/ZnSe layers as the top mirror. The reflectivity of bottom DBR mirror (R_b) is 93%.

Since no material degradation after the growth of ten highly strained GaAsSb layers was observed, the external quantum efficiency of device can be further improved by optimizing bottom mirror growth, adding more GaAsSb layers or using strain compensation [5.3, 5.4].

5.6 SUMMARY

We designed and fabricated a GaAsSb resonant-cavity-enhanced photodiode operating at 1.3 μm. The breakdown voltage was 12V for a 150 μm diameter device and a gain of 10 was obtained near breakdown. The peak external quantum efficiency was 54% at 1.3 μm and the FWHM was 8 nm. The absorption coefficient of $GaAs_{0.65}Sb_{0.35}$ was estimated to be ~7.3×10^3/cm at 1.3 μm. Our initial work on this GaAsSb RCE photodiode shows that GaAsSb is a promising absorption material for 1.3 μm photodiodes on GaAs substrate.

Chapter 6: RCE GaAsSb SACM APD

6.1 INTRODUCTION

In Chapter 5 we demonstrated a resonant-cavity-enhanced (RCE) GaAsSb *p-i-n* photodiode operating at 1.3 μm. The device exhibited an external quantum efficiency of 54% but a high dark current (~5 μA) near breakdown. In this device, the narrow bandgap GaAsSb layers acted as both the absorption region and part of the multiplication region. In order to achieve an adequate gain from the photodiode, a high electric field in the multiplication region is essential. At high electric field, the multiplication and band-to-band tunneling in these GaAsSb layers were the primary components of the dark current. In order to avoid these dark current components, it is necessary to separate the multiplication and absorption regions and tailor the electric field profile. This leads to a modified avalanche photodiode (APD) structure with separate absorption, charge and multiplication regions that is called SACM APD. In long-haul, high-bit-rate fiber optic communication systems, low noise is another critical requirement for the photodetectors in order to improve the detect sensitivity and reduce the number of repeaters and amplifiers during the transmission. The multiplication region of the SACM APD plays an important role in noise performance. By using some low noise materials or structures as the multiplication region and GaAsSb as the absorber, we can obtain APDs operating at 1.3 μm on GaAs substrates with very low noise. In this chapter, we demonstrate a RCE GaAsSb SACM APD operating

at 1.31 μm, which exhibited much lower dark current than the *p-i-n* structure and also very low multiplication noise [6.1].

6.2 LOW NOISE MULTIPLICATION REGION DESIGN

According to the local-field theory [6.2, 6.3], both multiplication noise and gain-bandwidth product of the APDs are determined by the ratio of the electron and hole ionization coefficients of the multiplication materials. Since this ratio is a material property, for a given electric field, efforts to improve the APD performance have focused on optimizing the electric field profile and developing new multiplication materials. GaAs and $Al_xGa_{1-x}As$ APDs with thin multiplication regions have been reported to have very low multiplication noise [6.4-6.8]. The non-local nature of impact ionization has been shown to be responsible for the low noise [6.9, 6.10]. The impact ionization properties of $Al_xGa_{1-x}As$ bulk materials with low Al ratio ($x \leq 0.4$) have been thoroughly studied [6.11, 6.12, 6.13]. Recently, we studied the high-Al-ratio $Al_xGa_{1-x}As$ ($x>0.8$) [6.14] and GaAs/$Al_xGa_{1-x}As$/GaAs impact-ionization-engineered (I^2E) structures [6.15] and obtained very low multiplication noise.

6.2.1 High Al-ratio $Al_xGa_{1-x}As$ Multiplication Region

To study the impact ionization and noise characteristics of $Al_xGa_{1-x}As$, $Al_xGa_{1-x}As$ homojunction APDs with x = 0, 0.2, 0.4, 0.6, 0.8 and 0.9 were grown on (100)-oriented n^+ GaAs substrates in a Varian Gen II MBE system. Two values of multiplication region thickness, 200 nm and 800 nm, were chosen for the APD structures.

The noise power spectral density of the APDs was measured with a HP 8970B noise figure meter. Table 6.1 shows the fitted *k* values from the extracted excess noise factors of the $Al_xGa_{1-x}As$ APDs (x=0.0-0.9). The measured thickness (by SIMS and/or C-V) of the *i* regions is shown below the *k* values.

Table 6.1: Fitted *k* values from the extracted excess noise factors of $Al_xGa_{1-x}As$ APDs with different Al concentrations (x = 0.0-0.9) and *i*-region thickness of 0.2 and 0.8 μm.

Al ratio	0%	20%	40%	60%	80%	90%
i: thick	*k*=0.48 0.79μm[b]	*k*=0.54 0.74μm[b]	*k*=0.36 0.75μm[a]	*k*=0.30 0.77μm[a]	*k*=0.15 0.65μm[a]	*k*<0.1 0.52μm[a]
i: thin	*k*=0.31[c] 0.17μm[b]	*k*=0.24[c] 0.19μm[b]	*k*=0.15 0.17μm[a]	*k*=0.14 0.17μm[a]	*k*=0.13 0.15μm[a]	*k*<0.1 0.14μm[b]

[a]Intrinsic region thickness measured by SIMS.

[b]Intrinsic region thickness measured by *C-V* techniques.

[c]See Ref. 6.4.

For the devices with thick multiplication regions, the fitted *k* values decreased with the increasing of Al concentration from x=0.2 to x=0.9. The decrease in multiplication noise was particularly significant for $x \geq 0.8$. These results indicate that the energy band structure may influence the impact ionization and the multiplication noise in $Al_xGa_{1-x}As$ APDs. For devices with thin multiplication regions, the excess noise factors also decreased with the increasing of Al concentration. Consistent with previous reports [6.16, 6.17], the non-local characteristics of impact ionization yield lower noise in all of the thin APDs compared to the corresponding thick devices. For the $Al_{0.9}Ga_{0.1}As$ APDs, the

excess noise is far below the k = 0.1 reference curve. It appears that the excess noise of $Al_{0.9}Ga_{0.1}As$ APDs does not change significantly with the *i*-region thickness, in contrast to what has been observed for lower Al concentration (x<0.9). The fitted k value of $Al_{0.9}Ga_{0.1}As$ APDs is the lowest (<0.1) among all the $Al_xGa_{1-x}As$ samples. The excess noise factor is comparable to that of silicon APDs, which is usually in the range of $0.02 \leq k \leq 0.05$ [6.18, 6.19].

6.2.2 Impact Ionization Engineered Multiplication Region

Very low multiplication noise has also been achieved by impact ionization engineered (I^2E) structures. This approach utilizes heterojunctions to provide greater localization of impact ionization than what can be achieved in spatially uniform structures. The basic idea of I^2E is to place thin layers with relatively low threshold energy (multiplication layers) on each side of a region with higher ionization coefficients, the separation layer. The goal of the I^2E structure is to enhance impact ionization at the edges in the twin multiplication layers and to suppress it in the center, while, at the same time, using the central separation layer to energize the carriers in transit. Figure 6.1 shows the schematic diagram of the I^2E multiplication region. The structure in Fig. 6.1 has GaAs multiplication layers and $Al_{0.6}Ga_{0.4}As$ separation layer. The dashed lines qualitatively represent the ionization rates for holes and electrons. In order to concentrate impact ionization in the multiplication layers, the difference between the ionization rates in the multiplication layers and the separation layer needs to be as large as possible. The thickness of the separation layer should be thin enough to minimize the probability of impact ionization during transit between the multiplication layers

yet thick enough to energize the carriers prior to injection into the multiplication layers.

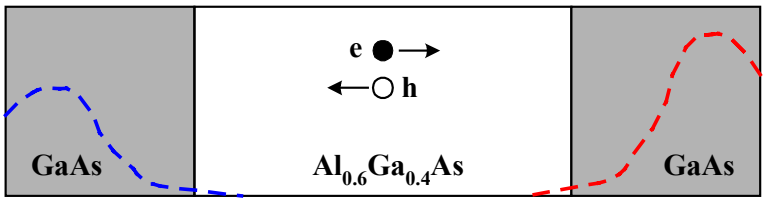

Figure 6.1: Schematic diagram of the impact ionization engineered (I^2E) multiplication region. Dashed lines qualitatively represent the ionization rates of electrons and holes.

I^2E APDs and comparison structures were grown and fabricated and the details were reported in [6.15]. Figure 6.2 shows the excess noise factors *F(M)* extracted from the noise measurement. Owing to the space modulation of impact ionization, the noise was much lower in the twin-well structures than in GaAs and $Al_{0.6}Ga_{0.4}As$ homojunction APDs. For M < 20 the multiplication noise of the 50 nm × 2 device was lower than that of Si APDs and would correspond to negative *k* value, which is further confirmation of the inadequacy of the local-field model for this kind of APD. The apparent variation of the noise with thickness of the twin multiplication regions may be related to the energy and momentum relaxation lengths. At very high gain values, the noise is expected to reflect some multiplication in the separation layer, which would lead to relatively higher noise.

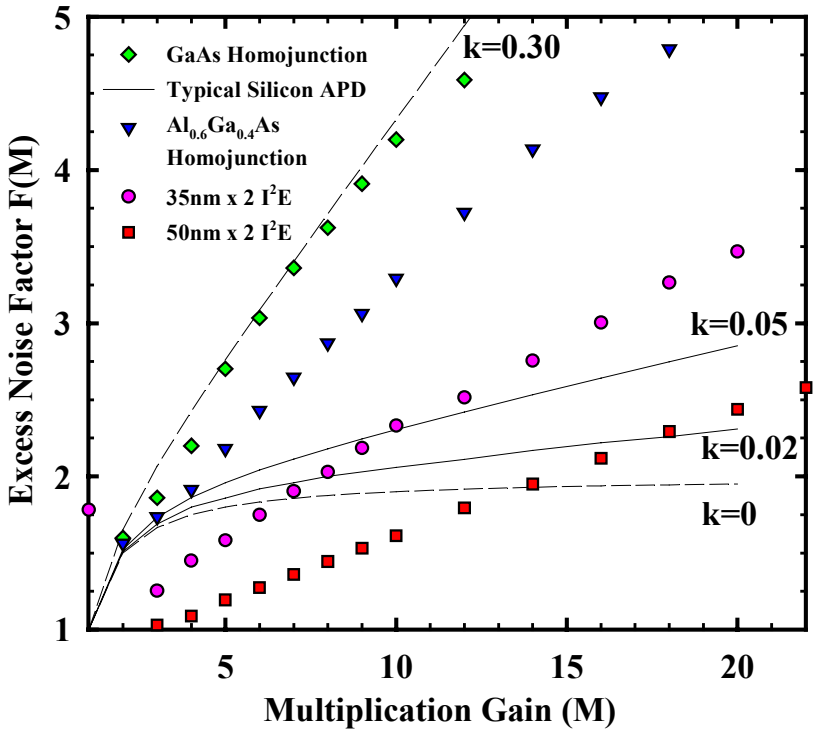

Figure 6.2: Measured excess noise factors versus multiplication gain of the I^2E and comparison APDs.

6.3 STRUCTURE OF RCE GAASSB SACM APD

The schematic diagram of the resonant-cavity-enhanced GaAsSb SACM APD structure with nominal thickness values is shown in Fig. 6.3. From the bottom to the top, the layer structure was: a n^+ GaAs buffer layer, a bottom DBR mirror containing 25 pairs of λ/4 GaAs/AlAs layers with *n*-type doping (Si: $5\times10^{18}/cm^3$), a 460 Å-thick GaAs layer and a 500 Å-thick $Al_{0.9}Ga_{0.1}As$ layer with n-type doping (Si: $5\times10^{18}/cm^3$) as spacer layers, a 2000 Å-thick undoped $Al_{0.9}Ga_{0.1}As$ multiplication layer, a 500 Å-thick lightly doped (Be: $5\times10^{17}/cm^3$) p-type $Al_{0.9}Ga_{0.1}As$ charge layer, an intrinsic region containing two GaAsSb/GaAs

multiple quantum well absorption regions and three GaAs spacer layers, a 958 Å-thick *p*-type (Be: $5\times10^{18}/cm^3$) GaAs spacer layer, a p^{++} (Be: $2\times10^{19}/cm^3$) GaAs cap layer for ohmic contact and 2 pairs of λ/4 MgF_2/ZnSe layers as the dielectric top mirror.

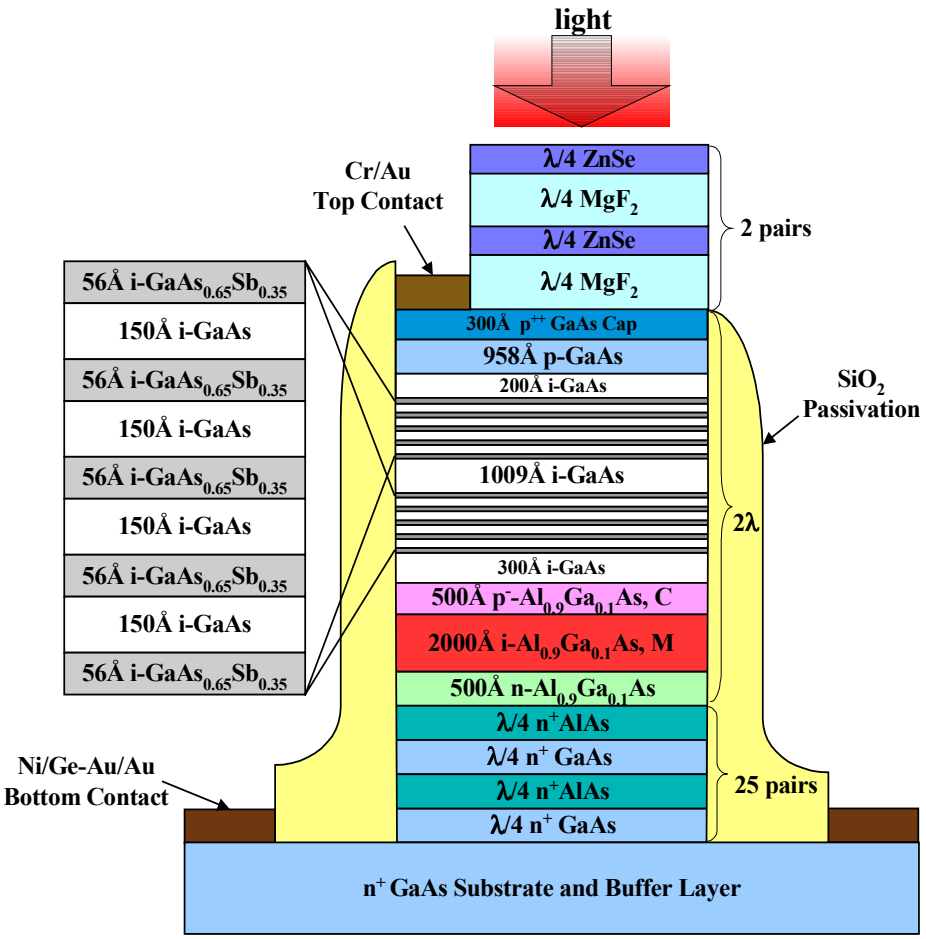

Figure 6.3: Schematic diagram of resonant-cavity-enhance GaAsSb SACM APD.

Compared to the *p-i-n* structure, the essential differences were the 2000Å undoped $Al_{0.9}Ga_{0.1}As$ multiplication region and 500Å lightly doped (Be:

$5\times10^{17}/cm^3$) p-type $Al_{0.9}Ga_{0.1}As$ charge layer used in the SACM structure. The thickness values of GaAsSb absorbers and GaAs spacers were also a little different than those in the *p-i-n* structure in order to fit into the 2λ resonant cavity. Same to the *p-i-n* structure, the two sandwich-like absorption regions were placed at the antinodes of the optical standing wave inside the cavity to enhance the light absorption. The total absorption layer thickness was 56nm in this SACM APD.

Figure 6.4 (a) and (b) show the simulated electric field profiles at breakdown for the *p-i-n* and SACM structures, respectively. We can see that by the separation of GaAsSb absorption regions and undoped $Al_{0.9}Ga_{0.1}As$ multiplication region, the electric field in the intrinsic region was lowered from ~3.9×10^5 V/cm in the *p-i-n* structure to ~2.5×10^5 V/cm in the SACM structure, which could reduce the avalanche multiplication processes in the narrow bandgap GaAsSb layers and decrease the dark current at higher bias.

6.4 MATERIAL GROWTH AND DEVICE FABRICATION

The epi layers were grown on a (100)-oriented n^+ GaAs substrate in a Varian Gen II solid source MBE system. The GaAsSb layers were grown at the optimum growth temperature of 530°C with a Ga growth rate of 0.86 ml/s. The rest of the structure was grown at the deoxidation temperature of 580°C. To obtain a GaAsSb composition that can absorb light at 1.3 μm, As beam equivalent pressure (BEP) of 2.5×10^{-6} Torr and Sb BEP of 5.0×10^{-7} Torr were used during the growth of GaAsSb layers. Measured and simulated X-ray diffraction spectra showed that the Sb mole fraction was approximately 0.35 in these GaAsSb layers.

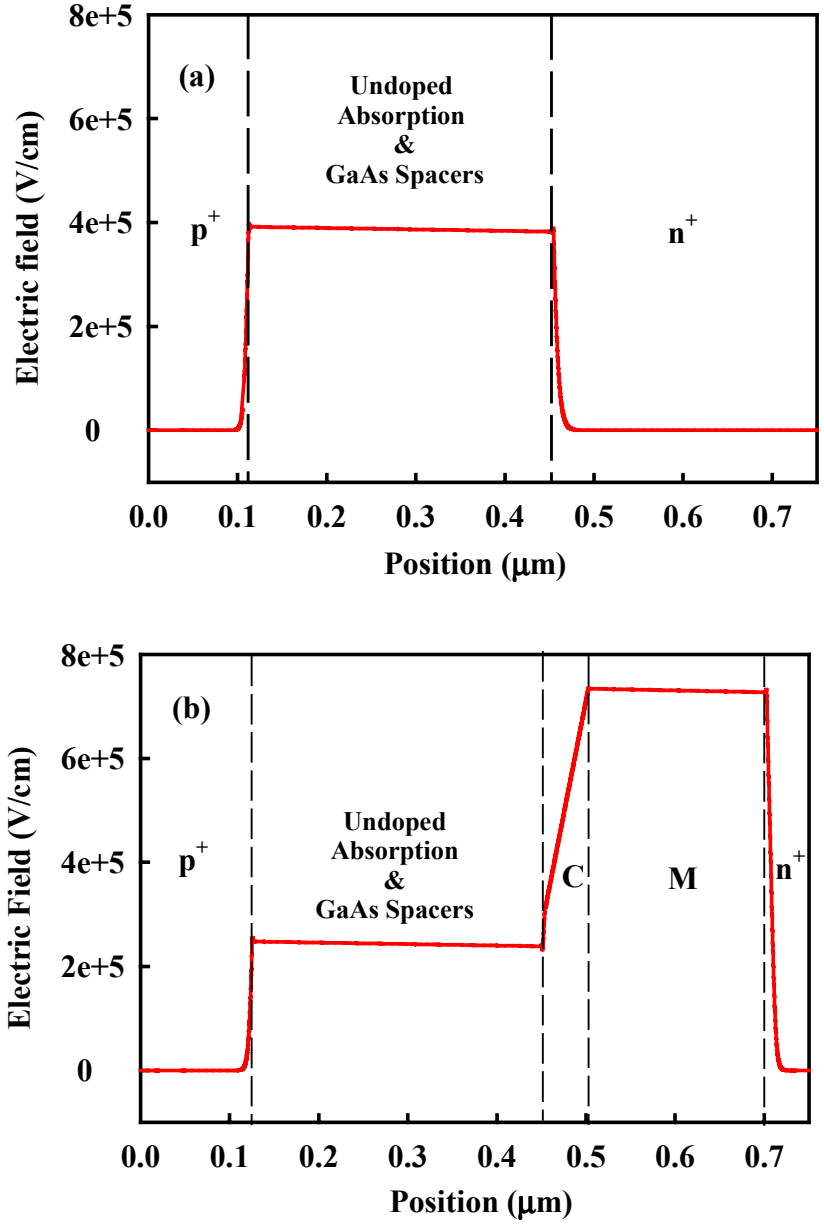

Figure 6.4 Simulated electric field profiles at breakdown in (a) RCE GaAsSb *p-i-n* photodiode and (b) RCE GaAsSb SACM APD.

Device mesas with diameters of ~160 μm were patterned by standard photolithography process and defined by wet chemical etching using a 1:1:8 etch solution of H_3PO_4: H_2O_2: H_2O. SiO_2 was deposited by plasma-enhanced chemical vapor deposition (PECVD) to serve as the passivation of the devices. The ohmic contacts were e-beam evaporated and patterned by a lift-off process. Cr/Au and Ni/Ge-Au/Au were used for the top p-type contact and bottom *n*-type contact, respectively. Two pairs of λ/4 MgF_2/ZnSe layers were e-beam evaporated as the dielectric top mirror for the resonant cavity.

6.5 DEVICE MEASUREMENTS

6.5.1 I-V Curve

The photocurrent and dark current were measured with a HP 4145B semiconductor parameter analyzer. For the compatibility with noise measurement, a stable *cw* Argon UV laser with two lines, 351 nm and 363 nm, was used as the light source.

Figure 6.5 shows the photocurrent, dark current and avalanche multiplication gain as a function of reverse bias voltage for this RCE GaAsSb SACM APD. For comparison, the dark current of the RCE *p-i-n* photodiode with similar GaAsSb absorption regions is also shown in this graph. The breakdown occurred at 24 volts and a multiplication gain up to 40 was obtained near breakdown. At 90% of breakdown, the dark current was approximately 5nA, which was much lower than that of the *p-i-n* structure. As shown Fig. 6.4, the lower electric field in the intrinsic region effectively reduced the multiplication and band-to-band tunneling in the narrow-bandgap GaAsSb layers and

significantly lowered the dark current in this device. The thin lightly doped p-type $Al_{0.9}Ga_{0.1}As$ "charge" layer between the absorption and multiplication regions ensured a low field in the absorption region.

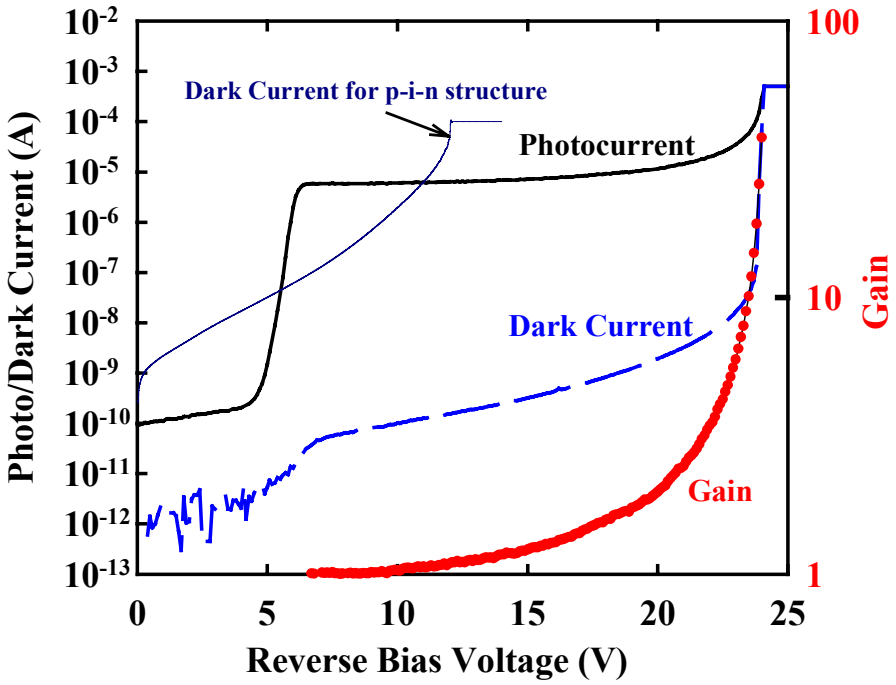

Figure 6.5: Photocurrent, dark current and multiplication gain as a function of reverse bias voltage for the RCE GaAsSb SACM APD.

6.5.2 External Quantum Efficiency

The external quantum efficiency was measured using a tungsten-halogen light source, a spectrometer and a lock-in amplifier. Figure 6.6 shows the external quantum efficiency of the photodiode with 2 pairs of λ/4 MgF_2/ZnSe layers as the

dielectric top mirror. The peak external quantum efficiency was 36% at the wavelength of 1.31 μm and the full width at half maximum (FWHM) was 7 nm.

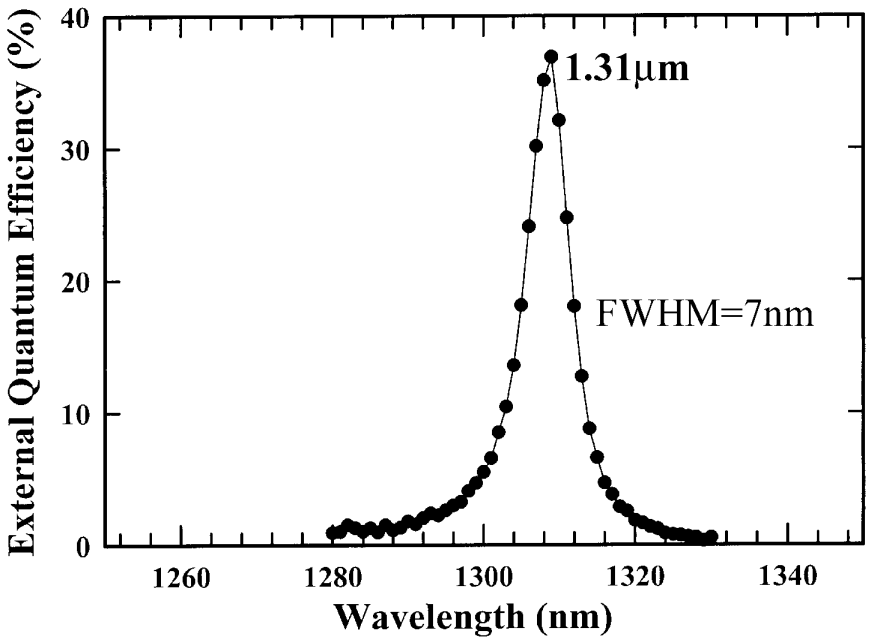

Figure 6.6: External quantum efficiency of the RCE GaAsSb SACM APD with two pairs of MgF_2/ZnSe as the top mirror at unity gain.

Previously, we have estimated that the absorption coefficient α of $GaAs_{0.65}Sb_{0.35}$ at 1.3 μm is approximately 7.3×10^3/cm [6.20]. The total absorption layer thickness d was 56 nm in this SACM APD. Therefore, the external quantum efficiency of this RCE GaAsSb SACM APD should be around 50%. The possible reasons for the lower than expected quantum efficiency are:

1. Bottom mirror growth. Defects and thickness variation in the bottom mirror growth will result in the decrease of bottom mirror reflectivity.

2. Top mirror deposition. The E-beam sputtering can introduce contamination or defects in the dielectric mirrors which reduces the top mirror reflectivity.
3. Positions of absorption regions. If the GaAsSb absorption regions are not accurately positioned at the antinodes of the optical standing wave due to growth rate variation, the light absorption would be reduced.
4. Growth defects in the GaAsSb absorption layers.

6.5.3 Noise

The noise power spectral density of the SACM APD was measured with a HP 8970B noise figure meter that can be programmed to operate at different center frequencies and bandwidths. The environmental noise was reduced by probing the devices with a shielded microwave probe. Signal resonances in the transmission line were minimized with accurate transmission-impedance matching. The noise of the circuit after the photodiode was normalized using a standard calibrated noise source to maintain the accuracy and consistency of the measurement. In the noise measurement, the UV laser was used to ensure pure electron injection into the high electric field $Al_{0.9}Ga_{0.1}As$ multiplication region. More details of the noise measurement were talked in [6.21].

Figure 6.7 shows the extracted excess noise factor, *F (M)*, as a function of multiplication gain. The symbols (♦) were the measured results and the dashed lines were calculated from Equation (4.12) with different k (k = 0, 0.1, 0.2, 0.3, and 0.4). Typical InP-based APDs have k values of ~0.4 [6.7]. The fitted k value

for this RCE GaAsSb SACM APD was approximately 0.1, which is the lowest reported to date for APDs operating at 1.3 μm.

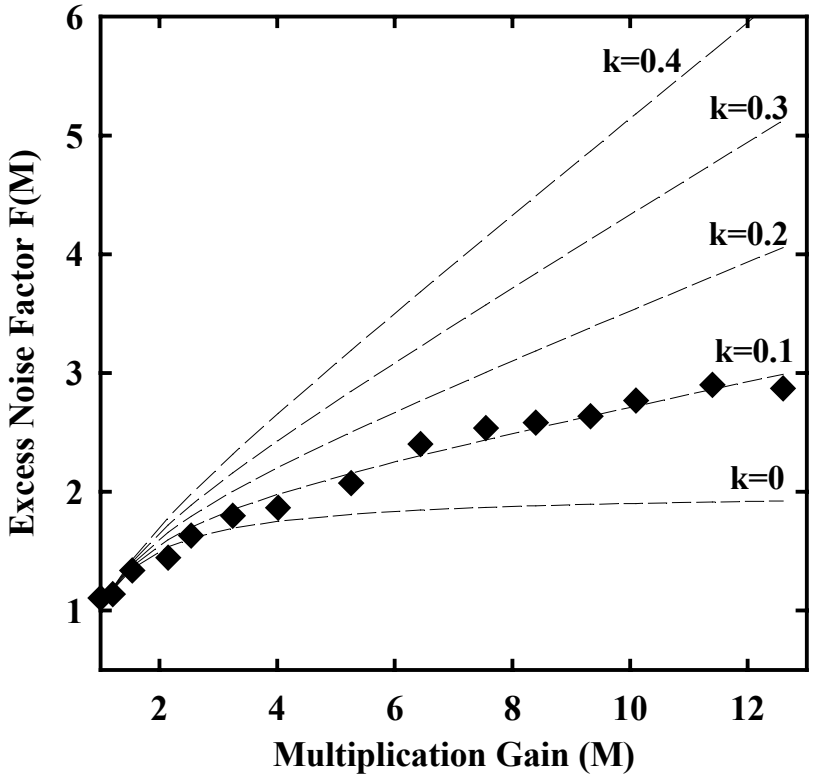

Figure 6.7: The excess noise factor, *F (M)*, versus multiplication gain for the RCE GaAsSb SACM APD. The symbols (♦) represent the measured results, and the dashed lines are the values calculated from the local-field theory and the specified *k*'s.

6.6 SUMMARY

In summary, two multiplication region designs, the high Al-ratio $Al_xGa_{1-x}As$ and impact ionization engineered structures, have been studied. Very low excess noise has been achieved from $Al_xGa_{1-x}As$ with high Al content ($x \geq 0.8$)

and I^2E structure. We also demonstrated a resonant-cavity-enhanced SACM APD with GaAsSb absorption layers and $Al_{0.9}Ga_{0.1}As$ multiplication layer. The peak external quantum efficiency was 36% at the wavelength of 1.31 μm with a full width at half maximum of 7nm. This APD exhibited a low dark current of 5nA at 90% of breakdown and also very low multiplication noise. Our work shows that by using GaAsSb absorber and SACM structure, low noise, low dark current avalanche photodiodes operating at 1.3 μm on GaAs substrates can be realized.

Chapter 7: Conclusions and Future Work

7.1 CONCLUSIONS

This dissertation addresses the issues related to the molecular beam epitaxy growth, device design, fabrication and testing of avalanche photodiodes operating at 1.3 μm on GaAs substrates for the applications in long-haul, fiber optic communication systems. MBE-grown compressively strained $GaAs_{1-x}Sb_x$ layers were used as the absorption regions of the photodiode structures in order to achieve the absorption at 1.3 μm on GaAs substrates. Resonant-cavity-enhanced avalanche photodides were the detectors of choice for high quantum efficiency, high bandwidth, low noise and low dark current.

The MBE growth of GaAsSb layers on GaAs substrates have been studied. Our results show that the optical properties and compositions of GaAsSb layers highly depend on the growth temperatures, the Ga growth rates and the As and Sb fluxes. With the increase of growth temperatures, the Sb desorption from the surface increases and incorporation with Ga decreases, the point defects decrease, and the Sb segregation increases. The optimum growth temperature window of GaAsSb on GaAs substrates is from 500 ºC to 530 ºC. The Sb incorporation with Ga increases at higher Ga fluxes and saturates at Ga growth rates higher than 0.8ml/s. The optimum Ga growth rate is 0.8 ml/s to 1.0 ml/s in order to eliminate the Ga growth rate influence to the composition of GaAsSb. With the same Sb/As flux ratio, the incorporated Sb in the GaAsSb layers decreases at higher As flux. For better photoluminescence results, lower As and Sb mixed flux is desired as

long as the surface is group-V stabilized. At the growth temperature of ~530 °C and Ga growth rate of ~0.9 ml/s, the optimum As and Sb mixed flux is ~3.0×10^{-6} Torr.

We demonstrated two resonant-cavity-enhanced photodiodes with multiple GaAsSb absorption layers on GaAs substrate. The RCE GaAsSb *p-i-n* photodiode exhibited a peak external quantum efficiency of 54% at the wavelength of 1.3 μm with a full-width-at-half-maximum of 8 nm. The dark current of this photodiode was ~5 μA at the reverse bias of 90% of the breakdown. The absorption coefficient of $GaAs_{0.65}Sb_{0.35}$ was estimated to be ~7.3×10^{3}/cm at 1.3 μm. In the RCE GaAsSb SACM APD structure, the high electric field multiplication region was separated from the intrinsic absorption region, which significantly reduced the multiplication and band-to-band tunneling in the narrow bandgap GaAsSb absorption layers. As a result, the RCE GaAsSb SACM APD exhibited very low dark current (~5 nA) at 90% of the breakdown. With 2 pairs of λ/4 MgF_2/ZnSe layers as the dielectric top mirror, the peak external quantum efficiency of this SACM APD was 36% at 1.31 μm and the full width at half maximum (FWHM) was 7 nm. By utilizing thin $Al_{0.9}Ga_{0.1}As$ layer as the multiplication region, very low multiplication noise with *k* value ~0.1 was obtained in the SACM APD. This is the lowest noise reported to date for APDs operating at 1.3 μm.

7.2 FUTURE WORK

We have achieved APDs operating at the wavelength of 1.3 μm on GaAs substrates with low noise, low dark current and reasonable external quantum

efficiency. However, there are still a lot of works need to be done to improve the performance of the photodiodes, which includes:

1. Further optimization of $GaAs_{1-x}Sb_x$ growth. The material quality is very critical to the success of the avalanche photodiodes. Since the optical properties and alloy composition of $GaAs_{1-x}Sb_x$ are influenced by several growth parameters, such as growth temperature, Ga growth rate and As and Sb fluxes, further optimization of combined growth conditions are still highly desired in order to reduce the strain-induced growth defects in the highly strained epitaxial layers.
2. Strain compensation. To obtain 1.3 μm emission on GaAs substrates, more than 35% Sb need to be incorporated into GaAs lattices which produces ~ 3% compressive strain in the GaAsSb layers. The high strain degrades the material quality and limits the absorption layer thickness in the APD. For higher external quantum efficiency, thicker GaAsSb absorber is desired. Strain compensation is one way to reduce the coherent strain and increase the critical thickness of GaAsSb. The basic idea of strain compensation is to grow a thin layer with tensile strain such as GaAsP on top of the layer with compressive strain such as GaAsSb. The compressive and tensile strain will compensate in some extent and thus reduce the overall strain in the layers. The MBE system in the University of Texas at Austin is equipped with a phosphorus source that makes the growth of GaAsP possible. Since GaAsP is also a mixed group-V compound similar to

GaAsSb, the growth and characterization methods of GaAsSb can be used on GaAsP.

3. Design of APDs with high bandwidth and low noise. The speeds of the RCE GaAsSb *p-i-n* photodiode and SACM APD were low due to the carrier trapping at the heterojunction interfaces. For high bandwidth, grading layers should be used at the interfaces between two materials with large bandgap discontinuity. Small device geometry is desired to reduce the *RC* limit. Besides the high Al-ratio $Al_xGa_{1-x}As$, impact ionization engineered structures with ultra low noise can also be used as the multiplication regions of the APDs.

Appendix A: Publications

Journals:

[1] X. Sun**,** S. Wang, J. Hsu, R. Sidhu, X.G. Zheng, X. Li, J. C. Campbell, and A. L. Holmes, Jr, "GaAsSb: a novel material for near infrared photodetectors on GaAs substrates", *IEEE J. Select. Topics Quantum Electron,* vol. 8, no. 4, pp. 817-822, 2002.

[2] X. Sun, S. Wang, X. G. Zheng, X. Li, J. C. Campbell, and A. L. Holmes, Jr., "1.31μm GaAsSb Resonant-cavity-enhanced Separate Absorption, Charge and Multiplication Avalanche Photodiodes with Low Noise", *J. Appl. Phys*., accepted for publication.

[3] X. Sun, J. Hsu, X.G. Zheng, J. C. Campbell, and A. L. Holmes, Jr.,"GaAsSb Resonant-Cavity-Enhanced Photodetector Operating at 1.3μm", *IEEE Photon. Technol. Lett.*, vol. 14, no. 5, pp. 681-683, 2002.

[4] S. Wang, J. B. Hurst, F. Ma, R. Sidhu, X. Sun, X. G. Zheng, A. L. Holmes, Jr., and J. C. Campbell, "Low-Noise Impact-Ionization-Engineered Avalanche Photodiodes Grown on InP Substrates", *IEEE Photon. Technol. Lett.*, accepted for publication.

[5] Xiaowei Li, X. Sun, X. G. Zheng, N. Li, A. L. Holmes, Jr. and J. C. Campbell, "$In_{0.53}Ga_{0.47}As$ Homojunction Photodiode with 68mA Saturation Current", submitted for publication.

[6] S. Wang, R. Sidhu, G. Karve, F. Ma, X. Li, X. G. Zheng, J. B. Hurst, X. Sun, N. Li, A. L. Holmes, Jr., and J. C. Campbell, "A study of low-bias photocurrent gradient of avalanche photodiodes", *IEEE Trans. Electron Devices*, accepted for publication.

[7] S. Wang, F. Ma, R. Sidhu, X. G. Zheng, X. Sun, A. L. Holmes, Jr., and J.C. Campbell, "Ultra-low Noise Avalanche Photodiodes With A "Centered-Well" Multiplication Region", *IEEE J. Quantum Electron.*, accepted for publication.

[8] X. G. Zheng, J. Hsu, X. Sun, J. B. Hurst, X. Li, S. Wang,, A.L. Holmes, Jr., J. C. Campbell, "A 12 × 12 $In_{0.53}Ga_{0.47}As/In_{0.52}Al_{0.48}As$ Avalanche Photodiode Array", *IEEE J. Quantum Electron.,* vol. 38, no. 11, pp. 1536-1540, 2002.

[9] X. G. Zheng, J. B. Hurst, X. Sun, S. Wang, A.L. Holmes, Jr., and J. C. Campbell, "Long Wavelength InGaAs/InP-GaAs/AlGaAs Avalanche Photodiode Implemented by Direct Wafer Bonding", *IEEE Photon. Technol. Lett.*, accepted for publication.

[10] S. Wang, R. Sidhu, X. G. Zheng, X. Li, X. Sun, A. L. Holmes, Jr., and J. C. Campbell, "Low-noise avalanche photodiodes with graded impact ionization Engineered multiplication region", *IEEE Photon. Technol. Lett.*, vol. 13, no. 12, pp. 1346-1348, 2001.

[11] X. G. Zheng, X. Sun, S. Wang, P. Yuan, G. S. Kinsey, A. L. Holmes, Jr., B. G. Streetman, and J. C. Campbell, "Multiplication noise of AlxGa1-xAs avalanche photodiodes with high Al concentration and thin multiplication region", *Appl. Phys. Lett.,* vol. 78, no. 24, pp. 3833-3835, 2001.

[12] P. Yuan, S. Wang, X. Sun, X. G. Zheng, A. L. Holmes, Jr., and J. C. Campbell, "Avalanche photodiodes with an impact-ionization-engineered multiplication region", *IEEE Photon. Technol. Lett.*, vol. 12, no. 10, pp. 1370-1372, 2000.

[13] X. G. Zheng, P. Yuan, X. Sun, G. S. Kinsey, A. L. Holmes, Jr., B. G. Streetman, and J. C. Campbell, "Temperature dependence of the ionization coefficients of $Al_xGa_{1-x}As$", *IEEE J. Quantum Electron*, vol. 36, no. 10, pp. 1168-1173, 2000.

[14] Xinping Qiu, Xiaoguang Sun, Wanci Shen, and Nanping Chen, "Spinel $Li_{1+x}Mn_2O_4$ synthesized by coprecipitation as cathodes for lithium-ion batteries", *Solid State Ionics*, vol. 93, pp. 335-339, 1997.

Conferences:

[15] S. Wang, J. B. Hurst, F. Ma, R. Sidhu, X. Sun, X. G. Zheng, A. L. Holmes, Jr., J. C. Campbell, A. Huntington, and L. A. Coldren "Low-noise InP-based avalanche photodiodes with an Impact-Ionization-Engineered multiplication region", *IEEE Lasers and Electro Optics Society (LEOS) 2002 Annual Meeting,* Glasgow, Scotland, UK, Nov.11-14, 2002.

[16] X. Sun, S. Wang, X. G. Zheng, X. Li, J. C. Campbell, and A. L. Holmes, Jr., "Resonant-cavity-enhanced GaAsSb avalanche photodiodes with separate absorption, charge and multiplication regions operating at 1300nm", *Optical Amplifiers and Their Applications and Integrated Photonics Research,* Vancouver, Canada, July 14-19, 2002.

[17] X. Sun, S. Wang, R. Sidhu, X. G. Zheng, X. Li, J. C. Campbell, and A. L. Holmes, Jr. "MBE Growth and Device Performance of GaAsSb Resonant-Cavity-Enhanced Avalanche Photodiodes with Separate Absorption, Charge and Multiplication Regions", *2002 Electronic Materials Conference*, Santa Barbara, California, June, 2002.

[18] Rubin Sidhu, Xiaoguang Sun, and Archie L. Holmes, Jr., "Influence of growth parameters on Antimony incorporation during Molecular Beam Epitaxy of III-Arsenide-Antimonides", *2002 Electronic Materials Conference*, Santa Barbara, California, June, 2002.

[19] J. B. Hurst, X. G. Zheng, X. Sun, S. Wang, Joe C. Campbell, and Archie L. Holmes, Jr., "Long Wavelength InGaAs/InAlAs/InP-GaAs/AlGaAs Avalanche Photodiode Implemented by Direct Wafer Bonding", *2002 Electronic Materials Conference*, Santa Barbara, California, June, 2002.

[20] J. C. Campbell, S. Wang, X. G. Zheng, G. S. Kinsey, A. L. Holmes, Jr., X. Sun, R. Sidhu, and P. Yuan, " Ultra-low-noise avalanche photodiodes", *Proc. SPIE*, vol. 4283, pp. 480-488, 2001.

[21] S. Wang, X. Sun, X. G. Zheng, A. L. Holmes, J. C. Campbell, and P. Yuan, "Avalanche photodiodes with an impact-ionization-engineered multiplication region", *IEEE Lasers and Electro Optics Society (LEOS) 2000 Annual Meeting*, vol. I, pp. 9-10, 2000.

[22] S. Wang, R. Sidhu, X.G. Zheng, X. Sun, A.L. Holmes, Jr., and J. C. Campbell, "Low noise avalanche photodiodes with a graded Impact-Ionization-Engineered multiplication region", *59th Annual Device Research Conference*, *Latest news*.

Bibliography

Chapter 1:

[1.1] T. Maimann, "Stimulated Optical Radiation in Ruby", *Nature*, vol. 187, pp. 493-494, 1960.

[1.2] K. C. Kao and G. A. Hockman, "Dielectric-fibre surface waveguides for optical frequencies", *Proceedings of the IEE*, vol. 133, pp. 1151-1158, 1966.

[1.3] F. P. Kapron, D. B. Keck, and R. D. Maurer, "Radiation losses in glass optical waveguides", *Appl. Phys. Lett.*, vol. 17, pp. 423-425, 1970.

[1.4] S. B. Alexander, *Optical Communication Receiver Design*, SPIE Optical Engineering Press, London, UK, 1997.

[1.5] B.G. Streetman, *Solid State Electronic Devices*, Fourth Edition, Prentice Hall, New Jersey, 1995.

[1.6] J. C. Campbell, W. T. Tsang, G. J. Qua, and J. E. Bowers, "InP/InGaAsP/InGaAs avalanche photodiodes with 70 GHz gain-bandwidth product", *Appl. Phys. Lett.*, vol. 51, pp. 1454-1456, 1987.

[1.7] F. Capasso, K. Alavi, A. Y. Cho, P. W. Foy, and C. G. Bethea, "New long wavelength $Al_{0.48}In_{0.52}As/Ga_{0.47}In_{0.53}As$ avalanche photodiode grown by molecular beam epitaxy", Appl. Phys. Lett., vol. 43, pp. 1040-1042, 1983.

[1.8] C. Lenox, H. Nie, P. Yuan, G. Kinsey, A. L. Holmes, Jr., B. G. Streetman, and J. C. Campbell, "Resonant-Cavity InGaAs/InAlAs Avalanche Photodiodes with Gain-Bandwidth-Product of 290 GHz", *IEEE Photon. Technol. Lett.*, vol. 11, pp. 1162-1164, 1999.

[1.9] M. MacDougal, P. Dapkus, V. Pudikov, H. Zhao, G. Yang, "Ultralow Threshold Current Vetical-Cavity Surface-Emitting Lasers with AlAs Oxide-GaAs Distributed Bragg Reflectors", *IEEE Photon. Technol. Lett.*, vol. 7, pp. 229-231, 1995.

[1.10] A. Chin, and T. Tang, "Multilayer Reflectors by Molecular Beam Epitaxy for Resonance Enhanced Absorption in Thin High-Speed Detectors", *J. Vac. Sci. Technol.* B. vol. 8, pp. 339-342, 1990.

[1.11] J. Piprek and S. J. B. Yoo, "Thermal comparison of long-wavelength vertical-cavity surface-emitting laser diodes", *Electron. Lett.*, vol. 30, pp. 866-868, 1994.

[1.12] J. Koeth, T. Bleuel, R. Werner and A. Forchel, "1.5 μm Ga(Al)Sb laser grown on GaAs substrate by MBE", *J. Cryst. Growth*, vol. 201-202, pp. 841-843, 1999.

[1.13] M. Kondow, T. Kitatani, S. Nakatsuka, M. C. Larson, K. Nakahara, Y. Yazawa, M. Okai, and K. Uomi, " GaInNAs: a novel material for long-wavelength semiconductor lasers", *IEEE J. Sel. Topics Quantum Electron.* vol. 3, 719-730, 1997.

[1.14] G. Steinle, H. Riechert, A.Yu. Egorov, "Monolithic VCSEL with InGaAsN active region emitting at 1.28μm and CW output power exceeding 500 μW at room temperature", *Electron. Lett.,* vol. 37, pp. 93-95, 2001.

[1.15] X. Yang, M. J. Jurkovic, J. B. Heroux, and W. I. Wang, "Molecular beam epitaxial growth of InGaAsN:Sb/GaAs quantum wells for long-wavelength semiconductor lasers", *Appl. Phys. Lett.*, vol. 75, pp. 178-180, 1999.

[1.16] R. P. Mirin, J. P. Ibbetson, K. Nishi, A. C. Gossard, and J. E. Bowers, "1.3 μm photoluminescence from InGaAs quantum dots on GaAs", *Appl. Phys. Lett.* , vol. 67, pp. 3795-3797, 1995.

[1.17] E. Roan, K. Cheng, "Long-wavelength (1.3 μm) luminescence in InGaAs strained quantum-well structures grown on GaAs", *Appl. Phys. Lett.*, vol. 59, pp. 26988-2690, 1991.

[1.18] K. Mukai, N. Ohtsuka, and M. Sugawara, "Emission from discrete levels in self-formed InGaAs/GaAs quantum dots by electric carrier injection: Influence of photon bottleneck", *Appl. Phys. Lett.*, vol. 68, pp. 3013-3015, 1996.

[1.19] J. J. Dudley, D. I. Babic, R. Mirin, L. Yang, B. I. Miller, R. J. Ram, T. Reynolds, E. L. Hu and J. E. Bowers, "Low threshold, wafer fused long wavelength vertical cavity lasers", *Appl. Phys. Lett.,* vol. 64, pp. 1463-1465, 1994.

[1.20] Z.-H. Zhu, Felix E. Ejeckam, Y. Qian, Jizhi Zhang, Zhenjun Zhang, Gina L. Christenson, and Y. H. Lo, "Wafer bonding technology and its applications in optoelectronic devices and materials", *IEEE J. Sel. Topics Quantum Electron.*, vol. 3, pp. 927-936, 1997.

[1.21] TaekRyong Chung, Naoe Hosoda, Tadatomo. Suga, and Hideki Takagi, "1.3 μm InGaAsP/InP lasers on GaAs substrate fabricated by the surface activated wafer bonding method at room temperature", *Appl. Phys. Lett.*, vol. 72, pp. 1565-1566, 1998.

[1.22] O. Blum and J.F. Klem, "Characteristics of GaAsSb single-quantum-well-lasers emitting near 1.3μm", *IEEE Photon. Technol. Lett.*, vol. 12, pp. 771-773, 2000.

[1.23] T. Anan, M. Yamada, K. Nishi, K. Kurihara, K. Tokutome, A. Kamei and S. Sugou, "Continuous-wave operation of 1.30μm GaAsSb/GaAs VCSELs", *Electron. Lett.*, vol. 37, pp. 566-567, 2001.

[1.24] M. Yamada, T. Anan, K. Tokutome, A. Kamei, K. Nishi, and S. Sugou, " Low-Threshold Operation of 1.3-μm GaAsSb Quantum-Well Lasers Directly Grown on GaAs Substrates", *IEEE Photon. Technol. Lett.,* vol. 12, pp. 774-776, 2000.

[1.25] J. E. Cunningham, M. Dinu, J. Shah, F. Quochi, D. Kilper, W. Y. Jan, M. D. Williams, A. Mills, and W. E. Henderson, "Growth and optical properties of GaAsSb quantum wells for 1.3 μm VCSELs", *J. Vac. Sci. Technol. B*, vol. 19, pp. 1948-1952, 2001.

[1.26] K. D. Choquette, J. F. Klem, A. J. Fischer, O. Blum A. A. Allerman, I. J. Fritz, S. R. Kurtz, W. G. Breiland, R. Sieg, K. M. Geib, J. W. Scott and R. L. Naone, "Room temperature continuous wave InGaAsN quantum well vertical-cavity lasers emitting at 1.3 μm", *Electron. Lett.,* vol. 36, pp. 1388-1390, 2000.

[1.27] M. C. Larson, M. Kondow, T. Kitatani, K. Nakahara, K. Tamura, H. Inoue, and K. Uomi, "GaInNAs-GaAs long-wavelength vertical-cavity surface-emitting laser diodes", *IEEE Photon. Technol. Lett.,* vol. 10. pp. 188-190, 1998.

[1.28] J. B. Héroux, X. Yang and W. I. Wang, "GaInNAs resonant-cavity-enhanced photodetector operating at 1.3 μm", *Appl. Phys. Lett.,* vol. 75, pp. 2716-2718, 1999.

[1.29] D. W. Gotthold, S. Govindaraju, T. Mattord, A. L. Holmes, Jr., and B. G. Streetment, "Growth of GaNAs by molecular beam epitaxy using a N_2/Ar rf plasma", *J. Vac. Sci. Technol. A*, vol. 18, pp. 461-464, 2000.

[1.30] I.–H. Tan, J. J. Dudley, D. I. Babic, D. A. Cohen, B. D. Young, E. L. Hu, J. E. Bowers, B. I . Miller, U. Koren, and M. G. Young, "High quantum efficiency and narrow absorption bandwidth of the wafer-fused resonant $In_{0.53}Ga_{0.47}As$ photodetectors", *IEEE Photon. Technol. Lett,* vol. 6, pp. 811-813, 1994.

[1.31] I.-H. Tan, E. L. Hu, J. E. Bowers, and B. I. Miller, "Modeling and performance of wafer-fused resonant-cavity enhanced photodetectors", *IEEE J. Quantum Electron.*, vol. 31, pp. 1863-1875, 1995.

[1.32] D. L. Huffaker, G. Park, Z. Zou, O. B. Shchekin and D. G. Deppe, "1.3μm room-temperature GaAs-based quantum-dot laser", *Appl. Phys. Lett.,* vol. 73, pp. 2564-2566, 1998.

[1.33] M. Yamada, T. Anan, K. Tokutome, K. Nishi, A. Gomyo, and S. Sugou, "Low-threshold lasing at 1.3μm from GaAsSb quantum wells directly grown on GaAs substrates", *Proc. LEOS' 98, 11th Annual Meeting,* IEEE Lasers and Electro-Optics Society 1998 Annual Meeting, pp. 149, 1998.

[1.34] J. C. Campbell, D. L. Huffaker, H. Deng and D. G. Deppe, "Quantum dot resonant cavity photodiode with operation near 1.3μm wavelength", *Electron. Lett.,* vol. 33, pp. 1337-1339, 1997.

[1.35] F. Quochi, J. E. Cunningham, M. Dinu, and J. Shah, "Room temperature operation of GaAsSb/GaAs quantum well VCSELs at 1.29μm", *Electron. Lett.,.* vol. 36, pp. 2075-2076, 2000.

[1.36] X. Sun, J. Hsu, X. G. Zheng, J. C. Campbell, and A. L. Holmes, Jr., "GaAsSb resonant-cavity-enhanced photodetectors operating at 1.3 μm, *IEEE Photon. Technol. Lett.*, vol. 14, pp. 681-683, 2002.

[1.37] C. Hu, K. A. Anselm, B. G. Streetman and J. C. Campbell, "Noise characteristics of thin multiplication region of GaAs avalanche photodiodes", *Appl. Phys. Lett.*, vol. 69, pp. 3734-3736, 1996.

[1.38] C. Lenox, P. Yuan, H. Nie, O. Baklenov, C. Hansing, J. C. Campbell, and B. G. Streetman, "Thin multiplication region InAlAs homojunction avalanche photodiodes," *Appl. Phys. Lett*., vol. 73, pp. 783-784, 1998.

[1.39] K. F. Li, D. S. Ong, J. P. R. David, G. J. Rees, R. C. Tozer, P. N. Robson, and R. Grey, "Avalanche multiplication noise characteristics in thin GaAs p^+-i-n^+ diodes", *IEEE Trans. Electron Dev.*, vol. 45, pp. 2102-2107, 1998.

[1.40] P. Yuan, H. Chad, K. A. Anselm, C. Lenox, H. Nie, H. L. Holmes, B. G. Streetman, and J. C. Campbell, "Impact Ionization Characteristics of III-V Semiconductors in a Wide Range of Multiplication Region Thickness," *IEEE J. Quantum Electron.*, vol. 36, pp. 198-204, 2000.

[1.41] Y. Okuto and C. R. Crowell, "Ionization coefficients in semiconductors: A nonlocal property," *Phys. Rev. B*, vol. 10, pp. 4284-4296, 1974.

[1.42] X. Li, X. Zheng, S. Wang, F. Ma, J. C. Campbell, "Calculation of gain and noise with dead space for GaAs and $Al_xGa_{1-x}As$ avalanche photodiodes", *IEEE Trans. Electron Devices*, vol. 49, pp. 1112-1117, 2002.

[1.43] R. J. McIntyre, "Multiplication noise in uniform avalanche diodes", *IEEE Trans. on Electron Dev.,* vol. 13, 1966.

Chapter 2:

[2.1] A. Cho, "Film Deposition by Molecular Beam Techniques", *J. Vac. Sci. Technol.,* vol. 8, pp. S31-S38, 1971.

[2.2] A. Cho, "Molecular Beam Epitaxy", *Prog. Solid-State Chem.,* vol. 10, pp. 157-192, 1975.

[2.3] C. T. Foxon, "MBE growth of GaAs and III-V alloys", *J. Vac. Sci. Technol. B*, vol. 1, pp. 293-297, 1983.

[2.4] V. Swaminathan, A. Macrander, *Material Aspects of GaAs and InP Based Structures*, Prentice-Hall, 1991.

[2.5] G. W. Wicks, M. W. Koch, J. A. Varriano, F. G. Johnson, C. R. Wie, H. M. Kim, and P. Colombo, "Use of a valved, solid phosphorus source for the growth of $Ga_{0.5}In_{0.5}P$ and $Al_{0.5}In_{0.5}P$ by molecular beam epitaxy", *J. Vac. Sci. Technol. B,* vol. 59, pp. 342-344, 1991.

[2.6] W. E. Hoke, D. G. Weir, P. J. Lemonias, H. T. Hendriks, G. S. Jackson, and P. Colombo, "Solid source molecular-beam epitaxial growth of $Ga_{0.5}In_{0.5}P$

using a valved, three-zone phosphorus source", *J. Vac. Sci. Technol. B,* vol. 13, pp. 733-735, 1995.

[2.7] M. Herman and H. Sitter, *Molecular Beam Epitaxy-Fundamentals and Current Status,* 2nd Edition, Springer Series in Materials Science 7, Springer-Verlag Berlin Heidelberg, New York, 1996.

[2.8] K.-Y. Cheng, "Molecular Beam Epitaxy Technology of III-V Compound Semiconductors for Optoelectronic Application", *Proc. IEEE,* vol. 85, pp. 1694-1714, 1997.

[2.9] E. H. C. Parker, *The Technology and Physics of Molecular Beam Epitaxy,* Plenum Press, New York, 1985.

[2.10] K. A. Anselm, *High-performance resonant-cavity enhanced photodiodes grown by molecular beam epitaxy,* Ph.D. Dissertation, University of Texas at Austin, 1997.

[2.11] P. F. Fewster and C. J. Curling, "Composition and lattice-mismatch measurement of thin semiconductor layers by x-ray diffraction", *J. Appl. Phys.*, vol. 62, pp. 4154-4158, 1987.

[2.12] C. R. Wie, "Rocking curve peak shift in thin semiconductor layers", *J. Appl. Phys.*, vol. 66, pp. 985-988, 1989.

Chapter 3:

[3.1] J. R. Pessetto, and G. B. Stringfellow, "$Al_xGa_{1-x}As_ySb_{1-y}$ phase diagram", *J. Cryst. Growth*, vol. 62, pp. 1-6, 1983.

[3.2] H. C. Chen, A. B. Rane, D. X. Zhang, S. J. Murry, S. S. Pei, Y. K. Tao, P. J. Pearah and K. Y. cheng, "Molecular-beam epitaxy growth and characterization of high quality GaAsSb", *J. Vac. Sci. Technol. B*, vol. 13, pp. 706-708, 1995.

[3.3] E. Hall, R. Naone, J. E. English, H.-R. Blank, J. Champlain, and H. Kroemer, "Operational experience with a valved antimony cracker source for use in molecular beam epitaxy", *J. Vac. Sci. Technol. B*, vol. 16, pp. 2660-2664, 1998.

[3.4] J. E. Cunningham, M. Dinu, J. Shah, F. Quochi, D. Kilper, W. Y. Jan, M. D. Williams, A. Mills, and W. E. Henderson, "Growth and optical properties of GaAsSb quantum wells for 1.3μm VCSELs", *J. Vac. Sci. Technol. B*, vol. 19, pp. 1948-1952, 2001.

[3.5] M. J. Cherng, Y. T. Cherng, H. R. Jen, P. Harper, R. M. Cohen, and G. B. Stringfellow, "OMVPE growth of the metastable III/V alloy $GaAs_{0.5}Sb_{0.5}$", *J. Electron. Mater.,* vol. 15, pp. 79-85, 1986.

[3.6] X. G. Xu, J. Hu, S. P. Watkins, N. Matine, M. W. Dvorak, and C. R. Bolognesi, "Metalorganic vapor phase epitaxy of high quality GaAs0.5Sb0.5 and its application to heterostructure bipolar transistors", *Appl. Phys. Lett.,* vol. 74, pp. 976-978, 1999.

[3.7] A. Bosacchi, S. Franchi, P. Allegri, V. Avanzini, A. Baraldi, R. Magnanini, M. Berti, D. De Salvador, and S. K. Sinha, "Composition control of GaSbAs alloys", *J. Cryst. Growth,* vol. 201-202, pp. 858-860, 1999.

[3.8] G. Almuneau, E. Hall, S. Nakagawa, J. K. Kim, D. Lofgreen, O. Sjolund, C. Luo, D. R. Clarke, J. H. English, and L. A. Coldren, "Molecular beam epitaxial growth of monolithic 1.55μm vertical cavity surface emitting lasers with AlGaAsSb/AlAsSb Bragg mirrors", *J. Vac. Sci. Technol B,* vol. 18, pp. 1601-1604, 2000.

[3.9] Frederic, Genty, Guilhem Almuneau, Laurent Chusseau, Arnaud Wilk, Serge Gaillard, Guilhem Boissier, Pierre Grech, and Joel Jacquet, "Growth and characterization of vertical cavity structures on InP with GaAsSb/AlAsSb Bragg mirrors for 1.55μm emission", *J. Cryst. Growth*, vol. 201-202, pp. 1024-1027, 1999.

[3.10] C. T. Foxon, "MBE growth of GaAs and III-V alloys", *J. Vac. Sci. Technol. B*, vol. 1, pp. 293-297, 1983.

[3.11] P. D. Brewer, D. H. Chow, and R. H. Miles, "Atomic antimony for molecular beam epitaxy of high quality III-V semiconductor alloys", *J. Vac. Sci. Technol. B*, vol. 14, pp. 2335-2338, 1996.

[3.12] J. Kordis and K. A. Gingerich, "Mass spectroscopic investigation of the equilibrium dissociation of gaseous Sb_2, Sb_3, Sb_4, SbP, SbP_3, and P_2", *J. Chem. Phys.*, vol. 58, pp. 5141-5149, 1973.

[3.13] G. Almuneau, E. Hall, S. Mathis, and L. A. Coldren, "Accurate control of Sb composition in AlGaAsSb alloys on InP substrates by molecular beam epitaxy", *J. Cryst. Growth*, vol. 208, pp.113-116, 2000.

[3.14] K. R. Evans, C. E. Stutz, P. W. Yu, and C. R. Wie, "Mass-spectrometric determination of antimony incorporation during III-V molecular beam epitaxy", *J. Vac. Sci. Technol. B,* vol. 8, pp. 271-275, 1990.

[3.15] Ron Kaspi, and Keith R. Evans, "Sb-surface segregation and the control of compositional abruptness at the GaAsSb/GaAs interface", *J. Cryst. Growth*, vol. 175-176, pp. 838-843, 1997.

[3.16] J. M. Moison, C. Guille, F. Houzay, F. Barthe, and M. Van Rompay, "Surface segregation of third-column atoms in group III-V arsenide compounds: ternary alloys and heterostructures", *Phys. Rev. B*, vol. 40, pp. 6149-6162, 1989.

[3.17] M. Yano, M. Ashida, A. Kawaguchi, Y. Iwai, and M. Inoue, "Molecular-beam epitaxial growth and interface characteristics of GaAsSb on GaAs substrates", *J. Vac. Sci. Technol. B,* vol. **7**, pp. 199-203, 1989.

[3.18] J. F. Klem, O. Blum, S. R. Kurtz, I. J. Fritz, and K. D. Choquette, "GaAsSb/InGaAs type-II quantum wells for long-wavelength lasers on GaAs substrates", *J. Vac. Sci. Technol. B*, vol. 18, pp. 1605-1608, 2000.

[3.19] A. Yamamoto, Y. Kawamura, H. Naito, and N. Inoue, "Optical properties of $GaAs_{0.5}Sb_{0.5}$ and $In_{0.53}Ga_{0.47}As/GaAs_{0.5}Sb_{0.5}$ type-II single hetero-structures lattice-matched to InP substrates grown by molecular beam epitaxy", *J. Cryst. Growth*, vol. 201-202, pp. 872-876, 1999.

[3.20] J. Klem, D. Huang, H. Morkoc, Y. E. Ihm, and N. Otsuka, "Molecular beam epitaxial growth and low-temperature optical characterization of $GaAs_{0.5}Sb_{0.5}$ on InP", *App. Phys. Lett.*, vol. 50, pp. 1364-1366, 1987.

Chapter 4:

[4.1] E. Desurvire, *Erbium-Doped Fiber Amplifiers*, Wiley Inter-Science, 1994.

[4.2] P. Bhattacharya, *Semiconductor Optoelectronic Devices*, Second Edition, Prentice-Hall, New Jersey, 1997.

[4.3] C. R. Pollock, *Fundamentals of Optoelectronics*, Richard D. Irwin, Inc., 1995.

[4.4] B. K. Ridley, *Quantum Processes in Semiconductors*, Oxford University Press, New York, 1982.

[4.5] R. J. McIntyre, "Multiplication noise in uniform avalanche diodes", *IEEE Trans. on Electron Dev.,* vol. ED-13, pp. 164-168, 1966.

[4.6] R. J. McIntyre, "The distribution of gains in uniformly multiplying avalanche photodiodes: Theory", *IEEE Trans. on Electron Dev.*, vol. ED-19, pp. 703-713, 1972.

[4.7] R. B. Emmons, "Avalanche-Photodiode Frequency Response", *J Appl. Phys.*, vol. 38, pp. 3705-3714, 1967.

[4.8] Y. Okuto and C. R. Crowell, "Ionization coefficients in semiconductors: A nonlocal property," *Phys. Rev. B*, vol. 10, pp. 4284-4296, 1974.

[4.9] J. S. Marsland, "On the effect of ionization dead spaces on avalanche multiplication and noise for uniform electric field," *J. Appl. Phys.*, vol. 67, pp. 1929-1933, 1990.

[4.10] C. Hu, K. A. Anselm, B. G. Streetman and J. C. Campbell, "Noise characteristics of thin multiplication region of GaAs avalanche photodiodes", *Appl. Phys. Lett.*, vol. 69, pp. 3734-3736, 1996.

[4.11] G. M. Dunn, G. J. Rees, J. P. R. David, S. A. Plimmer, and D. C. Herbert, "Monte Carlo simulation of impact ionization and current multiplication in short GaAs p^+in^+ diodes," *Semicond. Sci. Techno*l., vol. 12, pp. 111-120, 1997.

[4.12] P. Yuan, C. C. Hansing, K. A. Anselm, C. Lenox, H. Nie, H. L. Holmes, B. G. Streetman, and J. C. Campbell, "Impact Ionization Characteristics of III-V Semiconductors in a Wide Range of Multiplication Region Thickness," *IEEE J. Quantum Electron.*, vol. 36, pp. 198-204, 2000.

[4.13] M. M. Hayat, B. E. A. Saleh, and M. C. Teich, "Effect of dead space on gain and noise of double-carrier-multiplication avalanche photodiodes," *IEEE Trans. Electron De*v., vol. 39, pp. 546-552, 1992.

[4.14] C. Lenox, P. Yuan, H. Nie, O. Baklenov, C. Hansing, J. C. Campbell, and B. G. Streetman, "Thin multiplication region InAlAs homojunction avalanche photodiodes," *Appl. Phys. Lett*., vol. 73, pp. 783-784, 1998.

[4.15] A. Chin and T. Y. Chang, "Multilayer Reflectors by Molecular Beam Epitaxy for Resonance Enhanced Absorption in Thin High-Speed Detectors", *J. Vac. Sci. Technol. B*, vol. 8, pp. 339-342, 1990.

[4.16] K. Kishino, M. Ünlü, J-I. Chyi, J. Reed, L. Arsenault, and H. Morkoc, "Resonant Cavity Enhanced (RCE) Photodetectors", *IEEE J. Quantum Electron.*, vol. 27, pp. 2025-2034, 1991.

[4.17] K. A. Anselm, H. Nie, C. Hu, C. Lenox, P. Yuan, G. Kinsey, J. C. Campbell, and B. G. Streetman, "Performance of Thin Separate Absorption, Charge, and Multiplication Avalanche Photodiodes", *IEEE J. Quantum Electron.*, vol. 34, pp. 482-490, 1998.

[4.18] E. Hecht*, Optics*, Second Edition, Addison-Wesley, pp. 373-375, 1987.

[4.19] C. Weisbuch, and E. Burstein, *Confined Electrons and Photons: New Physcis and Devices*, London, Plenum Press, 1995.

[4.20] J. L. Moll, *Physics of Semiconductors*, New York, McGraw-Hill, 1964.

[4.21] L. E. Tarof, D. G. Knight, K. E. Fox, C. J. Inier, N. Puetz, and H. B. Kim, "Planar InP/InGaAs Avalanche Photodetectors with Partial Charge Sheet in Device Periphery", *Appl. Phys. Lett.*, vol. 57, pp. 670-672, 1990.

[4.22] L. E. Tarof, J. Yu, R. Bruce, D. G. Knight, T. Baird, and B. Oosterbrink, "High-Frequency Performance of Separate Absorption, Grading, Charge and Multiplication InP/InGaAs Avalanche Photodiodes", *IEEE Photon. Technol. Lett*., vol. 5, pp. 672-674, 1993.

[4.23] H. Nie, K. A. Anselm, C. Lenox, P. Yuan, C. Hu, G. Kinsey, B. G. Streetman, and J. C. Campbell, "Resonant-cavity separate absorption, charge and multiplication avalanche photodiodes with high-speed and high gain-bandwidth product", *IEEE Photon. Technol. Lett.,* vol. 10*,* pp. 409-411 , 1998.

[4.24] B.G. Streetman, *Solid State Electronic Devices*, Fourth Edition, Prentice Hall, New Jersey, 1995.

Chapter 5:

[5.1] S. R. Forrest, M. DiDomenico, Jr., R. G. Smith, and H. J. Stocker, "Evidence for tunneling in reverse-biased III-V photodetector diodes", *Appl. Phys. Lett.*, vol. 36, pp. 580-582, 1980.

[5.2] S. R. Forrest, R. F. Leheny, R. E. Nahory, and M. A. Pollack, "$In_{0.53}Ga_{0.47}As$ photodiodes with dark current limited by generation-recombination and tunneling", *Appl. Phys. Lett.*, vol. 37, pp. 322-324, 1980.

[5.3] S. R. Johnson, P. Dowd, W. Braun, U. Koelle, C. M. Ryu, M. Beaudoin, C. -Z. Guo, and Y. -H. Zhang, "Long wavelength pseudomorphic InGaPAsSb type-I and type-II active layers grown on GaAs", *J. Vac. Sci. Technol. B*, vol. 18, pp. 1545-1548, May 2000.

[5.4] T. Anan, M. Yamada, K. Nishi, K. Kurihara, K. Tokutome, A. Kamei and S. Sugou, "Continuous-wave operation of 1.30μm GaAsSb/GaAs VCSELs", *Electron. Lett.,* vol. 37, pp. 566-567, 2001.

Chapter 6:

[6.1] X. Sun**,** S. Wang, J. Hsu, R. Sidhu, X.G. Zheng, X. Li, J. C. Campbell, and A. L. Holmes, Jr, "GaAsSb: a novel material for near infrared photodetectors on GaAs substrates", *IEEE J. Select. Topics Quantum Electron*., vol. 8, no. 4, pp. 817-822, 2002.

[6.2] R. J. McIntyre, "Multiplication noise in uniform avalanche diodes", *IEEE Trans. on Electron Dev.,* vol. ED-13, pp. 164-168, 1966.

[6.3] R. B. Emmons and G. Lucovsky, "The frequency response of avalanching photodiodes", *IEEE Trans. Electron Devices*, vol. 13, pp. 297-305, 1966.

[6.4] C. Hu, K. A. Anselm, B. G. Streetman, and J. C. Campbell, "Noise characteristics of thin multiplication region GaAs avalanche photodiodes," *Appl. Phys. Lett*., vol. 69, no. 24, pp. 3734–3736, 1996.

[6.5] K. F. Li, S. A. Plimmer, J. P. R. David, R. C. Tozer, G. J. Rees, P. N. Robson, C. C. Button, and J. C. Clark, "Low avalanche noise characteristics in thin InP p^+-i-n^+ diodes with electron initiated multiplication," *IEEE Photon. Technol. Lett*., vol. 11, pp. 364–366, 1999.

[6.6] C. Lenox, P. Yuan, H. Nie, O. Baklenov, C. Hansing, J. C. Campbell, and B. G. Streetman, "Thin multiplication region InAlAs homojunction avalanche photodiodes," *Appl. Phys. Lett.*, vol. 73, pp. 783–784, 1998.

[6.7] P. Yuan, C. C. Hansing, K. A. Anselm, C. Lenox, H. Nie, H. L. Holmes, B. G. Streetman, and J. C. Campbell, "Impact ionization characteristics of III–V semiconductors in a wide range of multiplication region thickness," *IEEE J. Quantum Electron.*, vol. 36, pp. 198-204, 2000.

[6.8] D. S. Ong, K. F. Li, G. J. Rees, G. M. Dunn, J. P. R. David, and P. N. Robson, "A Monte Carlo investigation of multiplication noise in thin p^+-i-n^+ GaAs avalanche photodiodes," *IEEE Trans. Electron Device*s, vol. 45, pp. 1804–1810, Aug. 1998.

[6.9] J. S. Marsland, "On the effect of ionization dead spaces on avalanche multiplication and noise for uniform electric field," *J. Appl. Phys.*, vol. 67, pp. 1929-1933, 1990.

[6.10] M. M. Hayat, B. E. A. Saleh, and M. C. Teich, "Effect of dead space on gain and noise of double-carrier-multiplication avalanche photodiodes," *IEEE Trans. Electron De*v., vol. 39, pp. 546-552, 1992.

[6.11] V. M. Robbins, S. C. Smith, and G. E. Stillman, "Impact Ionization in $Al_xGa_{1-x}As$ for x=0.1-0.4", *Appl. Phys. Lett.*, vol. 52, no. 4, pp. 296-298, 1988.

[6.12] T. Kagawa, H. Iwamura, O. Mikami, "Dependence of the GaAs/AlGaAs superlattice ionization rate on Al content", *Appl. Phys. Lett.*, vol. 54, no. 1, pp. 33-35, 1989.

[6.13] F-Y. Juang, U. Das, Y. Nashimoto, and P. K. Bhattacharya, "Electron and hole impact ionization coefficients in GaAs-$Al_xGa_{1-x}As$ superlattices", Appl. Phys. Lett., vol. 47, no. 9, pp. 972-974, 1985.

[6.14] X. G. Zheng, X. Sun, S. Wang, P. Yuan, G. S. Kinsey, A. L. Holmes, Jr., B. G. Streetman, and J. C. Campbell, "Multiplication noise of $Al_xGa_{1-x}As$ avalanche photodiodes with high Al concentration and thin multiplication region", *Appl. Phys. Lett.*, vol. 78, pp. 3833-33835, 2001.

[6.15] P. Yuan, S. Wang, X. Sun, X. G. Zheng, A. L. Holmes, Jr., and J. C. Campbell, "Avalanche photodiodes with an impact-ionization-engineered multiplication region", *IEEE Photon. Technol. Lett.*, vol. 12, pp. 1370-1372, 2000.

[6.16] K. F. Li, D. S. Ong, J. P. R. David, G. J. Rees, R. C. Tozer, P. N. Robson, and R. Grey, "Avalanche multiplication noise characteristics in thin GaAs p^+-i-n^+ diodes", *IEEE Trans. Electron Devices*, vol. 45, pp. 1804-1810, 1998.

[6.17] S. A. Plimmer, J. P. R. David, D. C. Herbert, T. –W. Lee, G. J. Rees, P. A. Houston, R. Grey, P. N. Robson, A. W. Higgs, and D. R. Wight, "Investigation of Impact Ionization in Thin GaAs Diodes", IEEE Trans. Electron Devices, vol. 43, no. 7, pp. 1066-1072, 1996.

[6.18] H. Melchior, A. R. Hartman, D. P. Schinke, and T. E. Sidel, "Planar Epitaxial Silicon Avalanche Photodiode," *Bell Sys. Tech. J.*, pp. 1791-1807, 1978.

[6.19] T. Kaneda, H. Matsumoto, and T. Yamaoka, "A Model for Reach-Through Avalanche Photodiodes (RAPD's)," *J. Appl. Phys.*, vol. 47, pp. 3135-3139, 1976.

[6.20] X. Sun, J. Hsu, X. G. Zheng, J. C. Campbell, and A. L. Holmes, Jr., "GaAsSb Resonant-Cavity-Enhanced Photodetector operating at 1.3 μm", *IEEE Photon. Technol. Lett.*, vol. 14, no. 5, pp. 681-683, 2002.

[6.21] P. Yuan, K. A. Anselm, C. Hu, H. Nie, C. Lenox, A. L. Holmes, B. G. Streetman, J. C. Campbell, and R. J. McIntyre, "A new look at impact ionization—Part II: Gain and noise in short avalanche photodiodes," *IEEE Trans. Electron Device*s, vol. 46, pp. 1632–1639, 1999.

Vita

Xiaoguang Sun was born in Weihai, Shandong, China on September 30, 1971, the son of Langyi Sun and Lijun Wang. After completing his work at Weihai No. 2 High School in Weihai, Shandong, China in 1990, he entered Tsinghua University in Beijing, China. He received the degree of Bachelor of Science in Materials Science and Engineering in July 1995 with honor. In September 1995, he entered the Graduate School of Tsinghua University, Beijing, China, where he received the degree of Master of Science in Materials Science and Engineering in July 1997. In August 1997, he entered the Graduate School of University of Pennsylvania and majored in Materials Science and Engineering. In June 1998, he married his wife, Yuming Gu. In July 1998, he transferred to the Graduate School of the University of Texas at Austin to pursue his Ph.D. degree in the Electrical and Computer Engineering Department. In December 2000, he received the degree of Master of Science in Electrical Engineering.

Permanent address: Haidian Lanqiying District, Building 7, Room 1301, Beijing, 100084, China.

This dissertation was typed by the author.